博士論文

Soft X-ray analyses of O_2 and CO_2 adsorption to active sites in nitrogen-doped carbon-based catalysts

(軟 X 線分光を用いた窒素ドープカーボン触媒の O_2、CO_2 吸着状態解析による活性点の評価)

平成 27 年 12 月

指導教員　川合眞紀

東京大学大学院工学系研究科応用化学専攻

川合研究室　37-137104　木内　久雄

Contents

Chapter 1

General Introduction

1.1 Background

Polymer electrolyte fuel cell (PEFC) has many advantages to zero emission vehicles and potable batteries due to high efficiency, no harmful gas emission, and low operation temperature, which have attracted much attention as a promising energy conversion system suitable for the sustainable society. In general, Pt-based catalysts are utilized as cathode catalysts to accelerate the sluggish oxygen reduction reaction (ORR) in the present PEFC system [1]. Since Pt is expensive and limited material, alternative Pt-free or low-Pt-loading ORR catalysts are required to spread the PEFC system in the society. Recently, carbon-based catalysts such as carbon alloy catalyst (CAC) [2] are considered to be a candidate to replace the Pt-based catalysts. CACs are graphite base carbon materials modified by light elements (*i.e.* N, B, O, P, and S) and 3*d* transition metals. The most critical problem of CACs possess that the ORR activity of CACs does not surpass that of Pt-based catalysts. Although many groups have been trying to improve the ORR activity, the roles of light elements and transition metals on the ORR activity are not clarified yet. Thus, it is necessary to elucidate the ORR active sites of CACs to improve the ORR activity. In this study, I focus on the nitrogen components of CACs without transition metals to investigate the role of light elements.

1.2 Polymer electrolyte fuel cell

1.2.1 Principles of PEFC

Figure 1.1 shows a schematic image of PEFC. The membrane electrode assembly (MEA) is composed of proton conductive ionomers (membrane), catalysts, and gas diffusion layers [3]. Reactions at anode and cathode electrodes are shown in the

following equations:

$$\text{Anode:} \quad H_2 \rightarrow 2H^+ + 2e^- \quad \cdots (1.1)$$

$$\text{Cathode:} \quad O_2 + 4H^+ + 4e^- \rightarrow 2H_2O \quad \cdots (1.2)$$

$$\text{Total reaction:} \quad H_2 + 1/2\, O_2 \rightarrow H_2O. \quad \cdots (1.3)$$

At the anode electrode, introduced hydrogen fuel gas reacts on the catalysts, which produces protons and electrons through hydrogen oxidation reaction (1.1). While protons are carried to pass the membrane and react with introduced oxygen gas at the cathode electrode through ORR (1.2), the electrons are flowed to pass an external circuit and then generate the electricity. The product is only water in total reaction (1.3). PEFC generates the electricity by a direct conversion of chemicals to electrical energy without a conversion of chemicals to heat. Therefore, PEFC is a clean and high efficient energy conversion system.

The standard cell voltage E_0 of PEFC can be obtained by the Gibbs free energy change (ΔG_0) for the difference of the electrode potential of the anode and the cathode through the following equation:

$$E_0 = -\Delta G_0 / nF = 1.23 \text{ V} \quad \cdots (1.4)$$

where n is the number of electrons transferred and F is Faraday's constant.

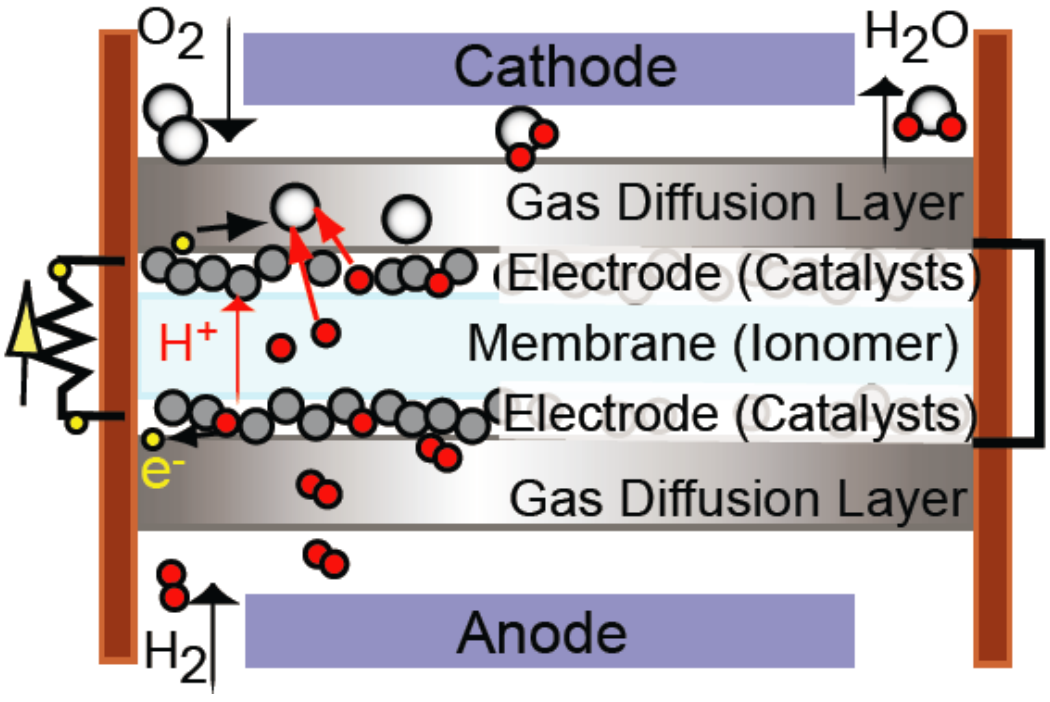

Figure 1.1 A schematic image of PEFC system.

1.2.2 Oxygen reduction reaction in PFEC

ORR is composed of several elementary processes as shown in Fig. 1.2. Oxygen is adsorbed on the catalyst surface, and subsequently two ORR processes proceed mainly at the cathode of PEFC through the following equations;

$$k_1:\ O_2 + 4H^+ + 4e^- \rightarrow 2H_2O \quad (E_0: 1.23\ \text{V}) \qquad \cdots (1.5)$$

$$k_2:\ O_2 + 2H^+ + 2e^- \rightarrow H_2O_2 \quad (E_0: 0.68\ \text{V}) \qquad \cdots (1.6)$$

$$k_3:\ H_2O_2 + 2H^+ + 2e^- \rightarrow H_2O \quad (E_0: 1.77\ \text{V}) \qquad \cdots (1.7)$$

One step 4-electron reaction (1.5) is the ideal reaction to generate the electricity. It is, however, known that the onset electrode voltage usually decreases below 1 V in the PEFC system due to the overvoltage. In contrast, two steps 4 (2 + 2)-electron reaction generates H_2O_2 and H_2O in combination with (1.6) and (1.7), where the standard cell voltage is 0.68 V (1.6). Thus this reaction (1.6) results in the decrease of the onset electrode voltage. In addition, powerful oxidizing agent H_2O_2 reacts with a Fe ion through the Fenton reaction [4] and generates OH radical species through the following equations;

$$Fe^{2+} + H_2O_2 \rightarrow Fe^{3+} + HO\cdot + OH^- \qquad \cdots (1.8)$$

$$H_2O_2 + HO\cdot \rightarrow HO_2\cdot + H_2O. \qquad \cdots (1.9)$$

The generated radical species would decompose the membrane and lead to the degradation of durability in PEFC system. Therefore, the requirement for the efficient fuel cell catalysts is the high selectivity to the 4-electorn process with low Fe impurities.

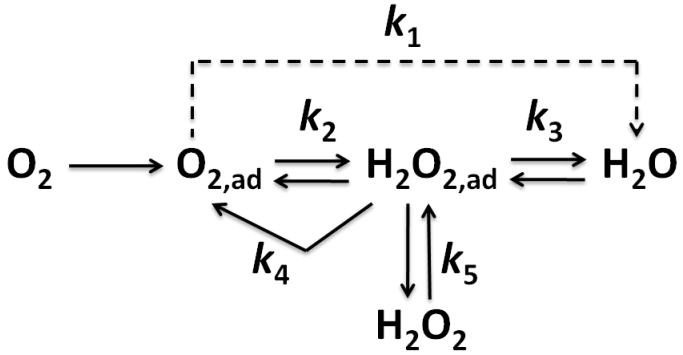

Fig. 1.2. Elementary processes of ORR process.

1.3 Oxygen reduction catalysts for cathode electrode

As PEFC can operate at lower temperature, such as 80 °C, than the other types of fuel cells, PEFC system shows excellent performance in start-up properties and has been utilized for the automobile, household fuel cell system, and mobile applications. However, reaction rates at electrodes slow down at such a low temperature. In order to accelerate the reaction rate, Pt-based catalysts are widely utilized.

1.3.1 Pt-based cathode catalysts

Pt efficiently catalyzes the ORR at the cathode. Accelerating ORR reaction is essential for the PEFC system since ORR is known as the cause of the most of overpotential [1]. Recently, alternative cathode catalysts have been required to develop the low-cost PEFC system due to the precious and expensive Pt metal. Many research groups approach to reduce the use of Pt amount and enhance the ORR activity on the cathode for example; Pt-*M* alloys (*M*: 3*d* transition metal) [5,6], surface modified *M*-Pt_3Ni [7], three-dimensional open-framework structure of Pt_3Ni [8], structure controlled nanocage Pt [9], and dispersed single Pt atom on catalyst supports [10]. PtCo catalysts have been already utilized practically in the state-of-the-art fuel cell vehicle (MIRAI, Toyota motor corp.) [11].

1.3.2 Carbon-based cathode catalysts

Pt-free catalysts have been also intensely investigated for the last several decades. Among alternative Pt-free catalysts, carbon-based cathode catalysts have attracted much attention due to their relatively high ORR activity. Since Jasinski reported the catalytic activity of Co phthalocyanine for ORR in 1964 [12] and Jahnke *et al.* discovered the activity improvement of Co TAA (Co dibenzotetraazaannulene) through the heat treatment in 1976 [13], there have been numerous attempts to develop precious-metal-free carbo-based cathode catalysts. These materials such as CAC are a mixture of carbon materials with light elements (*i.e.* N, B, O, P, and S) and 3*d* transition metals. In general, they are synthesized by pyrolysis of mixtures of macrocyclic complexes such as phthalocyanine and porphyrin with Fe-N_4 and Co-N_4, and carbon compounds under inert gas. In addition, Gupta *et al.* reported more simple synthesis method without macrocyclic complexes by pyrolysis of mixture of carbon precursors

with nitrogen species and metal salts in 1989 [14], whose method can be applied to a large variety of compounds. Thereafter, the competition in research and development of carbon based cathode catalysts has been more and more intense.

Figure 1.3 shows the changes of PEFC performance using carbon-based cathode catalysts [15–34]. In particular, Dodelet and Zelenay groups have been extensively developing ORR catalysts. Sun *et al.* reported that the ORR activity of the most active catalyst, which is composed of dual doped nitrogen and sulfur components [33], reaches to approximately 80% of that of Pt-based catalysts. The colored markers in Fig. 1.3 indicate the metal-containing ORR catalysts. Recently, however, transition metal-free ORR catalysts has been also developed (black cross marker). In order to surpass the ORR activity of Pt-based catalysts, it is required to reveal ORR active sites of these carbon-based cathode catalysts. Several research groups reported the two major candidates for the ORR active sites: (1) metal-N_x sites and (2) nitrogen doped carbon sites. These metal-N_x sites may be derived from macrocyclic complexes or formed during the pyrolysis step [20,35], which accelerate the ORR via side-on or end-on adsorption of O_2 molecule. Besides the candidate for the ORR active sites, other possible roles of transition metal may be the formation of the highly graphitized carbon structures during the pyrolysis step rather than the improvement of the ORR activity since the ORR activity remains nearly constant and the residual metals exist inside carbon nanoshell structures after HCl acid treatments to remove the most of the metals [36]. Secondly, as the candidate without metal species, nitrogen itself may improve the ORR activity because some carbon-based cathode catalysts without metal-containing precursors exhibit the ORR activities in the recent works [27,34,37–39]. Several research groups reported the possible ORR mechanism with pyridinic nitrogen [40], graphitic nitrogen [41], other nitrogen species, and carbon sites in the vicinity of the doped nitrogen [42–44]. However, the role of the nitrogen in ORR activity has not clarified yet.

Among the catalyst derived from Fe phthalocyanine and phenolic resin with different pyrolysis temperature [45], the ORR activity rapidly increases over 550 °C and becomes maximum at 600 °C with the decomposition of macrocyclic precursors and graphitization of carbon precursors. Subsequently, it decreases in the high temperature region. However, the most active catalyst at 600 °C has poor graphitized carbon

structures which result in the lower durability. In order to be compatible with the ORR activity and the durability, catalysts have been synthesized with highly graphitized carbon structures in the high temperature region where the structure of metal-containing macrocyclic precursors is perfectly decomposed. From this result, it is probable that the highly active and durable ORR active sites are originated from the nitrogen species doped into carbon matrix. In this study, therefore, I only focus on the role of nitrogen without metals to exclude the effects of metal species.

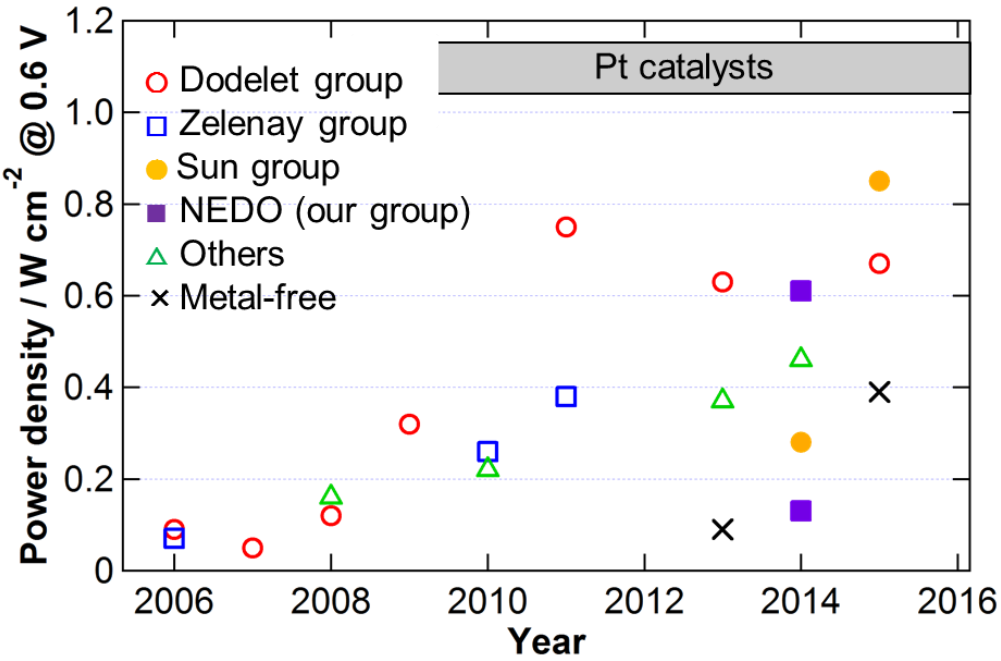

Fig. 1.3 Changes in the power density at 0.6 V in MEA condition for PEFC with carbon-based cathode catalysts. Cathode – O_2: 0.1-0.2 MPa. Temperature: 80°C.

1.3.3 ORR mechanism for carbon-based cathode catalysts

Several elementary processes occur during the ORR as shown in Fig. 1.2. Carbon-based cathode catalysts have lower ORR activity and lower selectivity of 4-electron process than that of Pt-based catalysts [46], indicating that the ORR activity of the carbon-based cathode catalysts would results from the different ORR processes compared to that of the Pt-based catalysts. Elementary reactions on the Pt surface are extensively investigated for several decades [47]. The hybridized electronic structure of

O_2 and Pt promote the O_2 adsorption with the side-on configuration, and dissociative reaction of an activated O_2 occurs to form Pt-O configuration. Similarly, the elementary processes should be investigated on the carbon-based cathode catalysts to elucidate the ORR mechanism and the role of nitrogen. In this study, therefore, *in situ* spectroscopic measurements are performed to observe the change of the electronic structure of each element.

1.4 Nitrogen doped graphite/graphene model catalysts

1.4.1 Nitrogen doped model catalysts synthesis

In general, powder samples for carbon-based cathode catalysts were investigated in the previous studies [48]. However, it is difficult to determine the detailed ORR active sites because the powder catalysts possess the various chemical states of carbon, nitrogen, and oxygen. It is necessary therefore, for an effective breakthrough, to synthesize a well-defined nitrogen doped carbon model catalyst such as graphene and graphite with controlling the chemical states of nitrogen species. In this model system, the selective nitrogen components can be generated while morphology, surface are, and crystallinity remain almost constant. Therefore, this model catalyst can be compared to the carbon-based catalyst in the high temperature region [45] due to the highly graphitized and nitrogen-doped carbon structure in this catalyst, which reveals the relationship between the nitrogen species and the ORR activity. Several methods are proposed to synthesize the nitrogen doped graphite and graphene, for example, nitrogen ions sputtering [49], pyrolysis under NH_3 gas [50], chemical vapor deposition growth under NH_3 gas [51] or with pyridine precursors [52]. In this study, highly oriented pyrolytic graphite (HOPG) is used as carbon substrate and doping through nitrogen ion sputtering is utilized, since the amount of ions can be controlled well using this method.

1.4.2 Property of doped nitrogen in the model catalyst

Recently, Kondo *et al.* reported the local electronic states in detail for the doped nitrogen and the surrounding carbon using scanning tunneling microscope (STM) and scanning tunneling spectroscopy (STS) as shown in Fig 1.4 [49]. The localized electronic structure was observed above the Fermi level in graphitic N, while below the Fermi level in pyridinic N. The modified electronic structures near the Fermi level

would hybridize with that of O_2 molecules and have the potential to catalyze ORR process. Therefore, it is necessary to investigate the interaction between the electronic states of catalysts and reactant. As for the first step of ORR, O_2 is adsorbed on the catalytic active sites. Since the ORR proceeds with electrons from the substrate as shown in equations 1.5 and 1.6, these catalytic active sites would be the electron rich sites that donate electrons to the adsorbates. In another word, the site can be express as a Lewis base site. In general, the existence of Lewis base sites can be proved by the CO_2 adsorption [53,54]. In this study, therefore, CO_2 adsorption method is applied to the model catalyst to elucidate the Lewis basicity of the nitrogen doped graphite substrate.

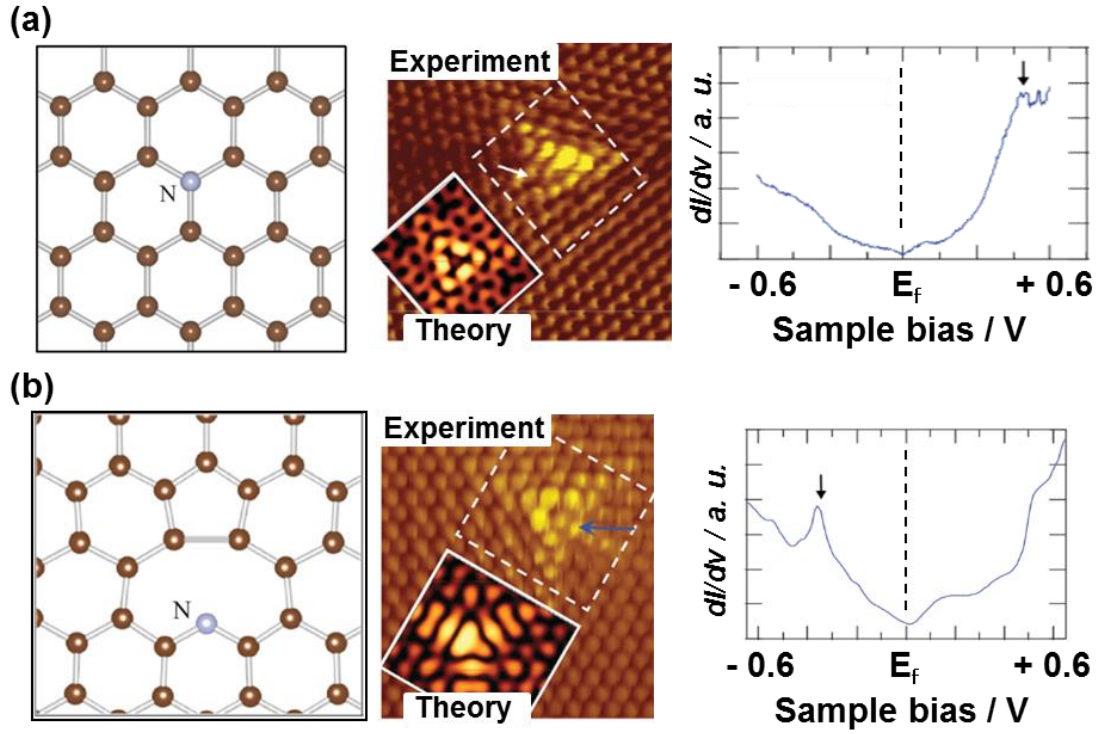

Fig. 1.4. Schematic images, STM images, and STS spectra of (a) graphitic nitrogen and (b) pyridinic nitrogen [49].

1.5 Purpose of this study

The purpose of this study is to reveal the role of nitrogen toward the ORR activity of the carbon-based cathode catalysts. In order to investigate the O_2 adsorption sites on the nitrogen-containing metal-free CACs, the electronic structure of each element was investigated before and after the O_2 adsorption using *in situ* X-ray photoelectron spectroscopy. In order to synthesize model catalyst with the kind and amount of nitrogen species in a controlled manner, the nitrogen doped graphite model catalyst was synthesized via low energy nitrogen ion sputtering to the HOPG surface. I investigated the characterization of the doped nitrogen using soft X-ray spectroscopy. I discussed the nitrogen doping mechanism and observed the development of the ORR activity. Furthermore, the property of CO_2 adsorption on the model catalyst was investigated to evaluate the Lewis basicity of a nitrogen-doped graphite substrate as an indicator of the ORR activity. Therefore, I clarified the role of nitrogen in the carbon-based cathode catalysts in combination with both the current catalyst (top down study) and the model catalyst (bottom up study).

Chapter 2

Experimental methods

2.1 Sample preparation

2.1.1 Carbon alloy catalysts (CACs)

The CACs were prepared by pyrolyzing poly meta-phenylene isophthalamide (denoted as polyamide), which contains no metal species with nitrogen species. The synthesis of the polyamide is shown in the previous report [38]. The polyamide was pyrolyzed at 600 °C for 1 h under N_2 flow, followed by ball milling with 5 min × 17 times at 750 rpm. Finally, the sample was pyrolyed again at 600 °C for 4 h under N_2 flow. The product will be referred to as PA. As a reference, a catalyst without nitrogen and metal species was prepared by pyrolyzing phenolic resin (PSK-2320, Gunei Chimical Co.) in the same synthesis manner. The product will be referred to as PhRs.

2.1.2 Nitrogen doped graphite (N-HOPG)

The model N-HOPG catalysts was synthesized at BL07LSU in SPring-8 in collaboration with Prof. Junji Nakamura's laboratory of Tsukuba University. The N-HOPG preparation chamber was constructed for this study. This chamber was composed of the sample introducing chamber (LL) and the sample preparation chamber (Prep.). Typical base pressures of LL and Prep. chambers were 5×10^{-6} and $<5 \times 10^{-7}$ Pa, respectively. The Prep. chamber was equipped with an ion gun (OMI-0730, Omegatron Co., Ltd.), a back surface electron bombardment heating apparatus (AVC Co., Ltd), an electric feed through to measure the compensating current, and a micro-channel plate (MCP) (Hamamatsu Photonics K.K.) analyzer, as shown in Fig. 2.1. The number of the sputtered ions was calculated by measuring the compensating current caused by the impinging ions. In order to control the number of sputtered ions accurately, the mechanical shutter was mounted. The ion beam was scanned vertically and horizontally

using the multifunction synthesizer (WF1944B, NF Corp.) to prepare the homogeneous doping of nitrogen species on the N-HOPG. Molybdenum sample holders were designed to anneal the samples more than 1000 K. The sample temperature (>600 K) was monitored by the fiber-type radiation thermometers (FTK9-P300A-30L21, Japan Sensor Corp.) with the emissivity of 0.85 and was constant throughout the sample surface. This chamber is designed to perform the X-ray absorption spectroscopy by using MCP when the chamber is connected to the beamline of BL07LSU in SPring-8.

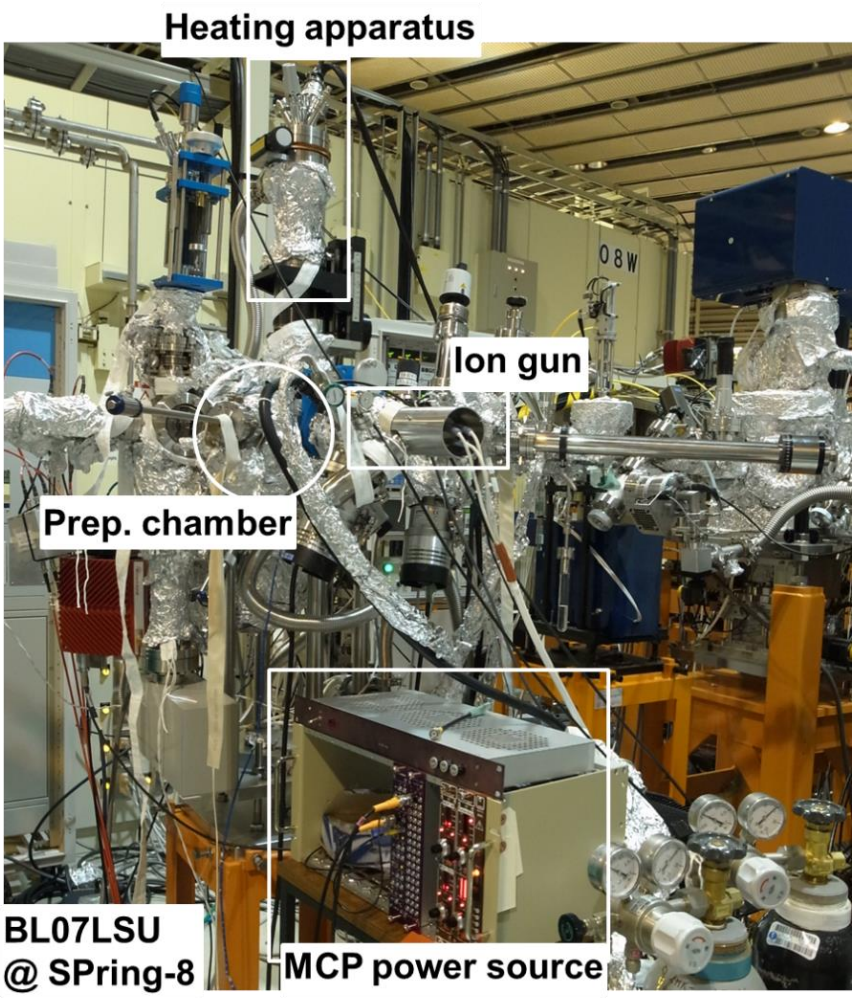

Fig. 2.1. The N-HOPG preparation chamber at BL07LSU in SPring-8.

A highly oriented pyrolytic graphite (HOPG) (PGCSTM, Panasonic Corp.) was cleaved in air using adhesive tape, and set in an ultra-high vacuum chamber (<5 × 10^{-7}

Pa). The substrate was then annealed at 1000 K for 30 min, and sputtered with nitrogen ions (N_2^+) at 300 K using the ion gun. The ion acceleration voltage was set to low energy as 200 eV in order to dope nitrogen atoms near the surface without disturbing the graphene lattice [49]. Finally, the samples were annealed at 1000 K for 1h for surface cleaning and to recover the crystallinity. These samples will be referred to as N-HOPG hereafter.

2.2 Electrochemical measurements

Electrochemical measurements are essential methods to evaluate the catalytic activity of electrode catalysts such as Pt and Au nanoparticles. In general, rotating ring disk electrode (RRDE) voltammetry is applied to investigate the number of transferred electrons *n* as well as the electrochemical activity [55]. In this study, this method was applied to evaluate the electrochemical characteristics of the CAC powders. However, this method cannot be applied to the plate-like N-HOPG since a suspension mixed with catalyst powder and Nafion is required to deposit it on the disk electrode. N-HOPG electrode was prepared directly instead as follow; attaching the iron wire with a conductive adhesive, pasting an inert polymer around the wire and adhesive, and drying in air. The detailed experimental setup and condition are described in the each following section.

2.2.1 Principles of RRDE voltammetry

Figure 2.2 shows a schematic image of RRDE measurements. The suspension mixed with the catalyst powder and Nafion is coated on the disk electrode. A voltage in the disk electrode (working electrode) relative to a reference electrode is swept while a constant voltage (~1.2 V) is applied in the ring electrode during rotating the electrode complexes. The mixed 4-electron and 2-electron oxygen reduction reactions, which generate H_2O and H_2O_2, respectively, occur on the disk electrode in the O_2 saturated liquid electrolyte.

$$O_2 + 4H^+ + 4e^- \rightarrow 2H_2O$$

$$O_2 + 2H^+ + 2e^- \rightarrow H_2O_2$$

The part of the generated H_2O_2 is reoxidized to the H_2O on the ring electrode with the constant voltage, while the other parts diffuse to the bulk electrolyte.

$$H_2O_2 \rightarrow O_2 + 2H^+ + 2e^-$$

The ratio of H_2O_2 collected in the ring electrode (collection efficiency: N) is theoretically determined by the size of the disk and ring electrodes. However, since the collection efficiency changes by the surface roughness of the electrode, the collection efficiency in real is estimated by measuring a reversible reaction such as $[Fe(CN)_6]^{4-}$/ $[Fe(CN)_6]^{3-}$ and Br^-/ Br^{3-}. The collection efficiency is 0.372 in this study. Therefore, the number of transferred electrons *n* and the yield of peroxide on the disk electrode can be calculated form the following equation.

$$n = 4 \times I_{disk} / (I_{disk} + (I_{ring} / N))$$

$$\%(H_2O_2) = 200 \times I_{ring} / (N \times I_{disk} + I_{ring})$$

where I_{disk} and I_{ring} are the Faradaic current at the disk and ring, respectively. The current density (A cm^{-2}) is calculated from the I_{disk} divided by the disk electrode area (0.2828 cm^2).

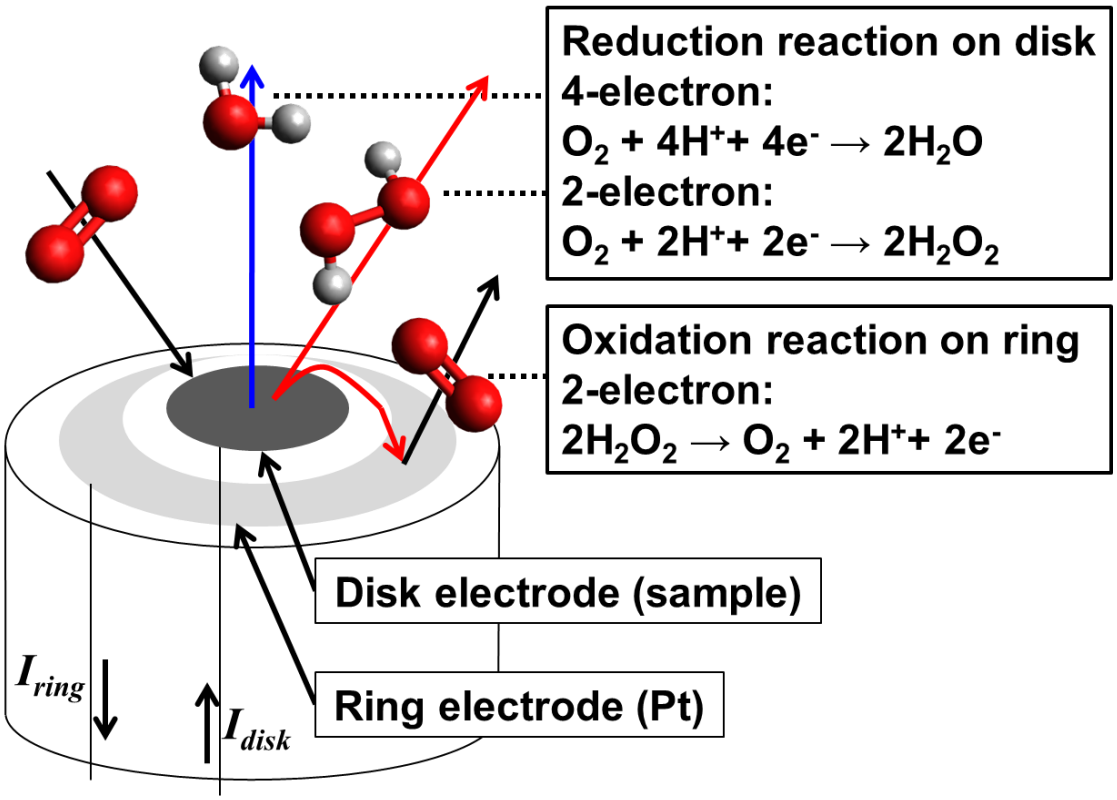

Fig. 2.2. A schematic image of RRDE measurements. Oxygen and hydrogen atoms correspond to red and white balls, respectively.

2.3 X-ray photoelectron spectroscopy (XPS)

X-ray photoelectron spectroscopy (XPS) is one of the most extensively used techniques to investigate the compositions and oxidation state of the sample. It is highly informative and semi-quantitative based on the well-developed theories, and is particularly useful in studies of solid surfaces and adsorption. In general, the characteristic X-ray (Al $K\alpha$ and Mg $K\alpha$) and the synchrotron radiation source are widely used as light sources. In this study, synchrotron radiation light source was used for the chemical composition analysis of the small amount of doped nitrogen species embedded in the carbon network.

2.3.1 Principles of XPS

Figure 2.3 shows a schematic diagram of photoemission process. When an electron in a material is excited by a photon whose energy (hv) is higher than the sum of the binding energy of the electron and the work function, it is emitted as a photoelectron. The binding energy E_B can be calculated from the following equation

$$E_B = hv - E_{kin}^{V} - \varphi$$

where E_{kin}^{V} is the kinetic energy of the photoelectron relative to the vacuum level, φ is the work function of the material. In order to compare the binding energy among different materials, it is convenient to use the kinetic energy E_k of the photoelectron relative to the Fermi level. Then, the binding energy can be simply expressed by the following equation

$$E_B = hv - E_k.$$

The energy distribution of the observed photoelectron has information about the core level and valence band of materials, and is proportional to the density of state of the occupied electronic structure. Therefore the identification of elements can be easily conducted due to the different binding energy of the core level of each element.

2.3.2 Chemical states analyses

The amount of each element is calculated from the ratio of area intensities divided by cross section of each element. The observed XPS spectra are fitted with several Voigt functions by the least square line to analyze the chemical states of materials. The position and the integrated intensity of each peak represent the oxidation state and the

amount of each element, respectively. The Voigt function is the convolution of Lorentzian and Gaussian functions. The full width half maximum (FWHM) of each peak is determined by both Lorentzian width W_L and Gaussian width W_G. The Lorentzian width is determined by the lifetime of the core hole generated by the photoelectron emission, which depends on the elements and the orbital characters. The Lorentzian width for N 1*s* and O 1*s* are 0.25 eV and 0.30 eV in this study, respectively. While the Gaussian width depends on the extent of the core orbital, the main factors to decide the Gaussian width are the energy resolutions of the light source and the photoelectron detector. The Shirley method is often used for the background subtraction.

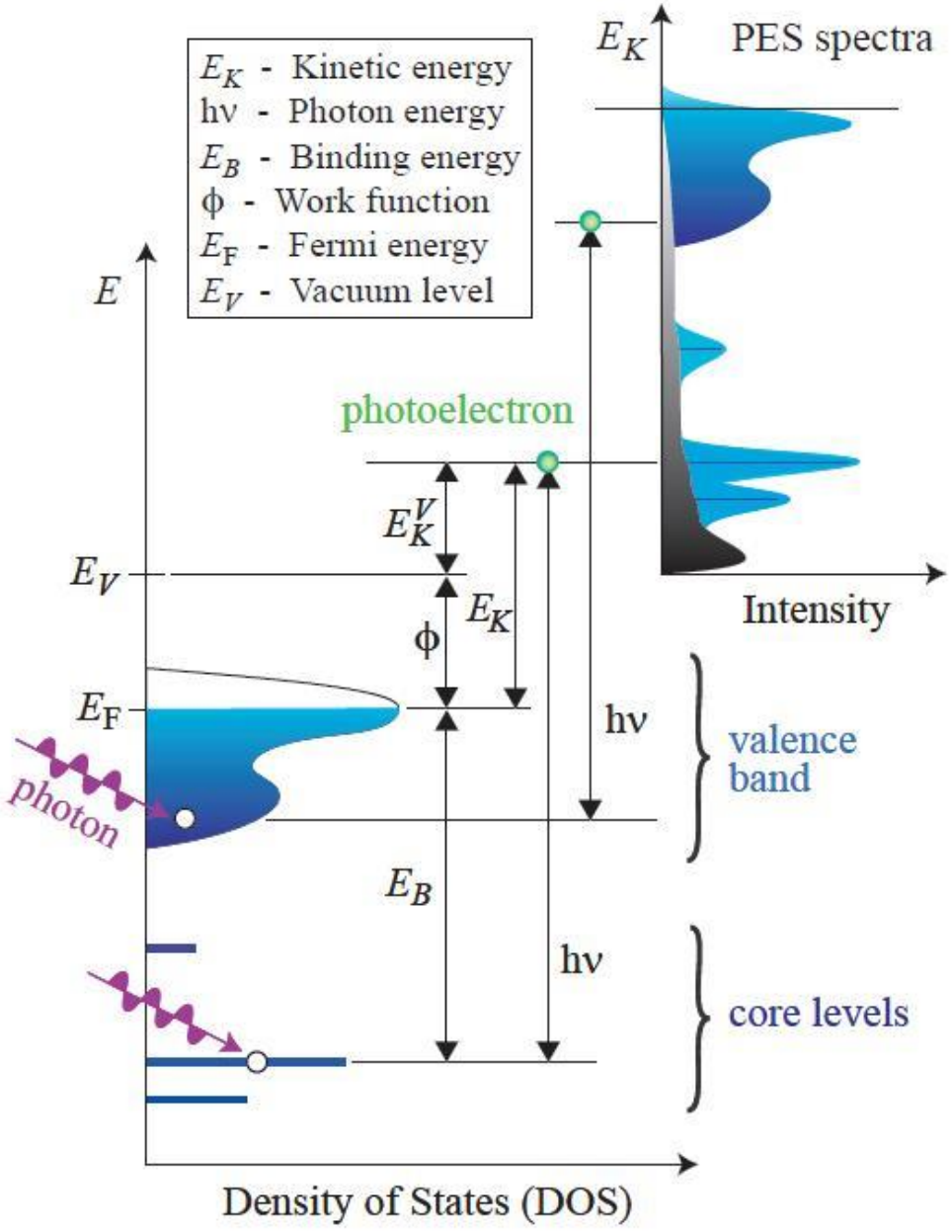

Fig. 2.3. A schematic diagram of photoemission spectroscopy [56].

2.4 X-ray absorption spectroscopy (XAS)

When the X-ray energy is scanned across the binding energy of a core level of a particular element and if X-ray absorption is plotted as a function of the excitation energy, one can probe X-ray absorption spectroscopy (XAS) which reflects element specific electronic structures of the unoccupied state [57]. The N and O 1*s* XAS measurements were performed in this study.

2.4.1 Principles of XAS

Figure 2.4 shows a schematic diagram of X-ray absorption process. An incident X-ray excites the electron in a core level into an unoccupied valence state. Then, this electron-hole state decays via fluorescence X-ray, photoelectron, Auger electron, and low energy secondary electron emissions. The X-ray transmission process also occurs depending on the energy of the incident X-ray or the thickness of materials. The transition probability I ($h\nu$) of X-ray absorption is described by applying Fermi's golden rule and dipole approximation. I ($h\nu$) is given by the following equation

$$I\ (h\nu) = \sum_{f} |\langle f|\hat{e}\cdot\vec{r}|i\rangle|^2 \delta(E_i\ -\ E_f - h\nu)$$

where $|\langle f|\hat{e}\cdot\vec{r}|i\rangle|$ is the dipole matrix element, f and i are wave functions of the final (energy E_f) and initial (energy E_i) states. The delta function $\delta(E_i - E_f - h\nu)$ takes care of the energy conservation. As an example for K-shell excitation of O_2 with the σ* and π* orbital, each transition moment is directed to the parallel and the perpendicular to the molecular axis, respectively. The polarization dependence of the total matrix element can be expressed as a function of the angle θ between the directions of the electric field vector and the largest amplitude of the final state orbital by the following equation

$$I\ (h\nu) \propto cos^2\theta.$$

Therefore the polarization dependence of σ* and π* peaks reveals the orientation of the adsorbed molecule on the surface.

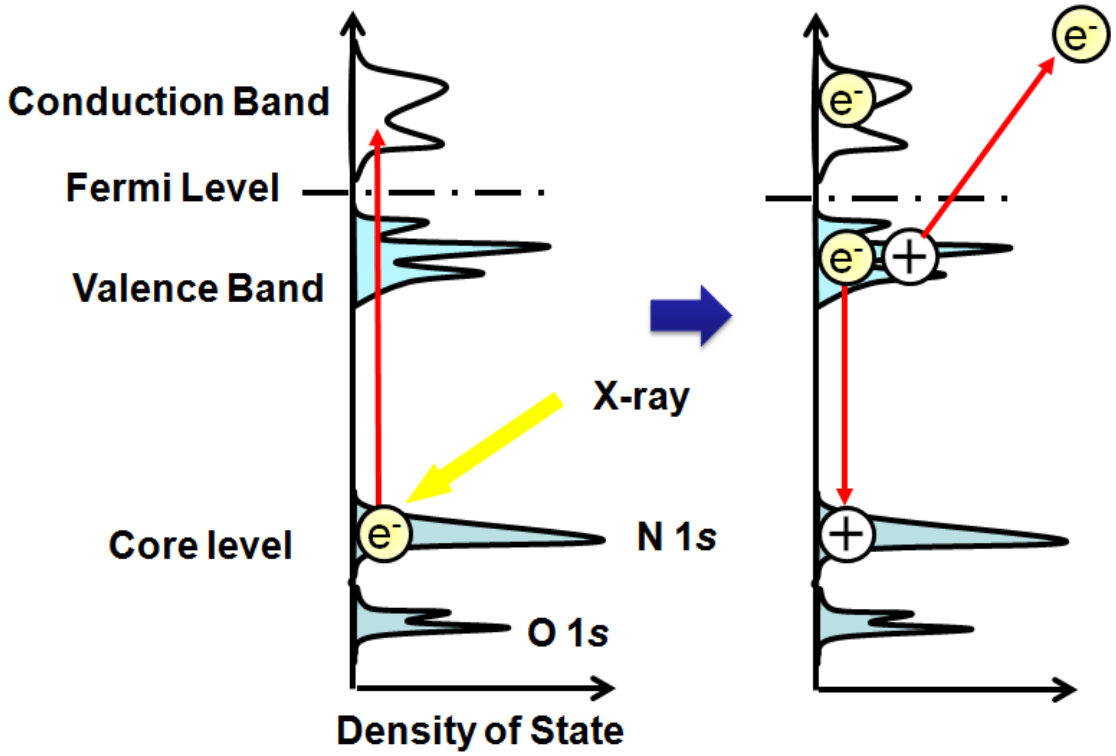

Fig. 2.4. A schematic diagram of X-ray absorption process.

2.4.2 Detection of XAS

There are several detection methods such as transmission, fluorescence yield, and electron yield. The X-ray transmission rarely occurs in the soft X-ray region due to the short penetration depth (~1 μm). As shown in Fig. 2.4, a generated core hole decays by either fluorescence channel or by the Auger channel. The electron yield is classified into a total electron yield (TEY) and a partial electron yield (PEY). In the TEY method, all electrons that emerge from the sample surface are detected, while in the PEY method, Auger electrons of a specific element are detected using a gold mesh with certain negative bias in order to remove the excess low energy secondary electrons, resulting in the better S/B ratio. The probing depths of TEY and PEY are approximately 3-10 nm and <3 nm, respectively, in the soft X-ray region. The PEY method was used in this study since it is suitable for measuring elements localized on the surface and the adsorbed molecules on the surface. In the PEY measurements a MCP analyzer (F2221-31S, Hamamatsu Photonics K.K.) was used.

2.4.3 XAS spectra fitting

The N 1*s* XAS analyses were performed by curve fitting in this study. Details of the analyses have been previously summarized by J. Stöhr [57]. The XAS spectra were fitted by Gaussian functions for each σ* and π* state, and step functions convoluted by an error function and an exponential decay function for the continuum states in each σ* and π* region. The error step function (I_{step}) and multiplied exponential decay step function ($\exp[-d(E - E_s - W_s)]$) in the following equations are used.

$$I_{step} = H\left[\frac{1}{2} + \frac{1}{2} erf\left(\frac{E - E_s}{W_s/c^*}\right)\right]$$

$$I_{step}^{exp} = I_{step}, \qquad E \leq E_s + W_s ,$$
$$I_{step}^{exp} = I_{step} \cdot \exp[-d(E - E_s - W_s)], \qquad E \geq E_s + W_s ,$$

where E_s is the positon of the inflection point of the step function, H is the height of the function above the step, W_s is the FWHM of the step function, d is the exponential decay coefficient, E is the independent variable energy, and $c^* = 2\sqrt{\ln 2}$.

2.5 Raman spectroscopy

Raman spectroscopy monitors a vibrational signal for specific chemical bonds including defect sites and is a versatile tool for studying the characteristics of carbon-based materials [58]. In this study, it is used to evaluate the amount of defects in carbon structures of the CACs and the N-HOPG.

2.5.1 Raman scattering process

Raman scattering is an inelastic scattering phenomena of photons by phonons, as shown in Fig. 2.5. In the Raman process, an incident photon with frequency ν_0 reaches the material and is scattered, resulting in the elastic scattering photon ν_0 (Rayleigh scattering light) and the weak inelastic scattering photon $\nu_0 \pm \nu_i$ (Raman scattering light) with the small frequency shift. The Stokes light and the anti-Stokes light correspond to $\nu_0 - \nu_i$ and $\nu_0 + \nu_i$, respectively. The intensities of the Stokes light (Raman shift) are plotted as a function of the difference between incident and scattered energy in the Raman spectra. Raman shift corresponds to the energy of a vibration mode, which gives similar energy to the IR spectroscopy.

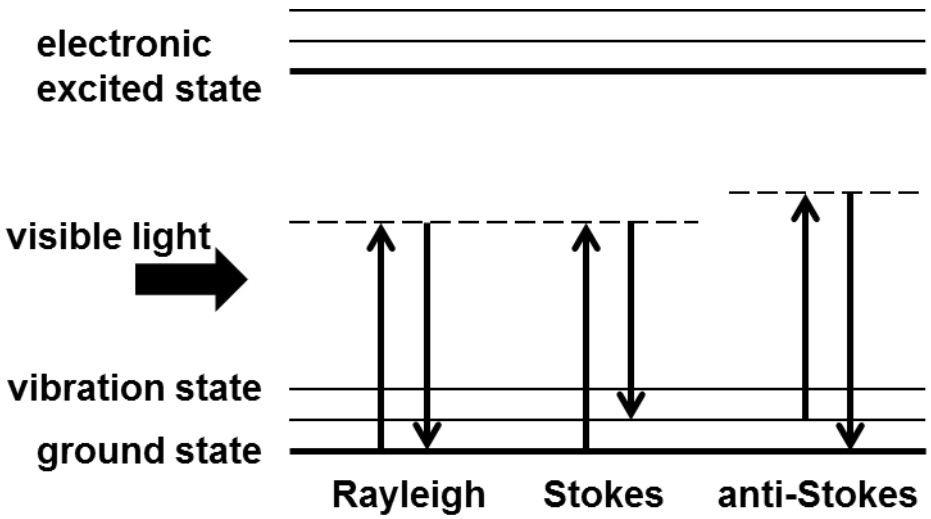

Fig. 2.5. A schematic diagram of Raman scattering process.

2.5.2 Raman shift in carbon-based materials

Carbon-based materials except diamond show the strong absorption in the visible light region, resulting in the shallow probing depth about several 10 nm [59]. The Raman spectroscopy is practically surface analyses method. The double degenerate E_{2g} mode is the Raman active in the sp^2 hybridized graphite structure and observed in ~1580 cm^{-1}. A defect structure induced in the graphite activates the A_{1g} mode in ~1350 cm^{-1} and 1620 cm^{-1} due to the breathing modes of six-membered rings. The former is called G-band, and the latter is called D-band and D'-band. The relative intensity ratio (I_D/I_G ratio) was used to evaluate the amount of defects in this work [58].

Chapter 3

O_2 adsorption property on nitrogen-doped metal-free carbon-based catalysts

3.1 Introduction

In order to develop PEFC in a large variety field for global environmental problems, the alternative cathode catalysts without expensive Pt are required. Several groups have reported that non-precious metal carbon-based materials such as CACs show high ORR activity [15–34]. CACs are composed of carbon-based substrates, transition metal and light elements. In the past several years, these materials are intensively investigated to achieve high activity comparable with Pt-based catalysts. However, the role of transition metal and light elements on the ORR activity has yet been dissolved. In the previous report, ORR activity was correlated with the nitrogen content among CACs derived from nitrogen-containing rigid-rot polymers [38]. Niwa *et al*. reported that graphite-like nitrogen is responsible for the ORR activity [60]. Ikeda *et al.* suggested by first principles calculation that the graphite-like nitrogen incorporated into the zigzag edge lowers the energy barrier for O_2 adsorption [42]. This means that nitrogen components which exist on a particular site enhance O_2 adsorption. In order to discuss the role of light elements on the ORR activity, it is necessary to study CACs without metal species since metal species would directly and indirectly contribute to the ORR activity [20,24,61].

I studied the characteristics of O_2 adsorption on CACs which containing light elements (carbon, nitrogen, and oxygen species) without metal species. A possible oxygen reduction site was discussed using O_2 adsorption isotherms, RRDE voltammetry, Raman spectroscopy, and *in situ* XPS. Since O_2 adsorption is the first step of ORR, the mechanism of oxygen reduction process on these systems will be further considered.

3.2 Experimental methods

The catalysts were prepared by pyrolysis of poly meta-phenylene isophthalamide and phenolic resin as a reference described in Chapter 2.1.1. The terminology of these catalysts is defined as PA and PhRs.

The oxygen reduction activity was evaluated by RRDE voltammetry at room temperature in a 0.5 M H_2SO_4 electrolyte solution. The electrodes were prepared by mixing 5 mg of the catalyst with 50 µl Nafion solution (Sigma-Aldrich Co. LLC.), 150 µl Millipore water and 150 µl ethanol, followed by sonication. Subsequently, 4 µl of the catalyst ink was deposited on a circular glassy carbon electrode and dried under atmosphere. The voltages were swept with respect to a reversible hydrogen electrode (RHE). Linear sweep voltammograms were recorded using an electrochemical equipment (ALS 2323, ALS Co. Ltd.), by rotating the electrode at 1500 rpm and sweeping the potential from 1.2 to 0 V (vs. RHE) at 5 mV s^{-1} in the saturated N_2 or O_2 gas electrolyte. The N_2 data were then subtracted from the O_2 data. The selectivity to H_2O_2 formation and the average number of transferred electrons *n* were calculated from the ring currents in Chapter 2.2.1.

In order to evaluate the degree of structural defects in PA and PhRs, Raman spectroscopy was carried out. Raman spectra were collected with a micro-Raman spectrometer (NR-1800, JASCO Corp.) with an excitation wavelength of 532 nm. Spectra for catalysts were acquired by performing two scans, each lasting 30 sec, from 700 to 2000 cm^{-1}. The wave length resolution is 2.6 cm^{-1}.

Gas adsorption isotherm measurements were performed for O_2 and N_2 gases at 298 K (Belsorp II mini, Bel Japan Corp.). The samples were pre-annealed at 500 °C for 1 h in vacuum in order to remove adsorbed water and oxygen before gas adsorption. Brunauer, Emmett, and Teller (BET) specific surface area was measured via N_2 adsorption at 77K.

XPS were performed using non-monochromatic Mg-$K\alpha$ source (JPS-9010MC, JEOL Ltd.). The effects of O_2 adsorption to the electronic structures of O 1*s* and N 1*s* were investigated in detail, while C 1*s* spectra were recorded to calculate the composition ratio of the sample. XPS spectra were recorded for three phases of PA and PhRs; before and after O_2 adsorption and after re-annealing to remove the adsorbed oxygen. Firstly the samples were annealed at 500 °C for 1 h in vacuum (<10^{-4} Pa) for the initial XPS spectra in order to remove the initially adsorbed gas under atmosphere. Secondly the

samples were exposed to 1 atm O_2 gas at 300 K for 1 h. Finally the samples were annealed at 500 °C for 1 h in vacuum (<10^{-4} Pa) again. Backgrounds of the core level spectra were subtracted by the Shirley method. Each spectrum was fitted with Voigt functions (N 1*s*: 1.6 eV Gaussian width and 0.25 eV Lorentzian width, O 1*s*: 2.0 eV Gaussian width and 0.3 eV Lorentzian width).

3.3 Results and discussion

3.3.1 RRDE voltammogram

Figure 3.1 shows RRDE voltammogram, H_2O_2 yield, and number of electrons in PA, PhRs, and Pt (50 wt%). The electrochemical properties of CACs are summarized in Table 3.1. The nitrogen-containing PA exhibits higher ORR activity (E_{O_2}: 0.79 V) than the nitrogen-free PhRs (E_{O_2}: 0.60 V) while the Pt (50 wt%) exhibits much higher activity (E_{O_2}: 0.98 V) and selectivity of a 4-electron ORR process (H_2O_2 yield: ~100% and number of electrons: ~4.0). The H_2O_2 yield and number of electrons in PhRs are 55% and 2.9, however, those in PA are 70% and 2.6, respectively. The increased selectively of a 2-electorn ORR process in PA is driven by the formation of ORR active sites which accelerate the 2-electron ORR process, indicating that nitrogen incorporated into PA mostly contributes to the increase of 2-electron ORR active sites.

Table 3.1. Electrochemical activities, H_2O_2 yield, and number of electrons for ORR in PA and PhRs

Sample	E_{O_2} [a] / V vs. RHE	H_2O_2 yield[b] / %	Number of electrons[b]
PA	0.79	70	2.6
PhRs	0.60	55	2.9

[a] Oxygen reduction potential defined as the voltage at which a reduction current density of -10 μA cm^{-2} is reached.

[b] H_2O_2 yield and number of electrons at 0.30 V vs. RHE.

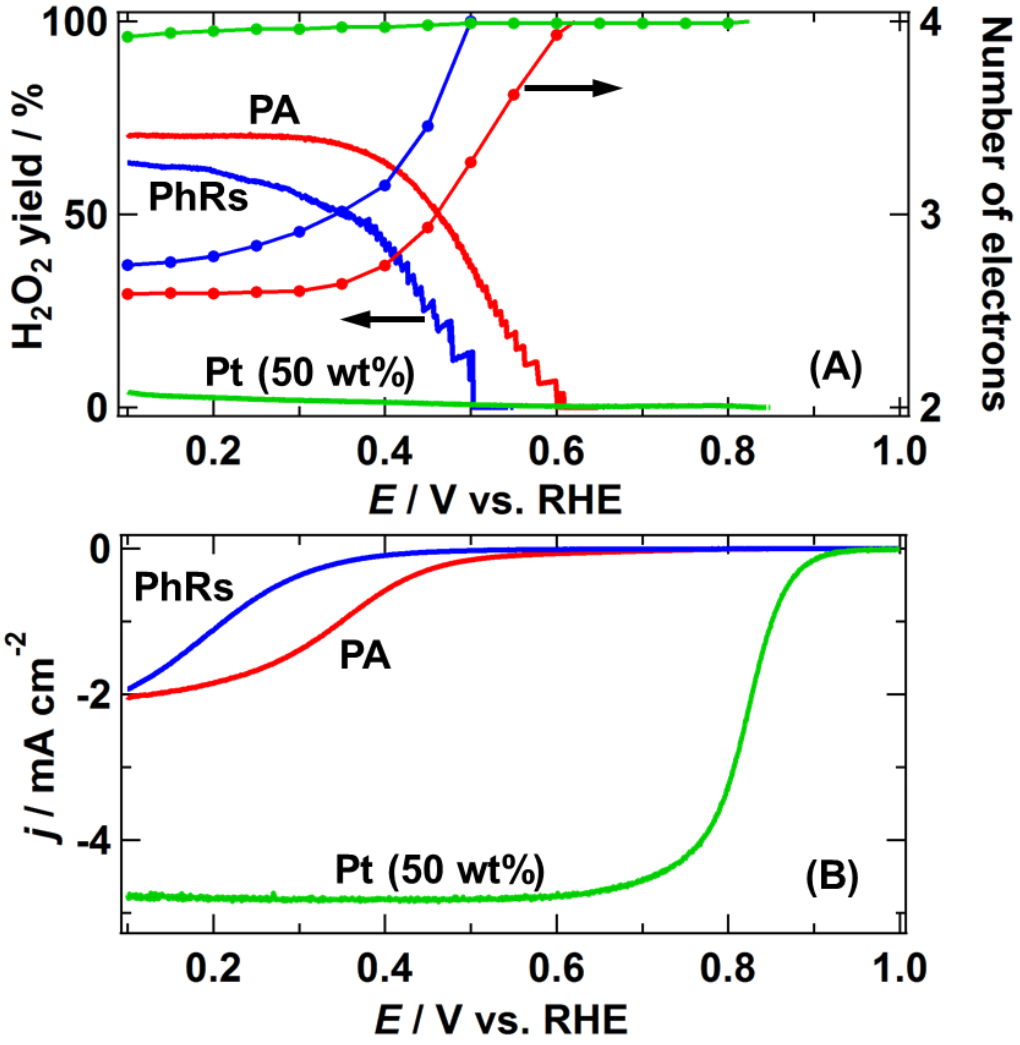

Fig. 3.1. (A) H_2O_2 yield and number of electrons and (B) RRDE voltammogram for ORR in PA (red), PhRs (blue), and Pt (50 wt%) (green).

3.3.2 Raman spectroscopy

Figure 3.2 shows Raman spectra of PA and PhRs. The D-band around 1340 cm^{-1} and the G-band around 1590 cm^{-1} are appeared, which are derived from carbon defects and hexagonal graphitic carbon structures, respectively. The peak height intensity ratio of the D-band to G-band, I_D/I_G, provides information about the degree of amorphous carbon and/or the amount of structural defects. The I_D/I_G ratio in PA was 1.06, larger than 0.93 observed in PhRs, indicating introduction of more amorphous carbon, structural defects, edges or other disordered structures caused by heterogeneous nitrogen atoms incorporated into PA [62,63].

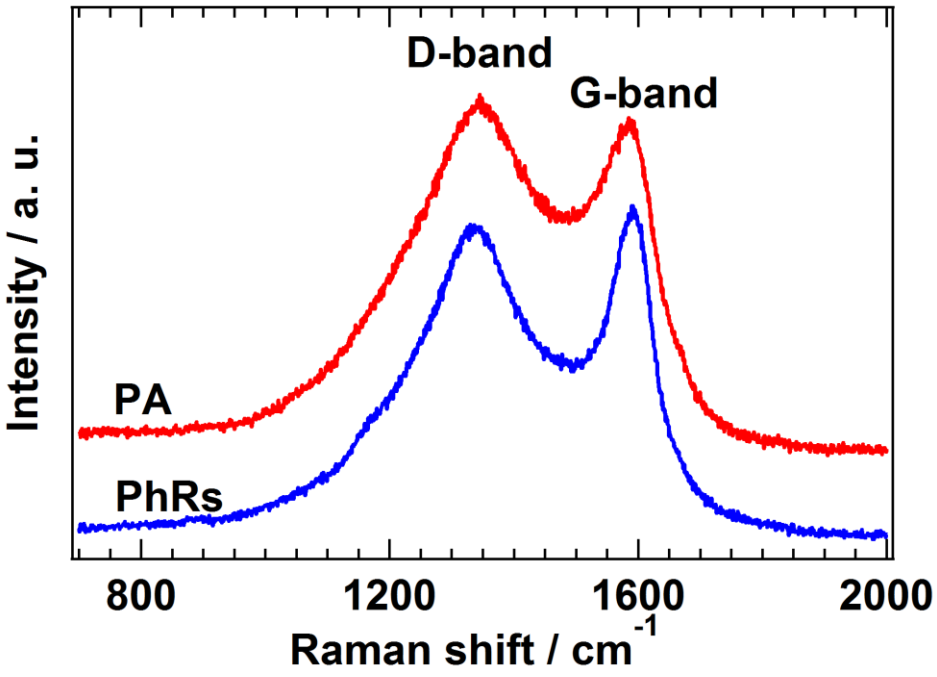

Fig. 3.2. Raman spectra of PA and PhRs

3.3.3 O_2 and N_2 adsorption isotherms

Figure 3.3 shows O_2 and N_2 adsorption isotherms of PA and PhRs at 298 K. The O_2 adsorption isotherm of both PA and PhRs shows two-step behavior, i.e. the amount of the adsorbed O_2 drastically increases with increasing the pressure in the low-pressure region below 0.1 kPa, while it shows a moderate linear increase in the subsequent high-pressure region [64]. However, the N_2 adsorption isotherms show no drastic

increase and little amount of the adsorbed N_2. The amount of the adsorbed O_2 is much higher than that of the adsorbed N_2 in both PA and PhRs, indicating that the O_2 adsorption is not physisorption but chemisorption process. The amount of the adsorbed N_2 is almost the same for both PA and PhRs, however that of the adsorbed O_2 is 1.0 mg g^{-1} for nitrogen-containing PA and 0.4 mg g^{-1} for nitrogen-free PhRs at 0.1 kPa. BET surface areas of PA and PhRs shown in table 3.2 are almost the same; 456 m^2 g^{-1} and 523 m^2 g^{-1}, respectively. If O_2 molecules equally interact with and adsorb on the catalyst surfaces, the amount of adsorbed oxygen should be identical among materials with the same BET surface. However, it is different that the amount of the adsorbed O_2 of PA and PhRs, indicating that nitrogen components incorporated into PA enhance the O_2 adsorption. Pollak *et al*. reported that the O_2 adsorption on the carbon surface at 523K is more pronounced when nitrogen atoms are introduced in the carbon structure [65]. Thus nitrogen atoms would contribute to alter the property of carbon materials to enhance the O_2 adsorption.

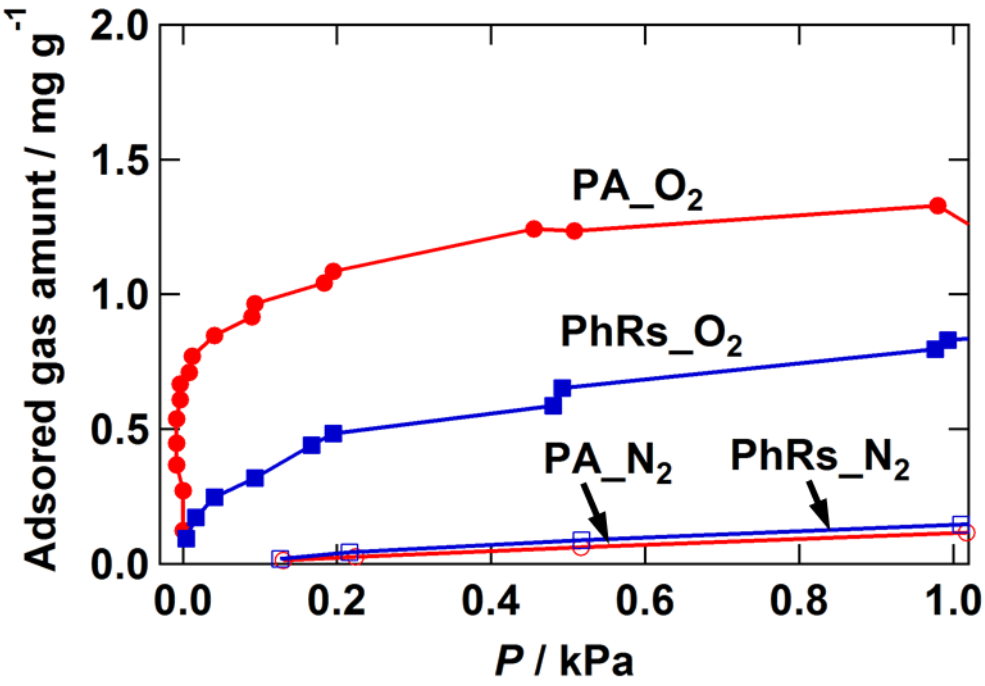

Fig. 3.3. The adsorption isotherms for O_2 and N_2 gas on PA and PhRs at 298 K. Full red circle and full blue squares denote the O_2 adsorption on the fresh PA and PhRs samples, respectively. Open red circles and open blue squares are for the N_2 adsorption on the fresh PA and PhRs.

Table 3.2. The BET specific surface area and the amount of adsorbed O_2 in PA and PhRs

Sample	S_{BET}[a] / m^2 g^{-1}	$O_{2,\ ads}$ amount[b] / mg g^{-1}
PA	456	1.0
PhRs	523	0.4

[a] BET specific surface area.

[b] The amount of adsorbed O_2 on the sample at 0.1 kPa.

3.3.4 In situ XPS analyses

The composition ratios of PA and PhRs estimated from XPS spectra are summarized in Table 3.3. The initial XPS spectra before oxygen adsorption of PA and PhRs are simply labeled as PA and PhRs, respectively. Subsequently, the second and final XPS spectra after oxygen adsorption and desorption by re-annealing are labeled as PA_O_2, PhRs_O_2, and PA_O_2_an.

Table 3.3. The composition ratio for PA and PhRs estimated from the XPS spectra. "O_2" and "an" extensions indicate "O_2 adsorption" and "annealing", respectively

Sample	C / at.%	N / at.%	O / at.%
PA	93	5.5	1.1
PA _O_2	92	5.5	2.7
PA _O_2_an	93	5.5	1.3
PhRs	99	0.2	1.3
PhRs _O_2	98	0.0	2.3

As shown in Table 3.3, the amount of the adsorbed oxygen is 1.6 at.% for PA and 1.0 at.% for PhRs. The increase in the amount of the adsorbed oxygen detected by *in situ* XPS for PA compared to PhRs is consistent with that estimated by the O_2 adsorption isotherms. Figure 3.4 shows O 1*s* XPS spectra of PA and PhRs before and after O_2 adsorption and after O_2 desorption. The spectra are normalized to the atomic ratio of each sample as shown in Table 3.3. The O 1*s* XPS spectra are decomposed into three peaks (OP1-OP3) corresponding to different chemical states of oxygen; the C=O group appears around 531.2-531.6 eV (OP1), the C-OH and C-O-C groups around 532.2-533.4 eV (OP2), and chemisorbed oxygen or water around 534.6-535.4 eV (OP3) [66,67]. Table 3.3 shows the atomic ratios and the relative composition ratios of the adsorbed oxygen extracted by comparing the XPS spectra before and after O_2 adsorption. It is revealed that the relative composition ratio of the adsorbed C=O component (OP1) are 57% in PA and 41% in PhRs, indicating that C=O components are likely to be incorporated into PA which has high selectivity of a 2-electron ORR process. In Fig. 3.4, the O 1*s* spectral profiles of (a) PA and (b) PA_O_2_an are similar, suggesting the reversible reaction of O_2 adsorption/ desorption.

Table 3.4. The atomic ratio of the adsorbed oxygen components and the relative composition ratios of three oxygen components calculated from XPS fitting results, which are estimated by subtracting oxygen atomic ratio of the annealed sample from that of the O_2 adsorbed sample

Precursor material	Atomic ratio / at.%	Relative composition ratios of the adsorbed oxygen / %		
	Adsorbed O	C=O	C-OH, C-O-C	Chemisorbed H_2O
PA sample	1.6	57	40	4
PhRs sample	1.0	41	51	8

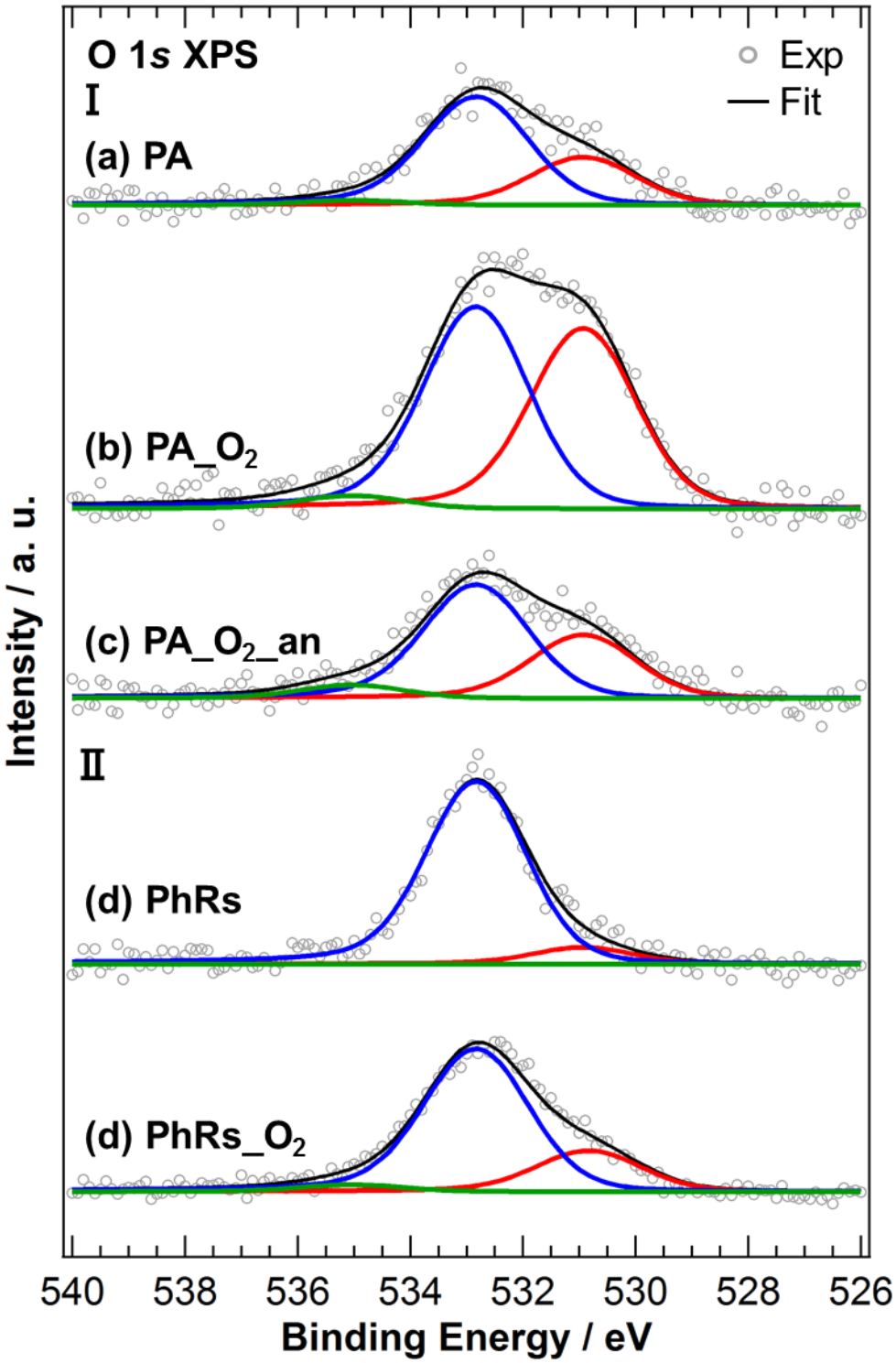

Fig. 3.4. O 1*s* XPS spectra of (I) PA and (II) PhRs. (a) and (d) show annealed samples before O_2 adsorption. (b) and (e) show O_2 adsorbed samples. (c) shows reannealed sample after O_2 adsorption. Gray open circle and black line represent raw data and fitting results. Red, blue, and green lines are C=O groups (OP1); C-OH and C-O-C groups (OP2); and chemisorbed oxygen or water (OP3) components, respectively.

Figure 3.5 shows N 1*s* XPS spectra of PA and PhRs before O_2 adsorption, after O_2 adsorption, and after O_2 desorption. The spectra are normalized to the atomic ratio of each sample shown in Table 3.3. The N 1*s* XPS spectra are decomposed into four peaks (NP1-NP4) and their atomic ratio N/C as well as relative composition ratio is summarized in Table 3.5. The terminology of nitrogen components used hereafter is shown in Fig. 3.6. Peak NP1 around 398.3-398.5 eV is pyridinic N bonded to two carbon atoms in a graphitic sp^2 network [68,69]. Peak NP2 around 399.9-400.2 eV is a mixture of pyrrolic N formed in a five-membered ring [68] and amide N that contains a functional group consisting of a carbonyl group (R-C=O) linked to a nitrogen atom [70]. Peak NP3 around 401.0-401.2 eV is assigned to the graphitic N which is hybridized with three carbon atoms in the sp^2 network [69,71,72]. Peak NP4 around 402.9-403.8 eV is assumed to the Oxide N which bonds to an oxygen atom [68].

The N/C ratio of PA before O_2 adsorption, after O_2 adsorption, and after O_2 desorption is 0.059, 0.060, and 0.059, respectively, shown in Table 3.3, indicating that nitrogen incorporated into PA doesn't decrease from 56% to 47% through O_2 adsorption and desorption. However, the relative composition ratio significantly changes before and after O_2 adsorption in PA. The relative ratio of graphitic N (NP3) decreased and that of pyridinic N (NP1) and pyrrolic/amide-like (NP2) N increased, while that of oxide N was almost constant. The similar change in the nitrogen composition is found in a CN_x film etched by the oxygen ion beam [73,74]. They reported that the amount of the oxide N did not increase through O_2 ion beam etching, indicating that O_2 does not directly reacts with nitrogen atoms. Therefore, O_2 would be adsorbed on a particular site close to the graphitic N and indirectly change the chemical state of the graphitic N. The relative composition ratio of the graphitic N increased from 47 % to 53 % after O_2 desorption while the total nitrogen content remained unchanged, suggesting that graphitic N was reproduced by reannealing. Thus the nitrogen-containing O_2 adsorption sites in PA have reversible characteristics for O_2 adsorption and desorption.

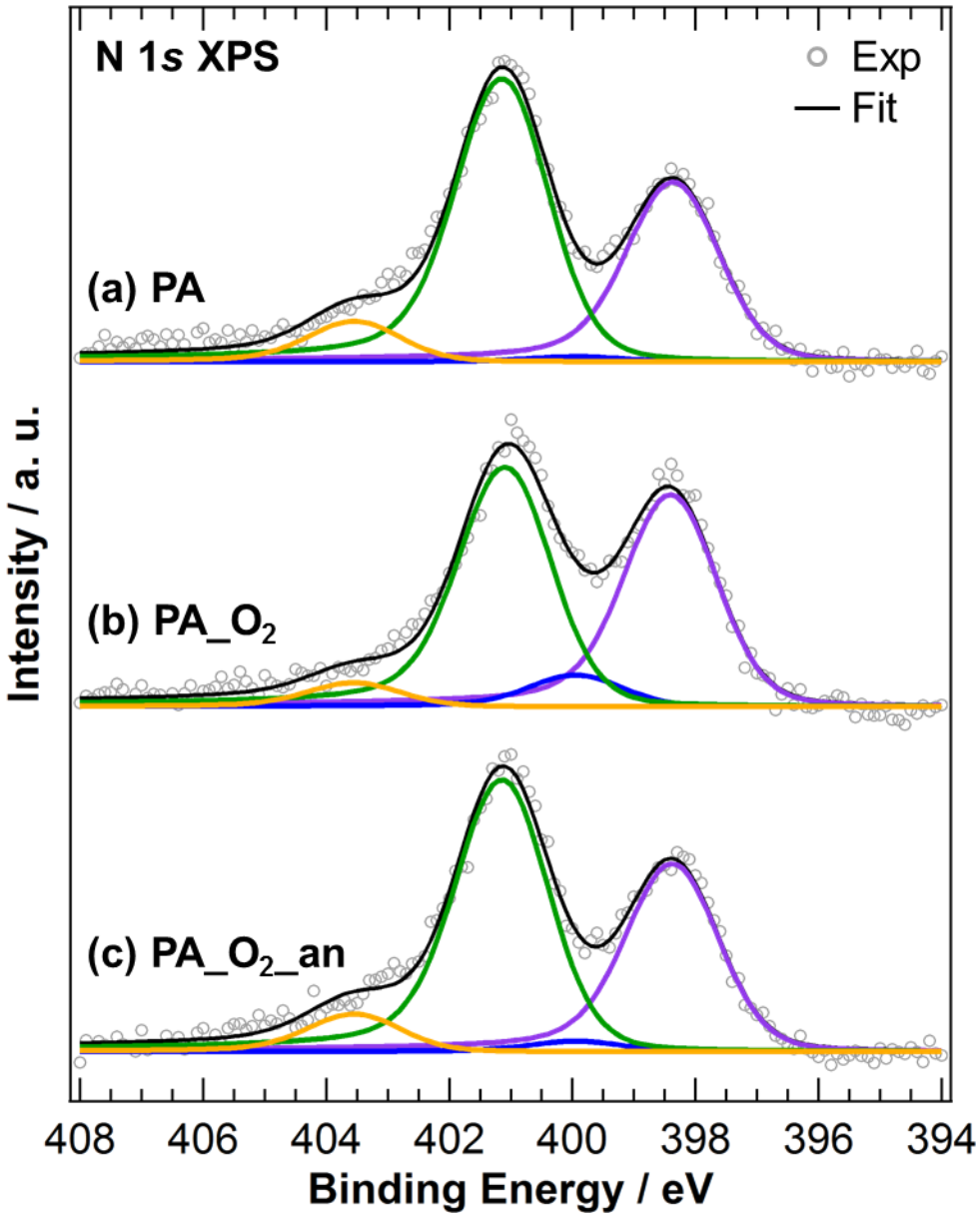

Fig. 3.5. N 1*s* XPS spectra of PA (a) before and (b) after O_2 adsorption. (c) shows reannealed sample after O_2 adsorption. Gray open circle and black line represent raw data and fitting results. Purple, blue, green, and orange solid lines are pyridinic N (NP1); pyrrolic and amide-like N (NP2); graphitic N (NP3); and oxide N (NP4) components, respectively.

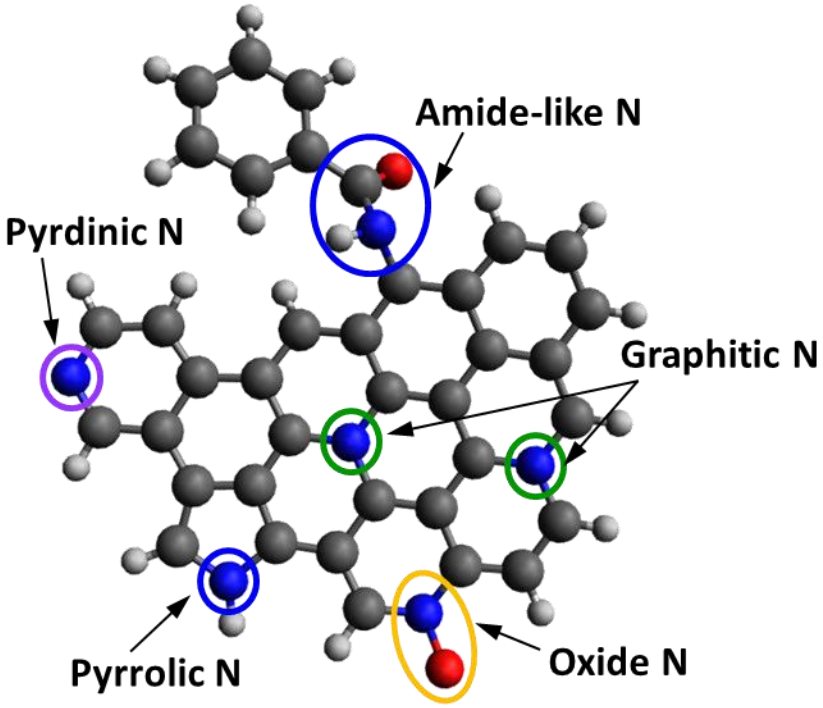

Fig. 3.6. Local geometry for various nitrogen components in graphite. Gray, blue, red, and white balls represent carbon, nitrogen, oxygen, and hydrogen atoms, respectively.

Table 3.5 The N/C ratio and the relative composition ratio of four nitrogen components calculated form XPS fitting results in each sample

Sample	N/C ratio	Relative composition ratio / %			
		Pyridinic N	Pyrrolic N Amide-like N	Graphitic N	Oxide N
PA	0.059	36	1	56	8
PA _O_2	0.060	42	6	47	5
PA _O_2_an	0.059	37	2	53	7

Figure 3.7 shows C 1*s* XPS spectra of PA before O_2 adsorption, after O_2 adsorption, and after O_2 desorption. The spectra are normalized to the peak area. The each dotted line (CP1-4) denotes the carbon functional groups. Peak CP1 around 286.2 ± 0.1 eV is derived from carbon atoms present in alcohol C-OH, phenolic, ether C-O-C or C=N groups. Peak CP2 around 287.4 ± 0.2 eV is derived from carbon atoms present in carbonyl or quione >C=O groups. Peak CP3 around 288.6 ± 0.3 eV is derived from carbon atoms present in carboxylate –C(=O)OH or ester O-C(=O)-R groups. Peak CP4 around 290.6 ± 0.2 eV is derived from carbon atoms present in carbonate O-C(=O)-O groups, CO, and CO_2 [67]. Although the amount of the adsorbed O_2 increased by 1.6 at.% and the relative ratio of the C=O component increased preferentially after O_2 adsorption, it is difficult to detect the little change of C 1*s* spectra profiles since this change is expected to about 2% at maximum. Similar results are also observed in PhRs. This changeless C 1*s* profiles indicate most of the carbon structure in PA and PhRs does not change dramatically after O_2 adsorption.

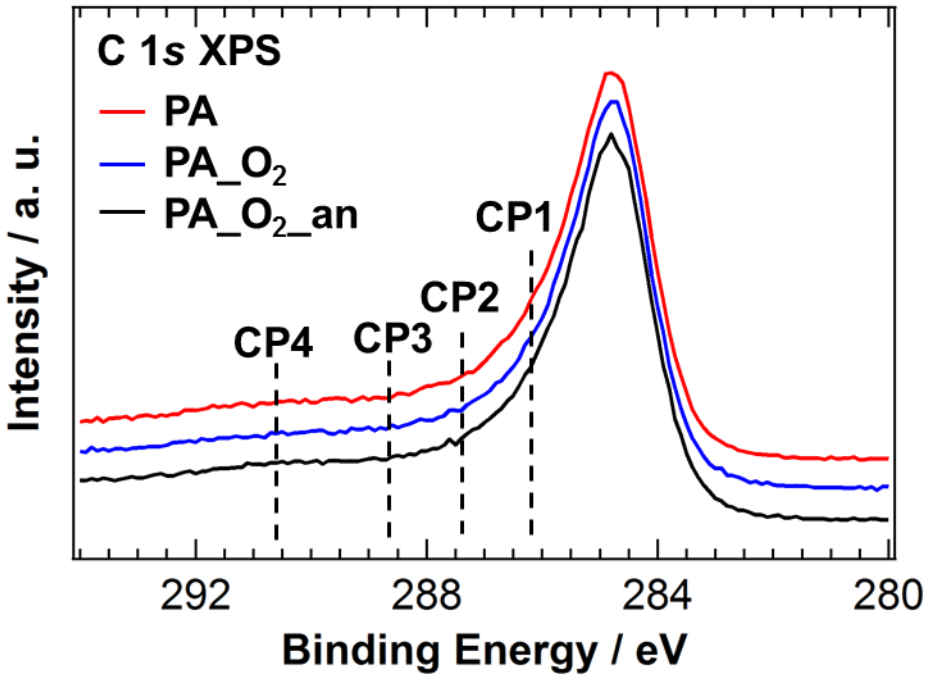

Fig. 3.7. C 1*s* XPS spectra of PA. PA, PA_O_2, and PA_O_2_an denote PA before O_2 adsorption, after O_2 adsorption, and after reannealing, respectively.

3.3.5 Oxygen adsorption sites and related ORR mechanism

The decrease in the relative amount of graphitic N has been observed while little change in oxide N after O_2 adsorption to PA, indicating that O_2 adsorbs on carbon atoms close to the graphitic N. Since PA has high selectivity to the 2-electron ORR, the graphitic N may contribute to the 2-electron ORR process. Sidik *et al.* have suggested that carbon radical sites formed adjacent to graphitic N in the basal plane are active for O_2 reduction to H_2O_2 in acid electrolyte and the adsorbed O_2 could also be reduced to H_2O by the 4-electron ORR [41]. Therefore their model seems to support the observed change in the N 1*s* XPS spectra. However, Ikeda *et al.* suggested by first principles calculation that O_2 adsorption energy for a carbon atom next to the graphitic N in the basal plane is quite high (~330 kJ mol^{-1}) [42]. The preferential production of carbonyl (C=O) group after O_2 adsorption to PA has been observed. It is well known that functional groups on a carbon surface, such as quinone/hydroquinone and carbonyl/hydroxyl groups, enhance electrochemical reactions mainly related to the 2-electron ORR process [75,76]. Thus the created carbonyl group in PA would be active for the 2-electron ORR process.

Several groups have suggested that the incorporated nitrogen atoms reduce potential barrier to make various defect sites [62,77] (such as ad-dimer defect [78,79], Stone-Wales defect [80], mono-vacancy [81], divacancy [82], edge [42,83] and so on), which would enhance O_2 adsorption and the subsequent ORR processes. Ghaderi *et al.* calculated that the Stone-Wales defect, which is composed by two pairs of a five-membered ring and a seven-membered ring in Fig. 3.8 (a), stabilized the hydroxyl group OH [80]. In addition, Terakura *et al.* reported by molecular dynamics (MD) calculation that O_2 adsorption in the Stone-Wales defects with graphitic N at a specific site induces the C-N bond breaking and the adsorbed O_2 exists in the form of C-O-O structure in Fig. 3.8 [84]. In other carbon defects such as the ad-dimer (inverse Stone-Wales) defect, which is also composed by the different type of two pairs of a five-membered ring and a seven-membered ring in Fig. 3.9, Horner *et al.* calculated that the adsorbed O_2 on this defect is stabilized [79]. Moreover, Terakura *et al.* also reported by MD calculation that the ad-dimer defect with graphitic N at a specific site can adsorb an O_2 molecule and the subsequent C-N bond breaking generates the pyridinic N, epoxide, and carbonyl groups in Fig 3.9 [84]. From the above theoretical calculations, it

would be expected in current catalyst that the O_2 adsorption causes the C-N bond breaking between the graphitic N and the carbon atom incorporated into the carbon defect structure due to the O_2 adsorption.

Therefore, the whole mechanism expected from the *in situ* XPS analyses is as follows; among the incorporated nitrogen in PA, the graphitic N located in the defect sites enhances O_2 adsorption to PA and the adsorbed oxygen itself is incorporated in the form of carbonyl group, which may become active sites for the 2-electeorn ORR. Note that there is also another possible mechanism that the first adsorbed oxygen (C=O) species itself is reduced to H_2O_2. This is the first XPS result of O_2 adsorption to CACs and the technique is applicable to any other ORR catalysts.

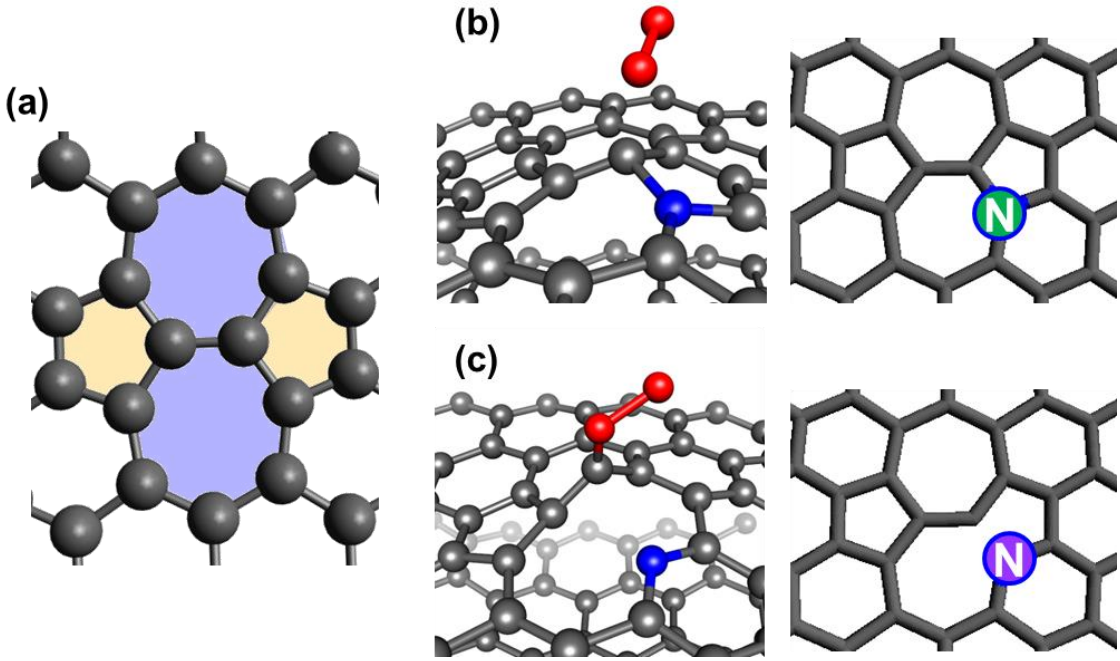

Fig. 3.8. Schematic images of (a) Stone-wales defect and Stone-Wales defect with a nitrogen atom (b) before and (a) after O_2 adsorption.

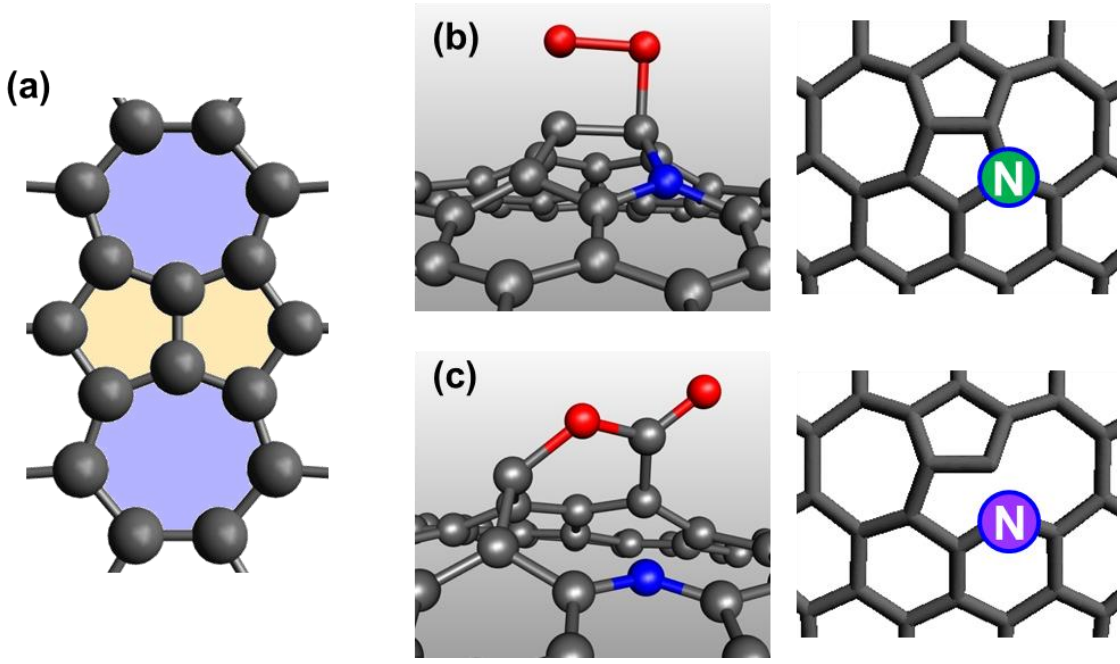

Fig. 3.9. Schematic images of (a) ad-dimer defect and ad-dimer defect with a nitrogen atom (b) before and (a) after O_2 adsorption.

3.4 Conclusions

The characteristics of O_2 adsorption on nitrogen-containing metal-free CACs were investigated and the possible ORR mechanism was elucidated using RRDE, Raman spectroscopy, O_2 adsorption isotherm and *in situ* XPS. RRDE measurements and Raman spectroscopy showed that nitrogen-containing PA has higher ORR activity, higher selectivity of the 2-electron ORR process, and more carbon defect sites than nitrogen-free PhRs. O_2 adsorption isotherm revealed the O_2 chemisorbed on CACs and the doped nitrogen components enhance O_2 adsorption. N 1*s* *in situ* XPS results showed that the graphitic N contributes to the O_2 adsorption process, which is the first step of ORR, with the C-N bond breaking. O 1*s* *in situ* XPS results showed the adsorbed oxygen are dominantly C=O components in PA. These results indicate that the graphitic N in the defect sites enhances O_2 adsorption and two possible 2-electron ORR processes; i.e. reduction of the adsorbed O_2 to H_2O_2 or the adsorbed oxygen itself, which forms quinone or carbonyl groups, becomes active sites for 2-electron ORR.

Chapter 4

Characterization of nitrogen-doped graphite using low energy nitrogen ion sputtering

4.1 Introduction

Nitrogen doping of carbon-based materials such as graphene, carbon nanotubes, and graphite is an effective way to tailor their electronic, chemical, optical, and magnetic properties. In particular, carbon-based oxygen reduction catalysts are expected to be alternatives to high cost Pt-based cathode catalysts for PEFCs [20,24,29,30,85–88]. In the last decade, there are various theoretical [42–44] and experimental [89–91] studies on the roles of pyridinic and graphitic nitrogen in ORR activity. In a diverse range of nitrogen-doping methods, including chemical vapor deposition [85,86], pyrolysis of nitrogen containing polymers [20,24,87], pyrolysis of the nitrogen source mixture [20,24,29,30,87,88,91], and nitrogen ion sputtering [92], a complicated relationship exists nitrogen doping and ORR activity because many parameters, such as morphology, surface area, and crystallinity, are involved. It is therefore essential to prepare a well-defined reference system exhibiting not only high crystallinity and surface morphology, but also possessing select nitrogen species in order to determine the relationship between nitrogen configuration and ORR activity. In this respect, highly oriented pyrolytic graphite (HOPG) is expected to provide a well-defined surface due to its ordered sp^2-carbon network.

The low energy nitrogen ion sputtering (8-4000 $\times$ 10^{13} ions cm^{-2}) to HOPG was performed in order to realize effective nitrogen doping (N = 0.4-8.4 at.%) while retaining the flatness of the surface sp^2-carbon structure. The chemical states of the doped nitrogen will be controlled by altering the amount of impinging nitrogen ions and the nitrogen species was clarified using a combination of X-ray and Raman

spectroscopic analyses. The characterized N-HOPG was investigated the electrochemical properties in order to discuss the possible ORR active site.

4.2 Experimental methods

The detailed preparation of N-HOPG was described in Chapter 2.1.2. The typical amounts of dosed nitrogen ions were calculated to be 8×10^{13}, 8×10^{14} and 4×10^{16} ions cm^{-2}, equivalent to 2%, 21%, and 1030% nitrogen ions, respectively, with respect to surface carbon atoms.

XPS was performed at BL27SU in SPring-8 using a photoelectron analyzer (PHOIBOS 150, SPECS GmbH), with 850 eV incident photon energy. Backgrounds of the core level spectra were subtracted using the Shirley method. The N 1*s* XPS spectra were fitted with Voigt functions (0.98 eV Gaussian width and 0.25 eV Lorentzian width). The energy resolution of XPS at BL27SU was 170 meV. Conventional laboratory-based XPS was also performed using a monochromatic and a non-monochromatic Al-$K\alpha$ source (JPS-9010, JEOL Ltd.) with energy resolutions of 0.7-0.8 eV and 1.1-1.3 eV, respectively. XAS spectra were measured by the PEY mode in order to increase surface sensitivity. XAS spectra were obtained at BL27SU and BL07LSU in SPring-8 by setting θ to 0°, 45°, 60°, or 70°. The angle, θ, is defined as the angle between the incident X-ray beam axis and the surface normal. The spectra were fitted with six Gauss functions for the π^* and σ^* states, and two step functions convoluted by error function and exponential decay function for the continuum states in the π^* and σ^* regions [57]. The detailed fitting method was described in Chapter 2.4.3. The energy resolution of XAS had a lower limit below 100 meV. The samples were annealed at 900 K for 30 min to remove the initially adsorbed gas before XPS and XAS measurements were carried out. For each sample, the nitrogen content remained constant both before and after annealing, while the oxygen contamination percentage decreased dramatically (<0.15 at.%) after annealing.

Raman spectroscopy was performed using a micro-Raman spectrometer (NR-1800, JASCO Corp.) with an excitation wavelength of 532 nm. The Raman spectral resolution was 2.6 cm^{-1}.

A Monte Carlo simulation tool, Stopping and Range of Ions in Matter (SRIM) [93], was used to estimate the depth profile of doped nitrogen ions in HOPG sputtered with

N_2^+ ions. This simulation tool yields the distribution of implanted ions, vacancies, and sputtered ions, along with surface defects. In this sputtering process, the initial kinetic energy (200 eV) was equally distributed among the N_2^+ ions [94]. Ion energy, lattice binding energy [95], surface binding energy [96], and displacement energy [96] were set at 100 eV, 3 eV, 7.41 eV, and 35 eV, respectively. In this case, ion energy is the incident energy of a nitrogen atom, and the lattice binding energy is the minimum energy required to remove an atom from its lattice site. In addition, the surface binding energy is the energy required to remove an atom at the target surface, and can be estimated from the heat of sublimation. Finally, the displacement energy is the minimum energy required to knock a target atom from its lattice site.

The ORR activity of N-HOPG was evaluated at room temperature in a 0.1 M H_2SO_4 electrolyte solution. The preparation method of the N-HOPG electrode was described in Chapter 2.2. The working electrode, counter electrode, and reference electrode were N-HOPG, Pt wire, and a reversible hydrogen electrode, respectively. Linear sweep voltammograms (LSV) were recorded by sweeping the potential from 1.1 V to -0.05 V (vs. RHE) at 5 mV s^{-1} in a saturated N_2 or O_2 gas electrolyte. The ORR current was determined by subtracting the N_2 data from the O_2 data. Current density was obtained as measured current divided by the electrode HOPG surface area (*e.g.* ~0.15 cm^2) rather than actual surface area, as the surfaces of all N-HOPG samples were flat, with no clear difference being observed based on the atomic force microscopy (AFM) analysis in Fig. 3.7.

4.3 Results and discussion

4.3.1 Chemical states of doped nitrogen in N-HOPG

Using the SRIM Monte Carlo simulation tool [93], we found that the doped nitrogen atoms were distributed near the surface region of HOPG as shown in Fig. 4.1 (projected range up to 2 nm). It was observed that the accelerated nitrogen ions create a 2-3 nm thick nitrogen-doped region at the surface of the HOPG substrate. Since the nitrogen doped region is thinner than the probing depth of XPS and XAS with PEY, all doped nitrogen can be detected by both XPS and XAS.

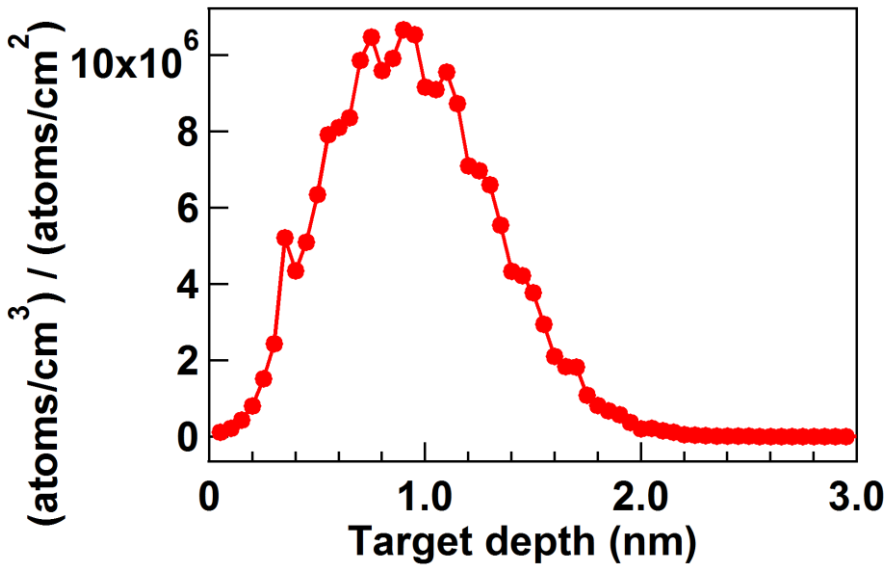

Fig.4.1. The simulated depth profile of doped nitrogen atoms on HOPG.

From the XPS spectra, the amount of surface nitrogen (X) was estimated to be 0.4, 2.3, and 8.4 at.% for N-HOPG samples prepared by doping with 2, 21, and 1030% nitrogen ions, respectively. Kondo *et al*. previously reported the N 1*s* XPS spectrum of N-HOPG produced by low energy (200 eV) nitrogen ion sputtering [49]. In this case, nitrogen content was 2.7 at.%, and the profile of N 1*s* spectra was similar to that of N-HOPG with X = 2.3 (at.%) in this manuscript. The amount of dosed nitrogen ions in the previous work was not measured but thus can be estimated around 80×10^{13} ions cm^{-2}. On the other hand, the total ion doses were lower than 0.2×10^{13} ions cm^{-2} for the STM measurements. Therefore, we have for the first time reported the ion dose effects between 0.2 and 80×10^{13} ions cm^{-2}; in particular emphasis is on 8×10^{13} ions cm^{-2}. The higher ion dose effect for 4000×10^{13} ions cm^{-2} was also reported.

Figure 4.2 shows the N 1*s* XPS spectra of N-HOPG with X = 0.4, 2.3, and 8.4. In addition, the N 1*s* XPS spectra at low nitrogen content region with low energy resolution (ΔE = 1.1-1.3 eV) are shown in Fig. 4.3. All spectra were normalized by the integrated intensity. As can be seen, the spectra are fitted with five Voigt functions, denoted as NP1 (398.0-398.5 eV), NP2 (399.9 eV), NP3 (400.9 eV), NP4 (401.9 eV), and NP5 (403.5 eV). The binding energy was treated as a fixed parameter except for NP1. The terminology of nitrogen components used hereafter is defined in Fig. 4.4.

NP1 represents pyridinic N where one nitrogen atom is connected with two carbon atoms. The peak positions at X = 0.4 and 2.3 are 398.0 eV and slightly lower than the reported one (398.5-398.9 eV) [86]. Although pyridinic N usually exists in the graphite edge, the majority of pyridinic N atoms in N-HOPG exist in the vicinity of in-plane defects at the beginning of nitrogen ion sputtering due to the small amount of graphite edge in HOPG. The difference between in-plane pyridinic N and pyridinic N in edges would induce the chemical shift. On the other hand, the peak position of pyridinic N at X = 8.4 is 398.5 eV [86]. The agreement with the previous report would results from the dominant number of pyridinic N at edges created by the large number of sputtering ions. NP2 represents cyanide N, where a triple bond is formed between a nitrogen and a carbon atom [70], or pyrrolic N where one nitrogen atom is connected with two carbon atoms and one hydrogen atom in a five-membered ring [68]. NP3 corresponds to graphitic N in the basal plane [69], which substitutes the carbon site in the graphite basal plane, forming a nitrogen site bonded to three carbon atoms. NP4 would be valley

N where one nitrogen atom substitutes the carbon site in the zigzag edge and/or vacancy sites in Fig. 4.4 [91,97]. From the theoretical reports, Casanovas *et al*. used cluster calculations to suggest that the peak position of graphitic N in the zigzag edge shifts to higher binding energy by approximately +1.0 eV compared to that of the in-plane graphitic N [69]. Wang *et al.* also estimated the binding energy separation of the same chemical components to be approximately +0.6 eV [98]. From the experimental results, the presence of the zigzag edge even in HOPG has been reported by STM [99], with step densities of 0.09-2.2% being recorded for a variety of HOPG grades using AFM [100]. The nitrogen sputtering process not only causes nitrogen doping but also creates carbon vacancies. Such carbon vacancies can contribute to the formation of pyridinic N and valley N. For a graphene on Ir (111) with 25 eV N^+ plasma treatment, Orlando *et al.* observed a peak around 401.9 eV and assigned it to valley N based on the XPD study [101]. Because graphene on a metal substrate forms a Moire structure by the mutual interaction, there was another possibility that the peak around 401.9 eV results from the chemical shift of graphitc N (400.9 eV). However, Orlando *et al*. excluded the possibility because the interaction between graphene and Ir(111) was weak [102], thus supporting my assignment. The more detailed doping dependence of N 1*s* XPS spectra was shown in Fig. 4.3 and confirmed the existence of NP4 peak at low nitrogen content. From these theoretical and experimental results, it seems therefore most plausible to assign NP4 to valley N. It should be noted that there is not yet strong evidence to visualize the local atomic structure of valley N using atomic scale microscopy such as STM and AFM and the assignment is not conclusive. Finally, NP5 represents oxide N, which forms direct bonds with oxygen atoms.

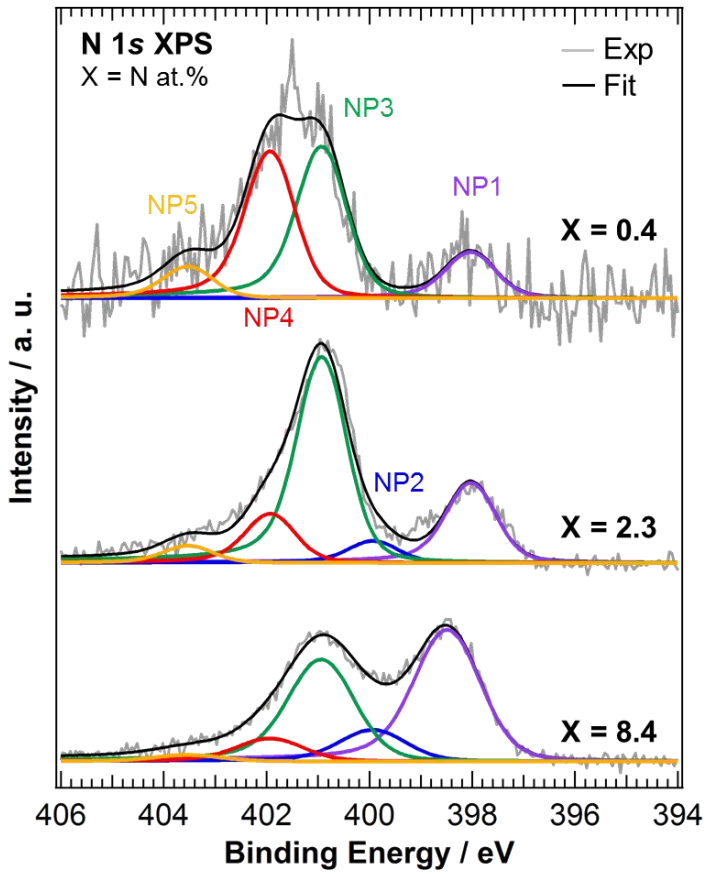

Fig. 4.2. (a) N 1*s* XPS spectra of N-HOPG (X = 0.4, 2.3, and 8.4). The energy resolution was 0.17 eV in N-HOPG with X =0.4 and 2.3, however, 0.7-0.8 eV in N-HOPG with X = 8.4. Purple, blue, green, red, and orange lines correspond to NP1 (pyridinic N), NP2 (cyanide N or pyrrolic N), NP3 (graphitic N), NP4 (valley N), and NP5 (oxide N), respectively. Gray and black lines represent raw and fitting results, respectively.

Table 4.1. Nitrogen atomic ratio of each nitrogen component in N-HOPG (X = 0.4, 2.3, and 8.4)

N content	Atomic ratio of each N component / at.%				
(X = N at.%)	Pyridinic N	Pyrrolic N	Graphitic N	Valley N	Oxide N
X = 0.4	0.04	0.0	0.14	0.14	0.03
X = 2.3	0.48	0.13	1.23	0.29	0.10
X = 8.4	3.78	0.91	2.88	0.65	0.17

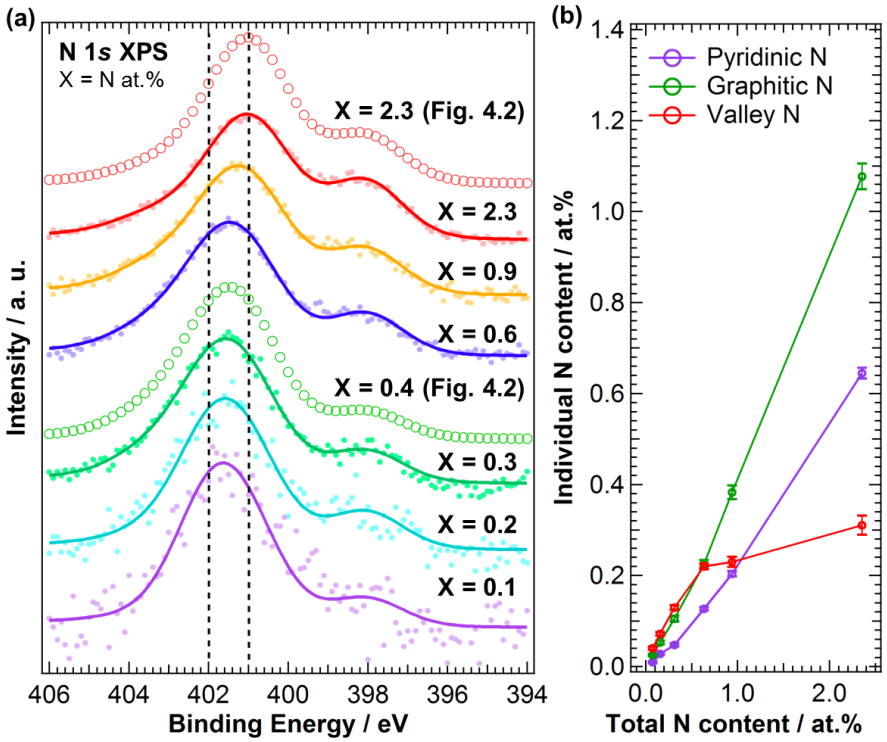

Fig. 4.3. (a) N 1*s* XPS spectra of N-HOPG measured with a non-monochromatic Al-Kα source and calculated fitting results in Fig. 4.2 (X = 0.4 and 2.3) using comparable Gaussian width. Closed circles, solid lines, and open circles present raw data, fitting results, and calculated fitting results, respectively. (b) The amounts of individual nitrogen components as a function of total nitrogen content.

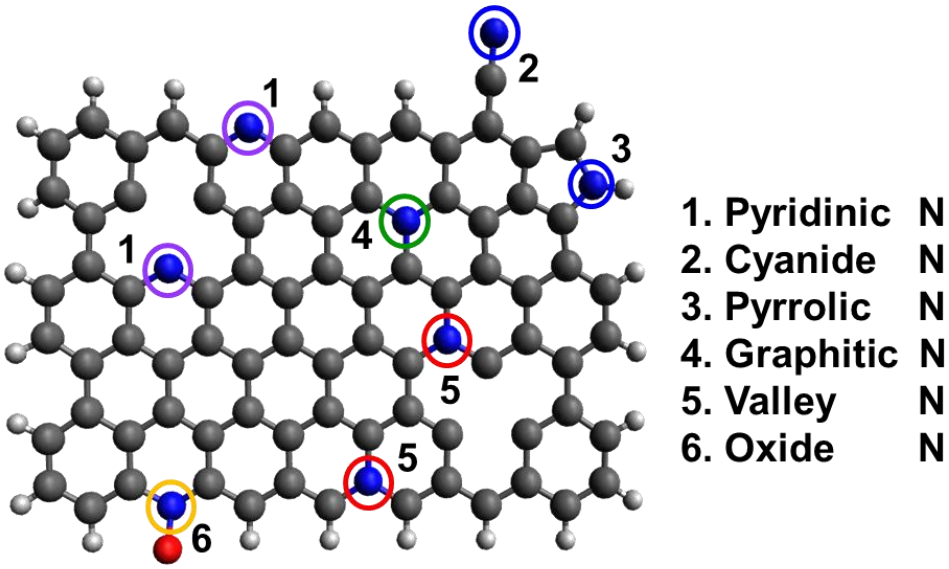

Fig. 4.4. A schematic representation of the nitrogen components. Hydrogen, carbon, nitrogen, and oxygen atoms correspond to white, black, blue and red balls, respectively.

Graphitic N (NP3) and valley N (NP4) components were found to be dominant in N-HOPG with X = 0.4 and X = 2.3, which correspond to more than 70% of the total nitrogen content. Pyridinic N was the next common component. It was found that the relative ratio of pyridinic N gradually increased with increasing total amount of doped nitrogen, *i.e.* 13% in N-HOPG with X = 0.4, 21% in N-HOPG with X = 2.3, and >40% in N-HOPG with X = 8.4. In graphene sputtered with nitrogen ions, a continuous increase in pyridinic N correlates to a greater amount of defects and some carbon loss [103]. Thus, it was clear that the formation of the defects in graphite is suppressed by the low nitrogen concentration. The amount of pyridinic N, graphitic N, and graphitic N increases in proportion to the total nitrogen content under X = 0.6, however, that of valley N increases a little over X = 0.9 in Fig. 4.3 (b). The relative ratio of valley N in Fig. 4.2 also decreased from 39% in N-HOPG with X = 0.4 to 13% in N-HOPG with X = 2.3. This counterintuitive feature of valley N can probably be explained as follows. Graphite retains flat surface under N-HOPG with X = 0.6 as later mentioned at 4.3.3. Above N-HOPG with X = 2.3, however, the carbon network was strongly disturbed and amorphized. At the low nitrogen doing region, the sputtering creates defects, such as zigzag edges and point vacancies, whereas at the high nitrogen doping region, the sputtering creates more defects resulting in disorder of several carbon layers, that is, amorphous carbon as discussed in the previous study of Ar^+ sputtering to single- and few-layer graphenes [104]. The zigzag edges and point vacancies contribute to the formation of both pyridinic N and valley N. Therefore, at the low doping region, the absolute amount of pyridinic N and valley N increases in proportion to the total ion dose (Fig. 4.3 (b)). At the high doping region, however, the evolution of the amorphous carbon (Fig. 4.8) prevents the formation of valley N (Fig. 4.3 (b)). Therefore, it was amorphization of carbon that drastically reduced the proportion of valley N at high doping region.

4.3.2 Configuration of doped nitrogen in N-HOPG

The configuration of doped nitrogen in N-HOPG was analyzed by angle-dependent N 1*s* XAS in Figs. 4.5 and 4.6. The spectra were normalized according to intensity at 430 eV, taking an average between 390-395 eV as background. Out-of-plane ($\theta = 90°$) unoccupied states of nitrogen were extracted by taking into account their contribution to the obtained ($\theta = 0°$, 45°, 60°, or 70°) spectra (Fig. 4.5). Figure 4.6 shows the in-plane ($\theta = 0°$) and the extracted out-of-plane ($\theta = 90°$) N 1*s* XAS spectra. Three sharp peaks in the π* region can be assigned to (A) pyridinic N, (B) cyanide N, and (C) graphitic N sites [51,60,105], respectively, where the presence of pyrrolic N could be excluded by XAS rather than XPS because the peak position of the pyrrolic N was calculated as ~402 eV [106]. In addition, peak D corresponds to the σ* states. The intensities of pyridinic N (A) and graphitic N (C) for the low nitrogen content (N-HOPG with X = 0.4 and 2.3) strongly depend on the X-ray incident angle. Since the similar angle dependence is observed in the carbon π* state of HOPG (C 1*s* XAS) [107], those nitrogen species are incorporated into the graphite basal plane to give a planar N-HOPG structure under low nitrogen doping conditions. The simulation of both in-plane and-out-of-plane XAS spectra has been reported by Hou *et al.* using density functional theory (DFT) calculations [108]. They reported that both a graphitic N in perfect graphene, and a pyridinic N with a monovacancy show perfect polarization dependence for π* and σ* components. Therefore, graphitic N and pyridinic N are doped into the planar graphene lattice *via* substitution. In this N-HOPG preparation method, two main factors can facilitate the formation of the planar structure. Firstly, the low acceleration voltage of ions (200 eV) maintains the nitrogen ions at the surface of the graphite layer and reduces the collapse of the graphite basal plane by recoil effects. Secondly, the post-annealing step at 1000 K reduces defects and removes excess nitrogen from the N-HOPG.

However, in highly nitrogen-doped systems (N-HOPG with X = 8.4), this polarization dependence is less distinct when the same preparation method is used. The decrease in polarization dependence is clearly shown in Table 1, where the degrees of the orientation of each nitrogen component are expressed by the intensity ratio [π*/σ* (at $\theta = 90°$)]/[π*/σ* (at $\theta = 0°$)] where π* and σ* represent the integrated intensity of the Gaussian functions for the π* (A, B, C) and σ* (D) components, respectively. In the

case of pyridinic N (A), the intensity ratios were >100 for X = 0.4 and 2.3, while a smaller ratio of ~10 was observed for X = 8.4. Similarly, the intensity ratios of graphitic N (C) decrease with increasing amount of nitrogen, *i.e.*, 290 for X = 0.4, 110 for X = 2.3, and 9 for X = 8.4. Thus, by increasing the amount of nitrogen ion sputtering, the number of nitrogen atoms incorporated in such defective and non-planar structures increases. This results in a lesser polarization dependence in the N 1*s* XAS spectra. The orientation of nitrogen sites is therefore gradually randomized from N-HOPG with X = 0.4 to N-HOPG with X = 8.4. It has also been reported by simulations that excessively high nitrogen content in the graphite lattice (X >20 at.%) can result in loss of the planar structure [109]. However, a small polarization dependence is still present, even in the doped nitrogen saturated N-HOPG where X = 8.4, suggesting that each doped nitrogen may be incorporated into the relatively flat N-HOPG surface. In contrast to pyridinic N and graphitic N, cyanide N (C) shows less polarization dependence with all N-HOPG samples, since it is not implemented in the graphite basal plane [105].

In the XAS spectra at $\theta = 90°$, the intensity ratio of pyridinic N (A) to graphitic N (C) increased from 0.37 (X = 0.4) to 0.53 (X = 2.3), which is the same trend as the intensity ratio of pyridinic N (NP1) to graphitic N and valley N (NP3 + NP4), with an increase from 0.16 (X = 0.4) to 0.32 (X = 2.3) in the XPS spectra. However, it should be noted that the valley N peak could not be identified in the XAS spectra, possibly due to overlap with the graphitic N (C) peak, while in the XPS spectra a different peak position allowed the two environments to be distinguished. As discussed for the pyrrolic N in this manuscript, the chemical shifts in XAS and XPS are not necessarily the same [106]. The assignment of the valley N species in the XAS spectra will therefore be investigated in a future study.

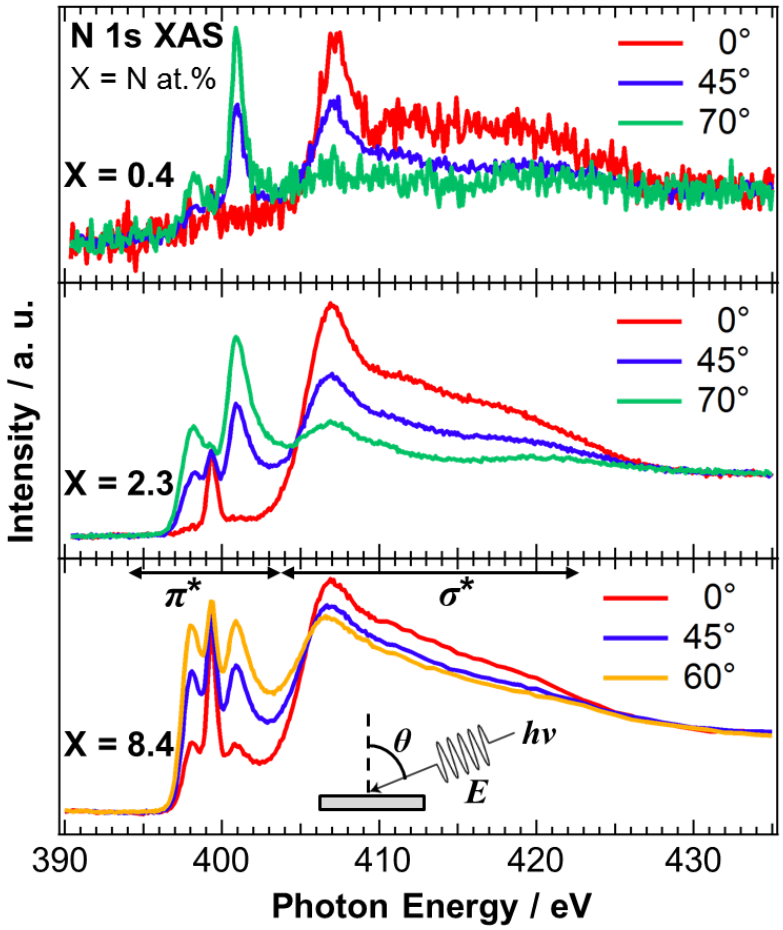

Fig. 4.5. N 1*s* XAS spectra of N-HOPG (X = 0.4, 2.3, and 8.4). Red, blue, orange, and green lines correspond to the spectra obtained with incident angles θ = 0°, 45°, 60°, and 70°.

Table 4.2. The degrees of the orientation of each π* peak (pyridinic N, cyanide N, and graphitic N) estimated by [π*/σ*] (at θ = 90°) / [π*/σ*] (at θ = 0°)

N content	[π*/σ*] (at θ = 90°) / [π*/σ*] (at θ = 0°)		
(X = N at.%)	Pyridinic N	Cyanide N	Graphitic N
X = 0.4	130	21	292
X = 2.3	120	5	112
X = 8.4	10	4	9

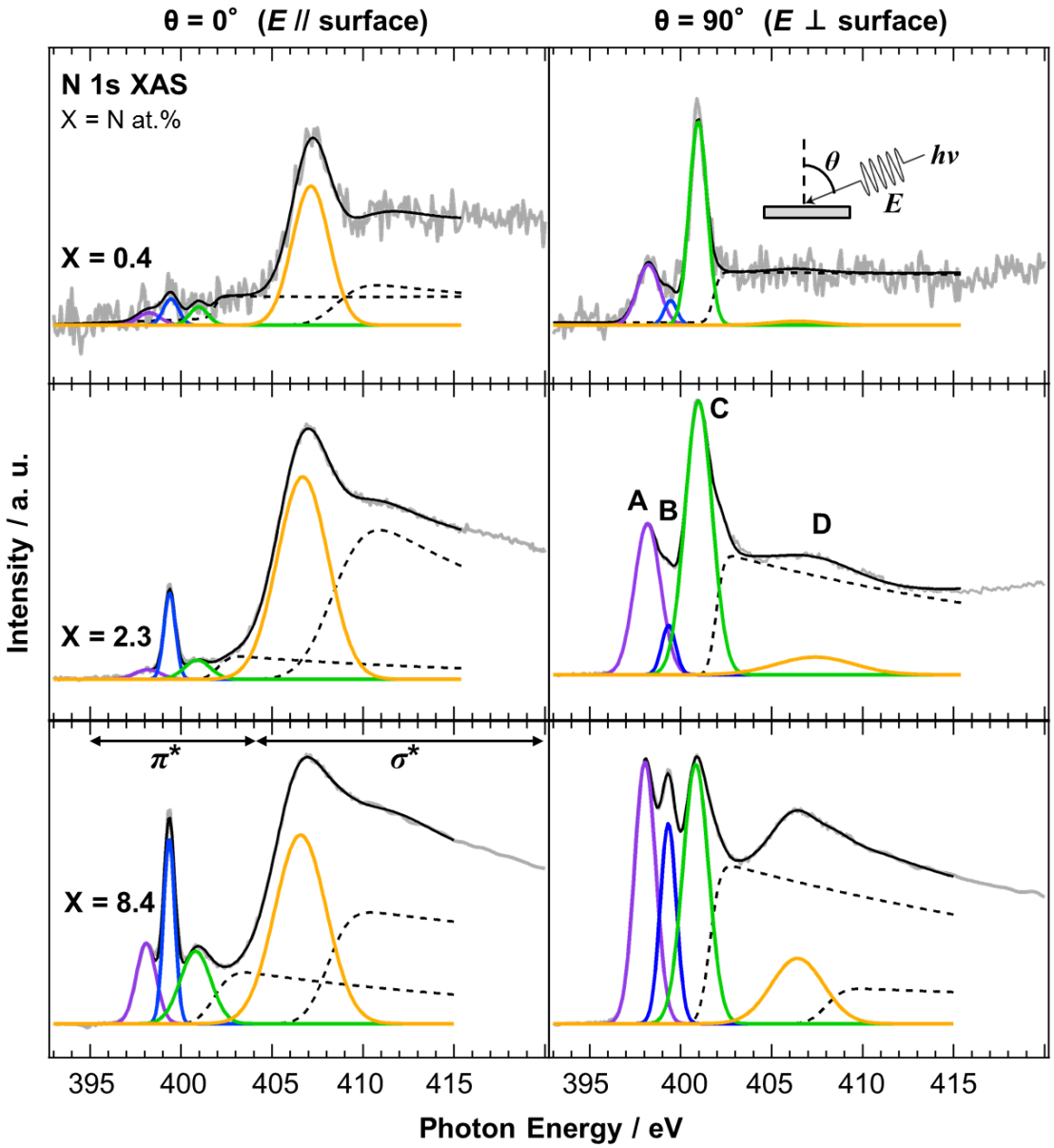

Fig. 4.6. N 1*s* XAS spectra of N-HOPG (X = 0.4, 2.3, and 8.4). The spectra at θ = 90° and 0° are shown on the left and right hand panels, respectively. Purple, blue, and green lines correspond to pyridinic N (A), cyanide N (B), and graphitic N (C) in the π* region, respectively. Orange line exhibits the lowest energy σ* peak (D). An additional Gaussian function for the higher energy σ* component is not shown here. Dashed lines represent step functions which correspond to continuum states of π* and σ* regions. Gray and black lines represent raw data and fitting results, respectively.

4.3.3 Surface morphology and defect sites

Figure 4.7 shows AFM images of the N-HOPG to investigate the surface morphology difference. The surfaces of the N-HOPG samples were flat with no distinct differences, implying that the nitrogen doping followed by an annealing process did not significantly affect the specific surface areas of the prepared samples.

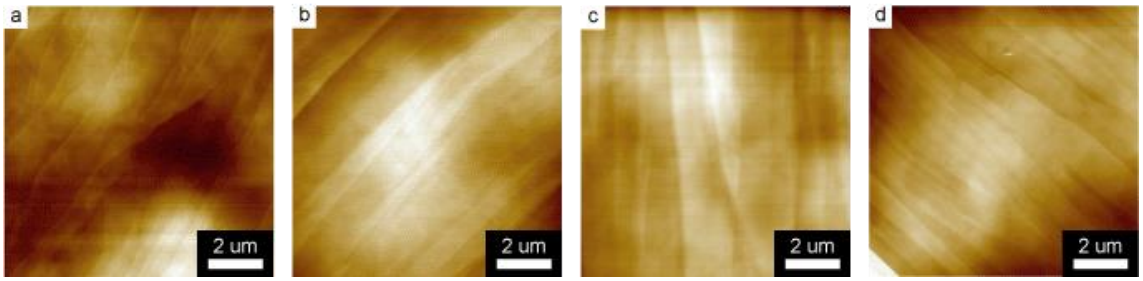

Fig. 4.7. AFM images of the N-HOPG (X = 0.4 (a), 2.3 (b), and 8.4 (c)) and clean HOPG (d).

Raman scattering measurements provide additional information regarding the disorder in the carbon structure. Figure 4.8 shows Raman spectra of each N-HOPG and clean HOPG (X = 0.0) as reference. The spectra were normalized according to peak height at 1585 cm^{-1}. The G-band at approximately 1585 cm^{-1} is derived from the graphite basal plane, while the D-band at ~1360 cm^{-1} corresponds to defect sites in the graphite plane [104,110,111]. A wide profile across the G- and D-bands appears at higher disorder levels corresponding to the graphite phonon density of states (PDOS-like background) [112]. The presence of this profile indicates the appearance of amorphization in the graphite layers [111]. However, separation of the PDOS-like background from other bands is problematic due to its rather broad profile. In addition, a large G-band is always observed due to the presence of pristine graphite layers below the nitrogen ion sputtered surface.

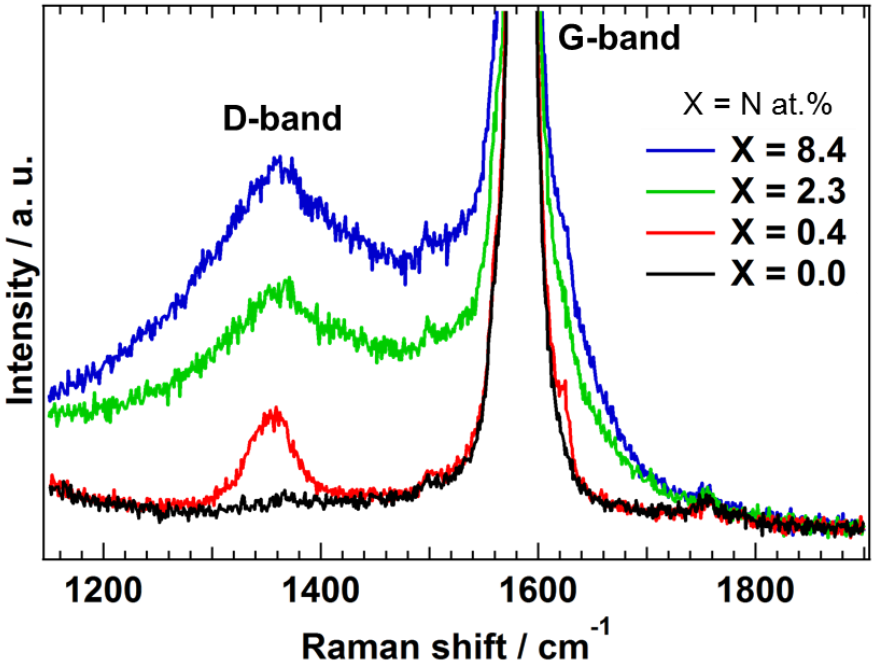

Fig. 4.8. Raman spectra of each N-HOPG and clean HOPG.

The sharp D-band in N-HOPG below X = 0.4 corresponds to the formation of defects with or without the doped nitrogen. The absence of the PDOS-like background indicates almost no disturbance of the surface graphite layers by nitrogen ion sputtering. The broad D-band and PDOS-like background were found to increase with the nitrogen content (X = 2.3, and 8.4), indicating the increase in amorphization of graphite due to the collapse of nitrogen ions partially penetrating into several graphite layers. These results suggest that the controlled nitrogen doping of HOPG with minimal disturbance to the graphite layer can only be realized under the appropriate conditions, such as < 8 $\times$ 10^{13} ions cm^{-2} (N-HOPG with X =0.4) nitrogen ion sputtering. The Raman scattering results are not necessarily consistent with the XAS results, which demonstrated the high orientation of the doped nitrogen components even at N-HOPG with X = 2.3 in Figs. 4.5 and 4.6. While N 1*s* XAS only probes the doped nitrogen, the Raman spectroscopy evaluates not only carbon sites close to the doped nitrogen but also the amorphous carbon and the bulk graphite. From the high polarization dependence of graphitic N and pyridinic N in N 1*s* XAS, these nitrogen species could be preferably doped into a flat graphite surface region rather than an amorphous carbon region, while the absence of polarization dependence of cyanide N can also exist in the amorphous

carbon region.

From the XAS, XPS, and Raman spectroscopy results, the HOPG doping mechanism of nitrogen ions can be summarized as follows; nitrogen atoms are preferably doped in the form of graphitic N and valley N in N-HOPG with X = 0.4. In N-HOPG with X = 2.3, the defective and amorphous regions increase in size. However, pyridinic N and graphitic N are likely to be doped into the flat in-plane graphite region, rather than into the amorphous region. As the amount of doped nitrogen increases in N-HOPG with X = 8.4, the majority of flat graphite layers convert into defective and amorphous regions, resulting in lower orientation of the doped nitrogen.

4.3.4 Possible nitrogen contribution to ORR of N-HOPG

The ORR activity measurements of N-HOPG were performed to discuss the possible contribution of nitrogen to ORR as shown in Fig. 4.9. The N-HOPG with X = 0.4 and 2.3 at low nitrogen concentrations exhibited higher ORR activity than the clean HOPG (E_{O2} = 0.05 V at −2 μA cm^{-2}). In particular, the N-HOPG with X = 0.4 at the lowest nitrogen doping level shows the highest ORR activity (E_{O_2} = 0.36 V at −2 μA cm^{-2}) among the three N-HOPGs. As the total amount of nitrogen increases, the ORR activity of N-HOPG with X = 8.4 decreases, and eventually drops below the activity of clean HOPG, likely due to the presence of amorphous regions that significantly reduce electron conductivity. Therefore, it is difficult to determine the relationship with ORR activity and each nitrogen component as shown in Fig. 4.9 (b). The possible nitrogen components to ORR are considered to be valley N and pyridinic N. This is because the relative ratio of valley N is high in N-HOPG with X = 0.4 which shows the highest ORR activity and pyridinic N is one of the probable ORR active nitrogen species in the previous reports [40,113].

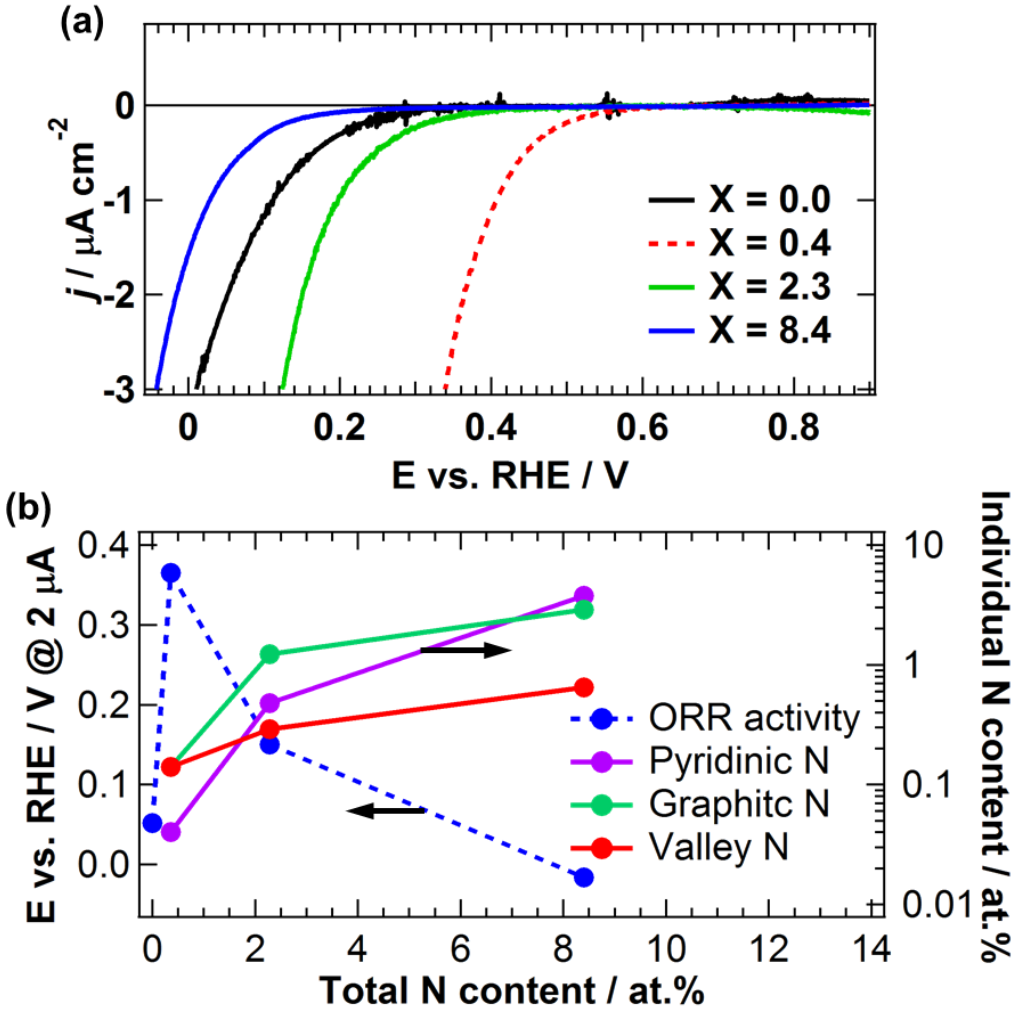

Fig. 4.9. (a) LSV voltammogram for ORR of each N-HOPG (X = 0.4, 2.3, and 8.4) and clean HOPG. (b) Electrochemical activities (the voltage at which a reduction current density of -10 μA cm^{-2}) and individual nitrogen content in N 1s XPS as a function of total nitrogen content.

With regards to the active site created by doped nitrogen on N-HOPG, it has been theoretically predicted that carbon atoms adjacent to both (1) valley N atoms at the zigzag edge [42–44] and (2) pyridinic N [114] atoms could be active sites for ORR, as they form occupied localized electronic states near the Fermi level at the carbon atoms. In addition, STS measurements and DFT calculations demonstrated that the carbon atoms in the vicinity of pyridinic N with a mono-vacancy create occupied localized electronic states near the Fermi level [49]. Therefore, these carbon atoms would be the

candidates for ORR active sites. In the possibility of the valley N, highly oriented valley N sites are selectively formed and the ORR activity is high under the low nitrogen doping conditions (X = 0.4). If it is assumed that valley N at vacancy sites can also modify the local electronic structure of neighboring carbon atoms in the same manner as at zigzag edges, N-HOPG with X = 0.4 can be considered to have such a theoretically-predicted ORR active site. This prediction supports the graphite based catalyst containing valley N sites shows high ORR activity. However, despite the three-fold increase in the absolute number of valley N sites, at higher nitrogen doping (N-HOPG with X = 2.3), the ORR activity decreases likely due to the significant change in electron conductivity. In contrast, the relative ratio of pyridinic N gradually increases with the total nitrogen content, while the ORR activity gradually decreases. As mentioned above, the amorphous carbon may affect the ORR activity at higher nitrogen doping conditions (N-HOPG with X = 2.3 or 8.4). Although the active sites for ORR in N-HOPG cannot be firmly concluded, it was important to prepare and examine the well-defined nitrogen structures.

Comparison of the graphite model with current catalysts synthesized from organic precursors is also of interest. In a standard synthetic protocol, such catalysts are subjected to heat treatment that converts an amorphous carbon structure into an ordered graphite structure. Above a critical temperature, their ORR activity dramatically improves, mainly due to a sharp increase in electron conductivity [115]. In addition, at higher pyrolysis temperatures, the ordered carbon structure excludes impurities such as nitrogen atoms, and the remaining nitrogen species dominate as in-plane graphitic N and/or pyridinic N [113,116]. In the study reported herein, N-HOPG with X = 0.4 under the lowest nitrogen doping conditions corresponds to this high temperature pyrolysis region of the current catalysts in terms of catalytic activity and electron conductivity. This N-HOPG preferably contains graphitic N and valley N due to the optimized low energy nitrogen ion sputtering and annealing conditions. The higher nitrogen doping thus produces an amorphous carbon structure on the surface of HOPG containing a variety of nitrogen species, comparable to that observed below the critical pyrolysis temperature of the current catalysts with high nitrogen concentrations. Thus, detailed studies on the properties of model N-HOPG catalysts under similar electron conductivity conditions (*e.g.*, similar density of amorphous carbon) will provide further

insight into the ORR active site. The highly oriented N-HOPG is expected to be a reference system for studying the orientation of nitrogen sites and the role of oxygen adsorption as the first step in the ORR [117] in carbon-based fuel cell cathode catalysts. The adsorbed O_2 configuration is expected to be critical with regards to the recently debated 2-electron or 4-electron mechanisms for the ORR [118,119].

4.4 Conclusions

The characteristics of nitrogen doped highly ordered pyrolytic graphite (N-HOPG) using the low energy nitrogen ion sputtering (200 eV) were investigated by X-ray photoelectron spectroscopy (XPS), X-ray absorption spectroscopy (XAS), and Raman spectroscopy in combination with electrochemical measurements. Under low nitrogen doping conditions (N-HOPG with X = 0.4), the doped nitrogen is well oriented in the graphite basal plane, substituting the graphite lattice to form the graphitic N and pyridinic N sites. On increasing the nitrogen dose the in-plane orientation of the incorporated nitrogen species become less remarkable, and under high nitrogen doping conditions (N-HOPG with X = 8.4) defective and non-planar structures become dominant. Raman spectra exhibit a similar trend. However, in the case of N-HOPG with X = 2.3, XAS revealed a highly oriented doped nitrogen character, while an amorphous-like signature was observed in the Raman spectrum. It is therefore thought that nitrogen atoms in N-HOPG with X = 2.3 are likely to be doped into the flat graphite region rather than into the amorphous region. Moreover, an additional peak was observed at higher binding energy of 401.9 eV than 400.9 eV for graphitic N in the basal plane in N 1*s* XPS. According to the previous theoretical and experimental reports, it seems to be most plausible to assign the peak to valley N (graphitic N in the zigzag edge and/or vacancy sites). The graphitic N and valley N were preferably formed when the amount of doped nitrogen was small (N-HOPG with X = 0.4), while the graphitic N was more abundant at higher nitrogen doping levels (N-HOPG with X = 2.3). The ORR activity measurements of N-HOPG were performed and the N-HOPG with X = 0.4 at the lowest nitrogen doping level showed the highest ORR activity among the three N-HOPG. Applying this preparation and characterization methods of model N-HOPG catalysts is a novel and promising way to reveal the nitrogen doped carbon-based catalysts.

Chapter 5

Lewis basicity of nitrogen-doped graphite observed by CO_2 adsorption

5.1 Introduction

Nitrogen doping to carbon-based catalysts modifies the electronic structure of carbon substrate. Recent STS measurements have revealed the localized electronic structures on the nitrogen doped graphite surface as shown in Fig. 1.4 [49]. The modified electronic structures near the Fermi level would hybridize with that of O_2 molecules, which is important to enhance the catalytic activity. As for the first step of ORR, O_2 is adsorbed on the surface and reduction reaction proceeds with electron donation from the catalytic active sites. Thus, the electron-donating property (Lewis basicity) would be important to reduce the O_2 molecules. The Lewis basicity of catalysts is usually investigated by the CO_2 adsorption. Since CO_2 molecule is a weak Lewis acid with an electropositive carbon atom [53,54], the carbon atom can detect the nitrogen-induced Lewis basic sites in the carbon-based catalysts; this detection is classified as Lewis acid/base reaction. Experimentally, Moroboshi *et al.* reported that the amount of the adsorbed CO_2 is proportional to the ORR activity of the nitrogen doped graphene [120]. Therefore, the detailed experimental information regarding the chemical state and geometry of adsorbed CO_2 on nitrogen-doped carbon-based catalysts is required to clarify the degree of Lewis basicity, which is useful to fine-tune the Lewis basicity toward ORR. The synthesized N-HOPG in the chapter 4 is suitable for revealing the Lewis basicity of carbon-based catalysts since it possesses the well-defined and electrochemical-active carbon structure with the doped nitrogen.

In this study, the Lewis basicity and the adsorption property of CO_2 of N-HOPG, synthesized by low-energy nitrogen-ion sputtering, were investigated using XPS,

angle-dependent XAS, and infrared reflection absorption spectroscopy (IRRAS). Using the highly graphitized model N-HOPG with selective nitrogen doping, the possible contribution of nitrogen components to the formation of Lewis base sites on N-HOPG will be discussed.

5.2 Experimental methods

The detailed preparation of N-HOPG was described in Chapter 2.1.2. The amounts of dosed nitrogen ions were calculated to be 8×10^{13} ions cm^{-2}, which is the same condition to synthesis N-HOPG with X = 0.4 as discussed in the chapter 4.

XPS measurements were performed at BL27SU in SPring-8 using a photoelectron analyzer (PHOIBOS 150, SPECS GmbH). The typical base pressures for the measurement and preparation chambers were 4×10^{-8} and 3×10^{-7} Pa, respectively. The incident photon energy and the photoemission angle were 850 eV and 45°, repectively. The total energy resolution of the XPS was 230 meV. Samples were scanned with the incident photon beam at a rate of 0.4 μm/s to reduce the radiation damage to the adsorbed molecules. The binding energies were calibrated using the Au 4*f* 7/2 (binding energy = 84.0 eV) peak of an evaporated gold as a reference. The N 1*s* spectra were fitted with the Voigt function (1.2 and 0.25 eV Gaussian and Lorentzian widths, respectively) as well as background subtraction using the Shirley method. N 1*s* and O 1*s* XAS spectra were measured by the PEY mode at BL27SU. The XAS spectra were collected by setting the angle θ between the incident X-ray beam axis and the surface normal to 0°, 45°, and 70°. The energy resolution of XAS had a lower limit below 100 meV.

The N-HOPG was annealed at 1000 K for 30 min in the preparation chamber to remove the initially adsorbed gas before the XPS and XAS measurements were performed. The sample was exposed to CO_2 at 300 K for 2500 s at 5.3×10^{-4} Pa, corresponding to 10000 L in volume.

IRRAS measurements were performed in grazing-angle reflection geometry both before and after CO_2 adsorption at 300 K to investigate the configuration of the adsorbed CO_2. In order to estimate the amount of the adsorbed CO_2 temperature-programmed desorption (TPD) was performed between 300 K and 700 K, with CO_2 adsorption at 300 K. Both the IRRAS and TPD experiments were performed

in the same UHV (3×10^{-8} Pa) chamber.

5.3 Results and discussion

5.3.1 Characterization of N-HOPG before CO_2 adsorption

The N-HOPG was synthesized in the same procedure described in the chapter 4.2. Figure 5.1 (a) shows the C 1*s* XPS spectra of HOPG and N-HOPG. The spectral intensities are normalized to the peak areas. The nitrogen ion sputtering causes the C 1*s* peak to broaden and introduces the C=N bond peak at 285.6 eV [121]. Figure 5.1 (b) shows the N 1*s* XPS spectrum of N-HOPG. The nitrogen content (ratio of N/C) is calculated from the XPS results to be 0.42 at.%. The spectrum is fitted with four Voigt functions corresponding to each nitrogen component, denoted as pyridinic N (NP1: 398.0 eV), cyanide N (NP2: 399.9 eV), graphitic N (NP3: 401.0 eV), and valley N (NP4: 401.9 eV) [122]. The terminology of each nitrogen component used hereafter is represented in Fig. 5.2. The detailed nitrogen configurations and peak assignment of each components has been already discussed in the chapter 4.3.1. The pyrrolic N can be excluded from NP2 since no XAS peak corresponding to the pyrrolic N was observed in chapter 4.3.2. The estimated amount of each nitrogen component from the fitting results is similar to that of N-HOPG with X = 0.4 in the chapter 4.3.1; graphitic N is the most prevalent, followed by valley N and pyridinic N.

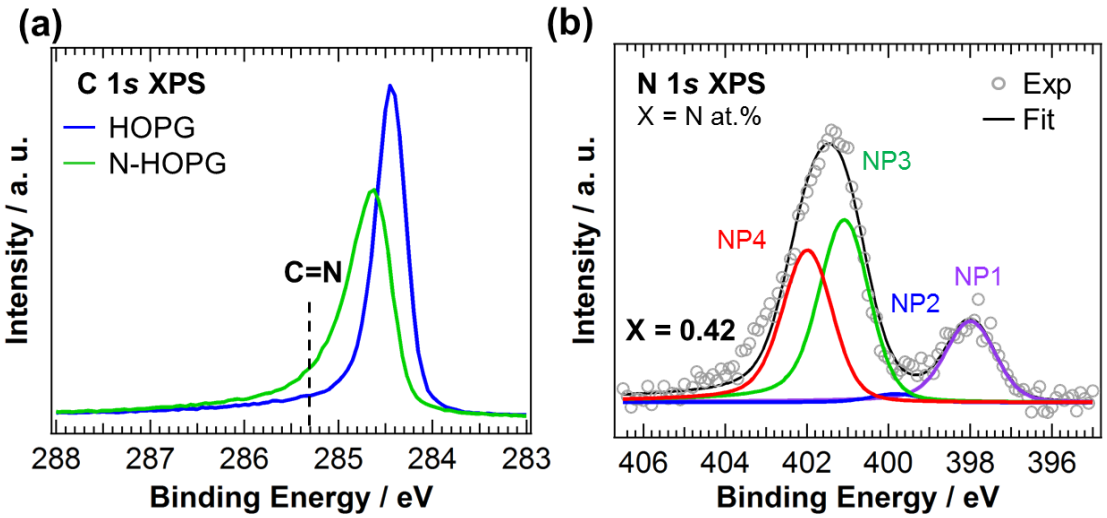

Fig. 5.1. XPS spectra of HOPG and N-HOPG before CO_2 adsorption: (a) C 1*s* XPS and (b) N 1*s* XPS. Gray open circle and black line represent raw data and fitting results. Purple, blue, green, and red solid lines are pyridinic N (NP1), cyanide N (NP2), graphitic N (NP3), and valley N (NP4) components, respectively.

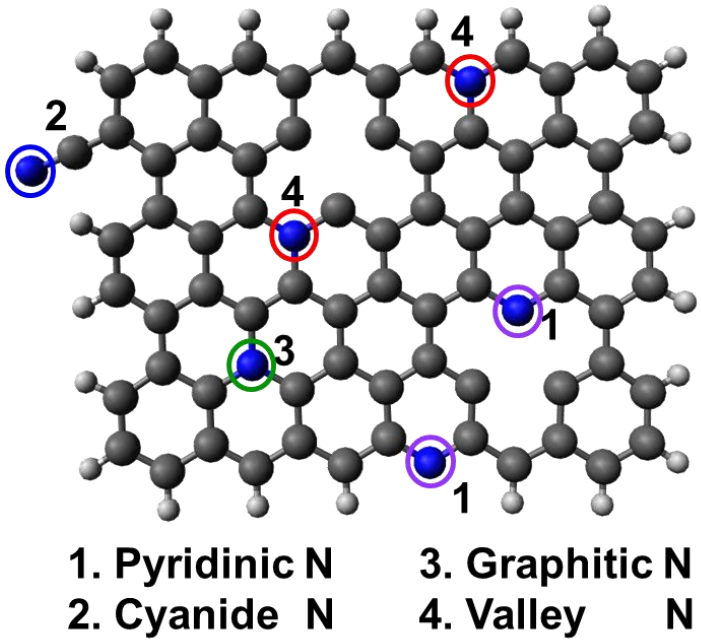

Fig. 5.2. A schematic image of each nitrogen component observed in N-HOPG (N/C = 0.42 at.%). Hydrogen, carbon, and nitrogen atoms correspond to white, black, and blue balls, respectively.

5.3.2 CO_2-TPD measurements of N-HOPG

Figure 5.3 (a) shows the TPD spectra of mass 44 (CO_2) on N-HOPG. The exposure amount of CO_2 is changed from 0 L to 10000 L at 300 K. The spectra are raw data without normalization. A similar CO_2 desorption peak is observed between 320 K and 400 K with the different CO_2 exposure amount, indicating the CO_2 desorption on N-HOPG is a first order. The first order desorption is an evidence of associative adsorption of CO_2 on N-HOPG since a second order reaction ($CO + O_{ads} \rightarrow CO_{2,ads} \rightarrow CO_{2,des}$) should be expected if the dissociative adsorption occurs. The reproducibility of the TPD measurements was confirmed by 5000 L CO_2 exposure using the same N-HOPG, indicating the CO_2 adsorption sites are not poisoned with CO_2 and restored after annealing to 600 K. Furthermore, the peak top of CO_2 desorption is almost constant at approximately 345 K with the different CO_2 exposure amount although it should be noted to underestimate the absolute temperature due to the insufficient temperature calibration. The activation energy for CO_2 desorption can be estimated simply through Redhead equation (5.1) [123] using the observed peak top temperature T_{peak} (K) and temperature raising rate β (K s^{-1})

$$E_a = RT_{peak}\left(ln\left(\frac{vT_{peak}}{\beta}\right) - 3.64\right) \qquad \cdots (5.1)$$

where E_a is an activation energy of desorption (J mol^{-1}), R is a gas constant (J K^{-1} mol^{-1}), and v is a pre-exponential factor (s^{-1}). The activation energy for CO_2 desorption E_a is obtained as 92 kJ mol^{-1} where β = 0.6 K s^{-1}, T_{peak} = 435 K, and $v = 1.0 \times 10^{13}$ s^{-1}. The CO_2 adsorption is proved to be a chemisorption process since the adsorption energy exceeds 40 kJ mol^{-1}. In contrast, only physisorbed CO_2 was reported on HOPG, where it desorbed at 83 K with the desorption energy of 20 kJ mol^{-1} [124]. According to these results, nitrogen doping to HOPG induces a new adsorption sites for CO_2 to chemisorb at 300 K.

Figure 5.3 (b) shows the integrated area intensity of the mass 44 (CO_2) peak as a function of CO_2 exposure amount obtained by the TPD measurements. The saturation amount of adsorbed CO_2 on N-HOPG is near 10000 L: this amount was used for the XPS and XAS measurements. The fact that the saturation coverage was not obtained under 10000 L is the reflection that the probability of CO_2 adsorption at 300 K is significantly low. However, it is difficult to reveal the precise mechanism only in this study.

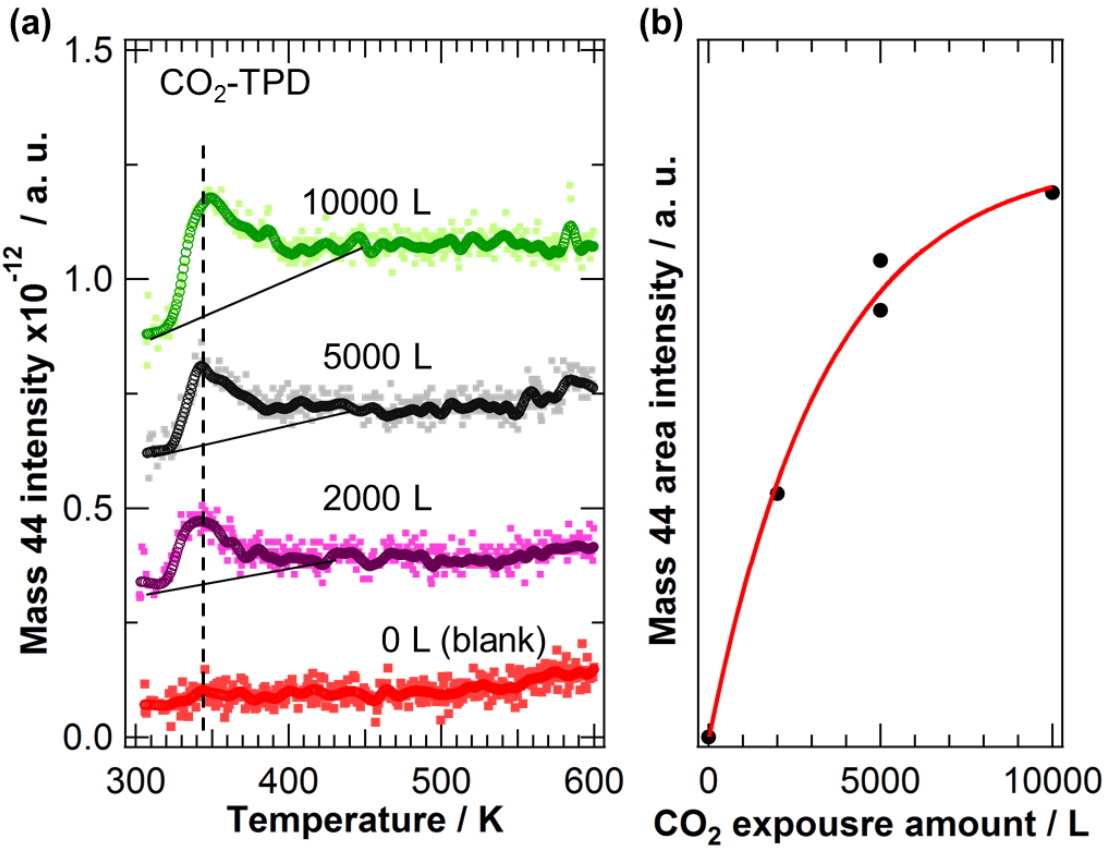

Fig. 5.3. (a) TPD spectra of N-HOPG with the different CO_2 exposure amount. (b) The area intensity of the mass 44 (CO_2) peak as a function of the CO_2 exposure amount.

5.3.3 Chemical states of adsorbed CO_2 on N-HOPG

Figure 5.4 shows O 1*s* XPS spectra of (a) HOPG and (b) N-HOPG before and after CO_2 adsorption. A very small amount of oxygen species (O/C = 0.040 at.%) exists in N-HOPG before CO_2 adsorption, as shown in Fig. 5.4 (b), which are not fully removed by annealing at 1000 K for 30 min. The difference spectrum in Fig. 5.4 (b) shows an O 1*s* peak centered at approximately 533 eV caused by CO_2 adsorption on N-HOPG. The difference in the oxygen content (ratio of O/C) is 0.023 at.% based on the XPS fitting results. Since CO_2 molecule is composed of one carbon atom and two oxygen atoms, the total number of CO_2 is 0.012 at. %. The quantitative discussion about interaction between CO_2 molecules and the adsorption sites will be shown in the chapter 5.3.5. However, the difference spectrum in Fig 5.4 (a) of HOPG at 300K shows no peak related to adsorbed CO_2. Table 5.1 summarizes the O 1*s* binding energies for physisorbed and chemisorbed CO_2 on various substrates [125–131]; for physisorbed CO_2, the binding energy is distributed from 534.0 eV to 535.8 eV, while for chemisorbed CO_2 it ranges from 530.6 eV to 533 eV. The observed binding energy at 533 eV on N-HOPG is below that of physisorbed CO_2 but within the range of chemisorption. The interaction strength of CO_2 directly estimates the degree of Lewis basicity of the N-HOPG substrate. To determine the origin of this binding energy, the electronic structure of CO_2 as presented by a Walsh diagram in Fig. 5.5 is considered [132]. The lowest unoccupied molecular orbital (LUMO) of $2\pi_u$ is degenerated in the linear configuration while it splits into $2b_1$ (perpendicular to the CO_2 plane) and $6a_1$ (parallel to the CO_2 plane) orbitals in the bent configuration. In particular, the energy position of $6a_1$ orbital sharply decreases upon bending. In the bent configuration, this low-energy $6a_1$ orbital is occupied by electrons charge-transferred from the substrate and stabilizes the adsorbed CO_2 molecules on N-HOPG. Thus, the charge transfer from the substrate to the $6a_1$ orbital in the bent configuration weakens the strength of CO bonds, causing the O 1*s* core level shift of CO_2 to the lower binding energy at approximately 533 eV. This result also provides evidence for the presence of Lewis base sites in the graphite system caused by the doped nitrogen.

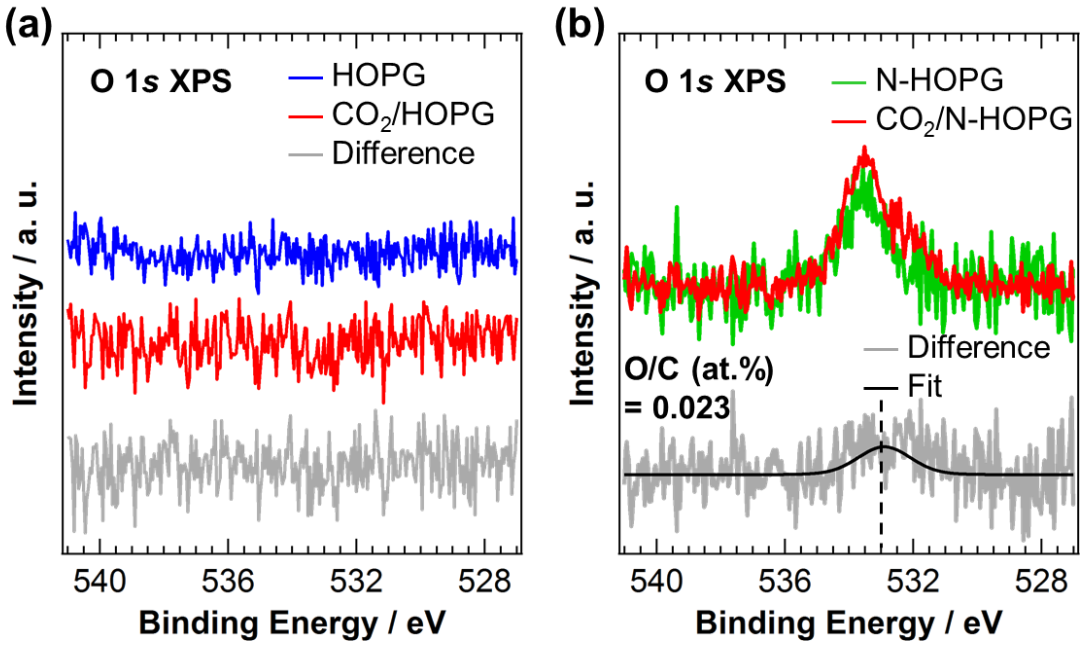

Fig. 5.4. O 1*s* XPS spectra of (a) HOPG and (b) N-HOPG before and after CO_2 adsorption. Gray and black lines correspond to difference spectra through CO_2 adsorption and fitting result, respectively.

Table 5.1. O 1*s* binding energies for physisorbed and chemisorbed CO_2 on various substrates

Substrate	O 1*s* Binding Energy / eV		Ref.
	Physisorption (CO_2)	Chemisorption ($CO_2^{\delta-}$)	
Ni(110)	534.7	531.1	[125]
Ni(110)	534	530.6	[126]
Fe(poly)	535	531	[125]
Cr_2O_3(0001)	-	532.5	[127,128]
K doped Rh(111)	534.7	532.8	[129]
K doped Mo_2C	535.8	533	[130]
Graphene/SiC(0001)	534.8	-	[131]
N doped HOPG	-	533	This work

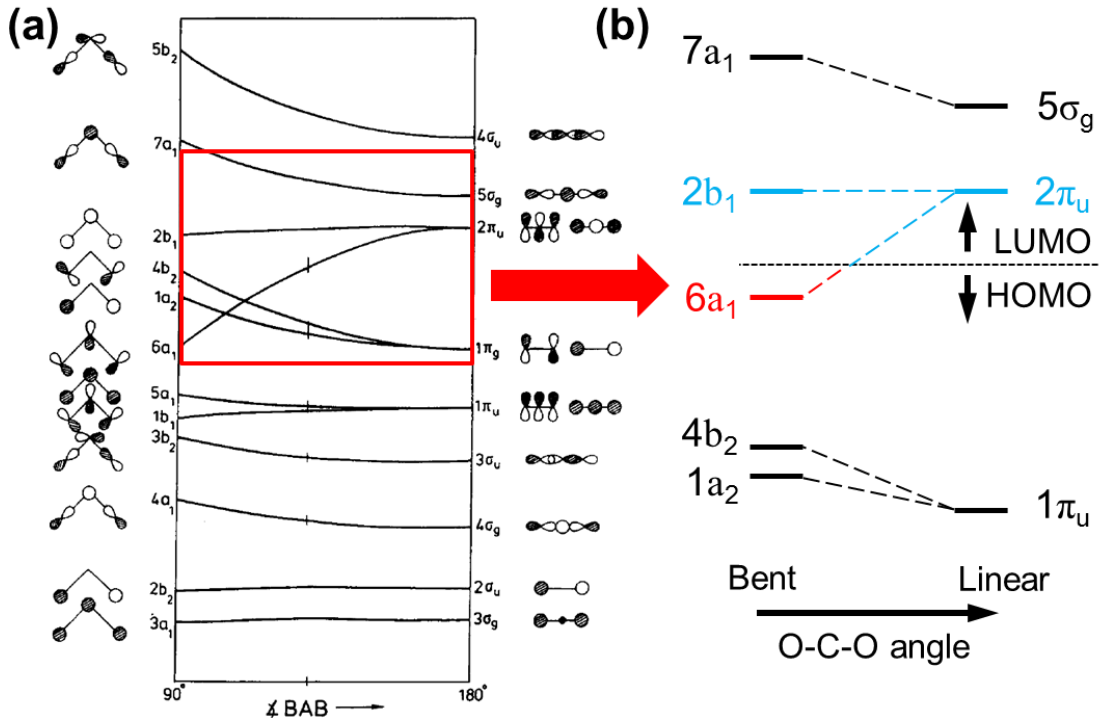

Fig. 5.5. (a) A schematic image of the Walsh diagram of CO_2 orbital energies in linear and bent geometries [132]. (b) The enlarged Walsh diagram near HOMO (red) and LUMO (blue) levels of CO_2.

5.3.4 Configuration of adsorbed CO_2 on N-HOPG

In order to reveal the orientation of the adsorbed CO_2 on N-HOPG, angle-dependent XAS was performed. Figure 5.6 (a) shows the O 1*s* XAS spectra of N-HOPG after CO_2 adsorption for different X-ray incident angles θ, where the background XAS profile obtained before CO_2 adsorption is subtracted. The σ* (540 eV) and π* (532 eV) peaks are enhanced at surface normal (0°) and grazing (70°) incidence, respectively. Since the similar angle dependence is observed in the carbon π* state of HOPG (C 1*s* XAS) [107], this polarization dependence of O 1*s* XAS indicates that the CO_2 molecules are lying flat on the N-HOPG surface. Although the energy position of the $6a_1$ orbital sharply decreases upon bending, the energy position of the $2b_1$ orbital remains nearly constant relative to that of the $2\pi_u$ orbital, as shown in Fig. 5.5. Therefore, the observed π* orbital would be derived from the $2b_1$ orbital (perpendicular to the CO_2 plane) caused by the splitting of CO_2 LUMO orbitals. The observed π* peak is ~2.8 eV lower than the π* peak ($2\pi_u$ orbital) for the gas-phase linear CO_2 at 534.8 eV [133], mainly because of the

observed chemical shift of the O 1*s* core level in XPS (~533 eV) as shown in Fig 5.6 (b), as discussed in the chapter 5.3.3.

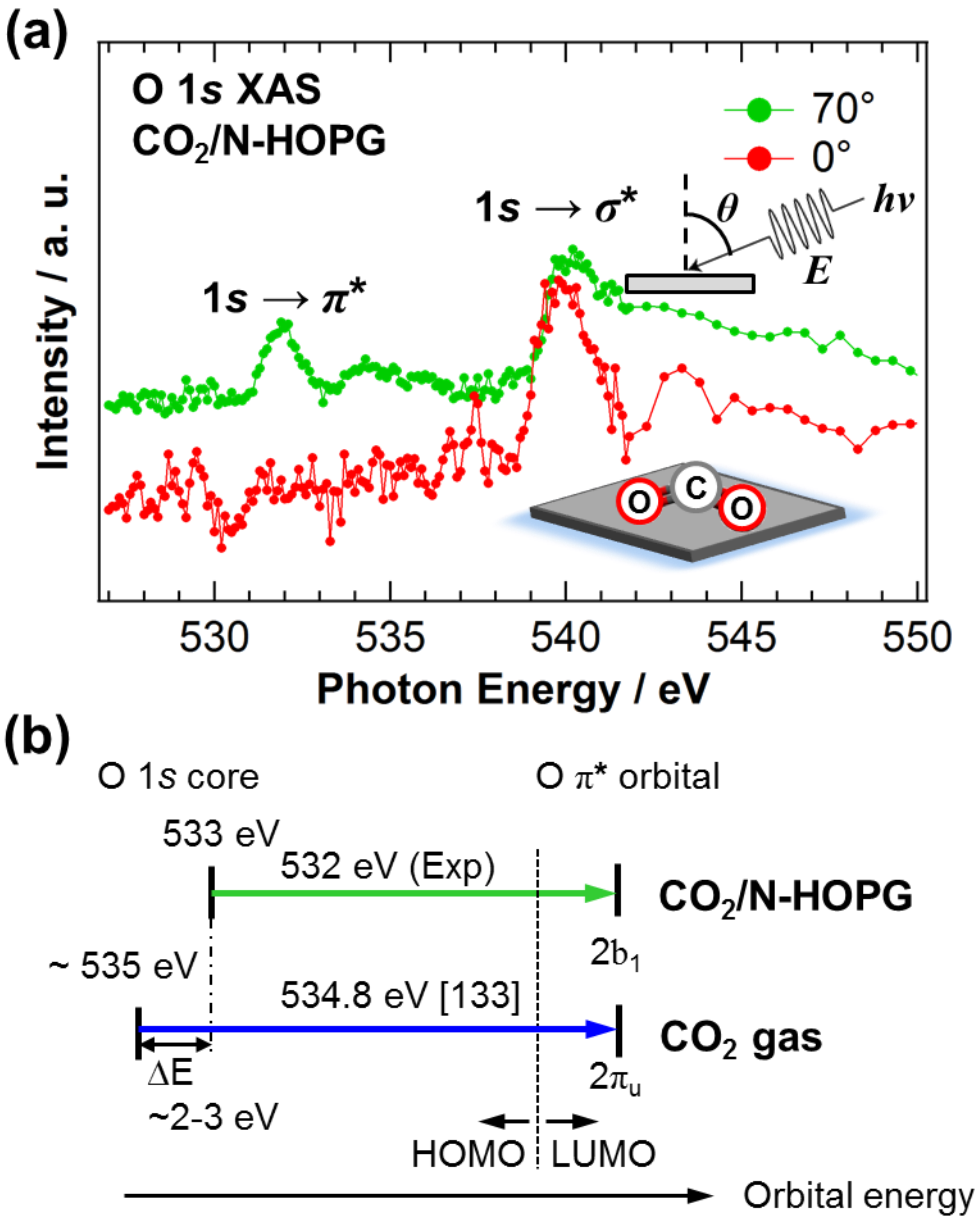

Fig. 5.6. (a) O 1s XAS spectra of N-HOPG after CO_2 adsorption. Red and green lines correspond to the spectra obtained with X-ray incident angles θ = 0° and 70°. (b) A schematic diagram of O 1*s* X-ray absorption process of CO_2/N-HOPG (this work) and CO_2 gas [133].

The IRRAS spectrum in Fig. 5.7 also supports the above CO_2 configuration; considering the selection rule of IRRAS, the absence of peaks at approximately 1200-1300 cm^{-1} and 1600 cm^{-1}, which are expected for the symmetric and asymmetric OCO-stretching modes of the bent $CO_2^{\delta-}$ carboxylate with its molecular plane perpendicular to the surface [128], suggests the CO_2 to be lying flat on the surface. Both the O 1*s* XAS spectra and the IRRAS spectrum of the N-HOPG support this configuration of the adsorbed CO_2 lying flat on the N-HOPG surface.

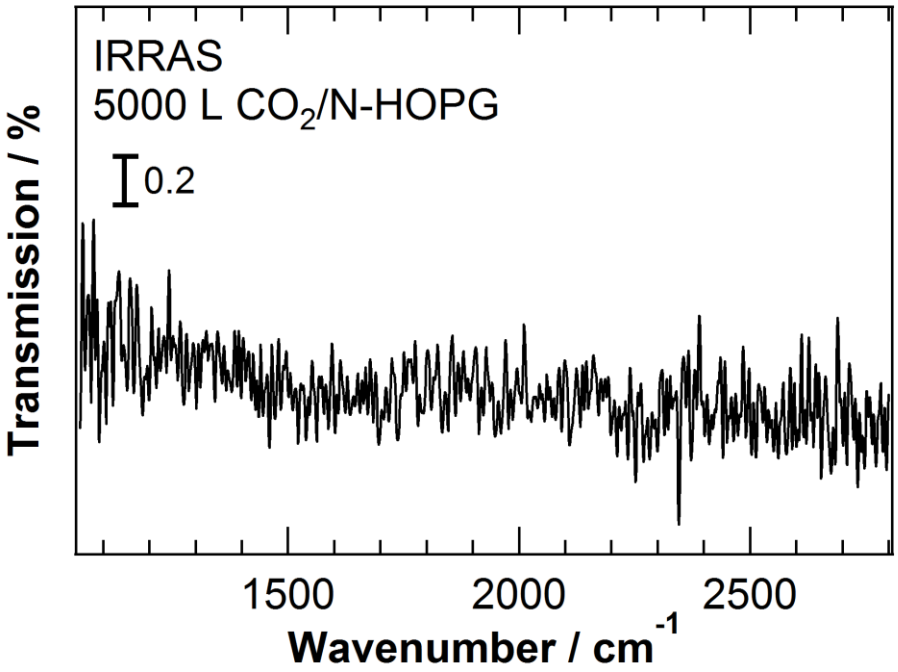

Fig. 5.7. IRRAS spectrum of N-HOPG with 5000 L CO_2 exposure.

5.3.5 Possible CO_2 adsorption sites on N-HOPG

To discuss the possible CO_2 adsorption sites derived from the doped nitrogen, angle-dependent N 1*s* XAS was performed before and after CO_2 adsorption. Figure 5.8 (a) shows the N 1*s* XAS spectra in the π* region of the N-HOPG before and after CO_2 adsorption for different X-ray incident angles of 0°, 45°, and 70°. The spectra before CO_2 adsorption are normalized according to the intensity at 430 eV. In contrast, the spectra after CO_2 adsorption are normalized according to the integrated peak area corresponding to each X-ray incident angle before CO_2 adsorption. Three sharp peaks in the π* region can be assigned to pyridinic N (A), cyanide N (B), and graphitic N (graphitic N and valley N) (C) [51]. The intensities of the pyridinic and graphitic N change with the X-ray incident angles, indicating that these components are incorporated into the planar graphite lattice via substitution [105] as discussed in the chapter 4.3.2. Since the adsorbed CO_2 also shows a highly oriented (lying flat) configuration, CO_2 adsorption sites should be introduced in the vicinity of the highly oriented (A) pyridinic and (B) graphitic N (graphitic N and valley N).

The difference spectra were taking by subtracting the spectra before CO_2 adsorption from the spectra after CO_2 adsorption (Fig. 5.8 (b)). The change ratios were taking by dividing the spectra in Fig. 5.8 (b) by the experimental spectra after CO_2 adsorption (Fig. 5.8 (c)) to remove the intensity difference of each nitrogen component. Since the positive and negative values in Fig. 5.8 (b), (c) mean the increased and decreased peaks after CO_2 adsorption, respectively, the change ratios would show the negative values if the CO_2 bonds directly to the nitrogen sites and causes the change of the electronic structure of nitrogen. For example, Tao *et al.* reported that the large positive chemical shift (~+1.9 eV) is observed in pyridine on Si bonded via lone pair compared to physisorbed pyridine on Si [134]. However, the change ratios around the peak A, B, C are quite low below ~10%. As already investigated in chapter 5.3.1 and 5.3.3, the number of the adsorbed CO_2 molecules and the ratios of the CO_2 molecules to each nitrogen component are summarized in Table 5.2, indicating that the maximum change ratios are expected to be 14%, 142%, 7%, and 8% for peak A, B, C, and C, respectively. From these results, it is discussed whether CO_2 directly bonds to the nitrogen sites or not as follow. Firstly, the cyanide N can be excluded since it shows the smaller change ratio (~10%) than the expected one (142%). In addition, the graphitic N and valley N

can be excluded due to the positive values of change ratio. The pyridinic N would be also excluded because the change ratio of pyridinic N (~5-9 %) is below the expected one (14%) although it should be noted that the expected one (14%) is similar to that of the S/N level. Therefore, CO_2 adsorption sites would be not nitrogen sites but carbon sites in the vicinity of nitrogen.

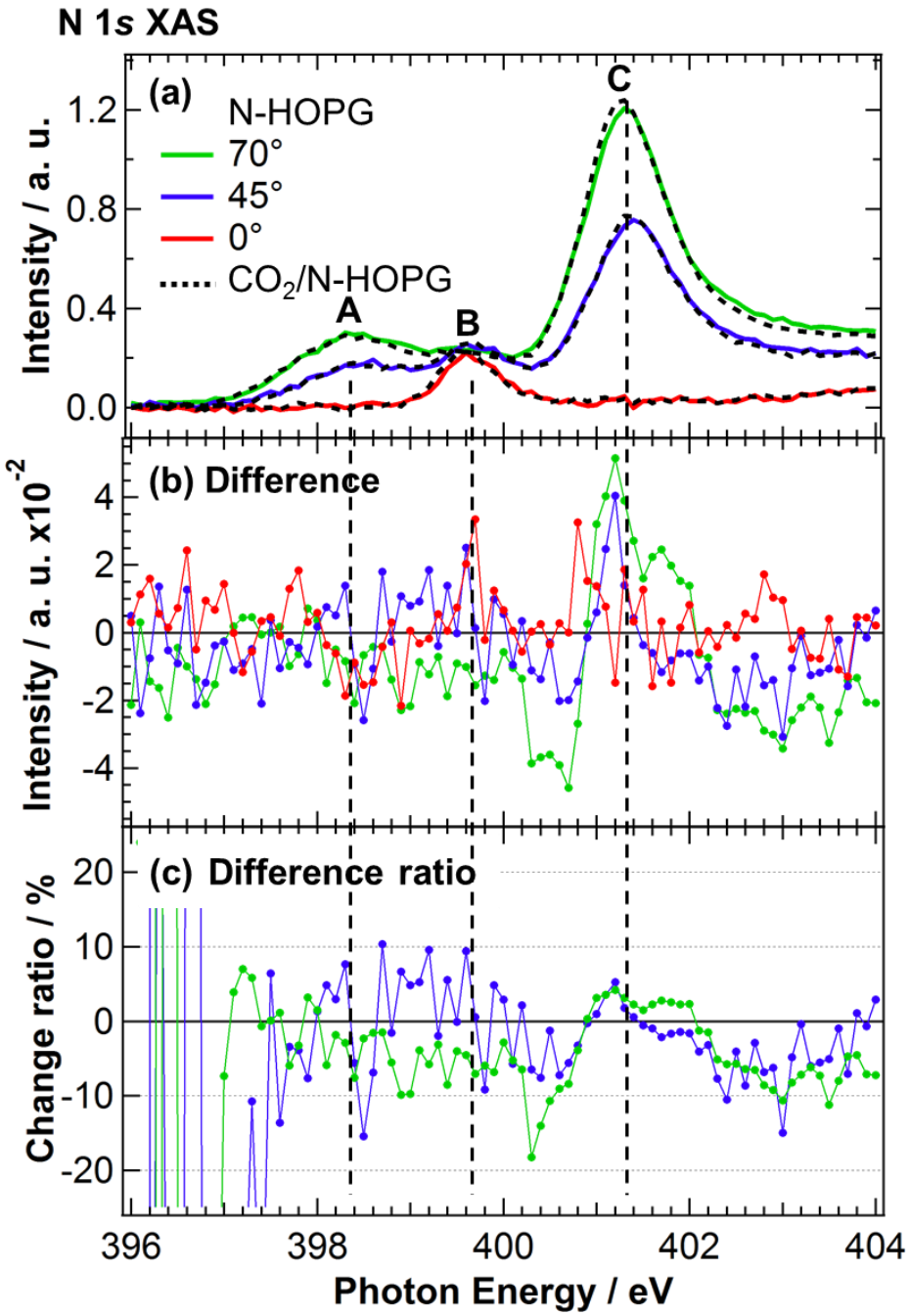

Fig. 5.8. N 1*s* XAS spectra of N-HOPG before and after CO_2 adsorption: (a) experimental spectra, (b) difference spectra calculated by subtracting (N-HOPG) from (CO_2/N-HOPG), (c) change ratios calculated by dividing (b) by the spectra after CO_2 adsorption. Red, blue, and green lines correspond to the spectra obtained with X-ray incident angles θ = 0°, 45°, and 70°. The dotted black line represents the spectra of each X-ray incident angle after CO_2 adsorption.

Table 5.2. The number of the adsorbed CO_2 molecules ($CO_{2,\,ads}$) and the ratios of the CO_2 molecules to each nitrogen component ($Ratio_x$, X = pyridinic, cyanide, graphitic and valley N)

	$CO_{2,\,ads}$ / at.%	$CO_{2,\,ads}$ / $Ratio_x$ / %			
		Pyridinic N	Cyanide N	Graphitic N	Valley N
N-HOPG	0.012	14	142	7	8

Based on the Lewis acid/base interaction picture, the possible CO_2 adsorption process via a localized electronic structure of the graphite surface modified by the doped nitrogen [49,81,83,135] are discussed as follow: carbon sites in the vicinity of (1) pyridinic N, (2) valley N, (3) graphitic N, and (4) defect sites.

(1) Carbon sites in the vicinity of pyridinic N

Recently, Kondo *et al.* reported the localized electronic structure at ~–370 meV below the Fermi level was observed in several carbon atoms near pyridinic N with a monovacancy [49]. The carbon sites possessing this electronic structure would act as Lewis base sites and interact with CO_2 through charge transfer from the localized electronic structure. However, CO_2 would not be adsorbed on carbon atoms next to pyridinic N since the expected change ratio of pyridinic N is not observed in Fig. 5.8 (c). For example, the large positive chemical shift (~+1.5 eV) was observed in the pyridonic N which is pyridinic N with an electron-with drawing hydroxyl group at the ortho carbon atom [68]. Therefore, the several carbon atoms near the pyridinic N are probable for the active sites for CO_2 adsorption.

(2) Carbon sites in the vicinity of valley N

The observed valley N in XPS results is also expected to modify the electronic structure of the surrounding carbon atoms, and induce a localized density of states at ~–

200-400 meV below the Fermi level [83] , which may also provide CO_2 adsorption sites. The localized electronic structure was theoretically induced at two carbon atoms next to the valley N in the zigzag edge, which are probable for the active sites for CO_2 adsorption. However, since the local electronic structure of valley N has not been observed experimentally yet, further study by STM and STS measurements will be necessary to discuss the electronic structure of valley N. The possibility of nitrogen sites can be excluded due to the more positively charged valley N (401.9 eV) than the pyridinic N (398.0 eV) as shown in Fig. 5.1 (b).

(3) Carbon sites in the vicinity of graphitic N

Kondo *et al.* reported that the graphitic N in the basal plane also modifies the electronic structure of surrounding several carbon atoms [49]. However, they form a localized electronic structure at ~+500 meV above the Fermi level, which would act as Lewis acid sites. Therefore, CO_2 cannot be adsorbed near the graphitic N. The possibility of nitrogen sites can be also excluded due to the more positively charged graphitic N (401.0 eV) than the pyridinic N (398.0 eV) as shown in Fig. 5.1 (b).

(4) Carbon sites in the vicinity of defect sites

A localized electronic structure at ~+170 meV above the Fermi level was observed in the vicinity of a monovacancy by STS measurements [81], which is similar to that of graphitic N. Therefore, CO_2 cannot be adsorbed near the monovacancy sites.

From these considerations, the interaction sites with CO_2 in N-HOPG would be provided by the localized π states just below the Fermi level induced by the pyridinic N and/or valley N. CO_2 adsorption sites would be the surrounding several carbon atoms in the vicinity of the pyridinic N and/or valley N. It is important to note that the Lewis acid site derived from a monovacancy changes to the Lewis base site through the doping of pyridinic N, suggesting that nitrogen with defect engineering is crucial to modify the electronic structure of carbon-based catalyst.

The clear evidence of the charge transfer from the substrate and the new information on the molecular orientations of both CO_2 and nitrogen moieties on the graphite substrate provide great insight into the CO_2 adsorption and the Lewis basicity of nitrogen-doped graphite.

5.4 Conclusions

The adsorbed CO_2 at 300 K on N-HOPG was investigated by XPS, angle-dependent XAS, and IRRAS using N-HOPG model catalysts. The O 1*s* binding energy of the adsorbed CO_2 at 300 K, located at 533 eV, showed clear evidence of the Lewis basicity of N-HOPG caused by the nitrogen doped in the graphite system. The polarization dependence of the σ* and π* peaks in the O 1*s* XAS spectra, as well as the absence of expected IRRAS signals, clearly indicate that the adsorbed CO_2 lies flat on the graphite surface. The possible CO_2 adsorption sites with pyridinic N and valley N are discussed. Therefore, these results indicate that the Lewis base sites are induced by the incorporation of nitrogen in electrochemical active N-HOPG.

Chapter 6

Summary and future prospects

6.1 Summary

In this thesis, I have presented soft X-ray spectroscopy studies on the properties of O_2 and CO_2 adsorption in nitrogen-doped carbon-based catalysts to elucidate the role of the nitrogen toward the catalytic active sites. To reveal the element specific characteristics, I have measured the electronic structure using soft X-ray and used the powder catalyst and the nitrogen-doped graphite model catalyst (N-HOPG). Firstly, I have investigated the O_2 adsorption property of the nitrogen-containing metal-free powder catalyst and discussed the possible ORR mechanism. Secondly, I have synthesized the N-HOPG via low energy nitrogen ion implantation in a controlled manner and observed the development of the ORR activity. Then I have investigated the CO_2 adsorption property of N-HOPG to elucidate the Lewis basicity of the nitrogen-doped graphite surface.

In Chapter 1, I have outlined the present PEFC system and the current development of the cathode catalysts. It is required to develop the cathode catalysts without expensive and rare Pt in order to spread PEFC system widely. The carbon-based catalysts, which are modified by light elements and 3*d* transition metals, have attracted much attention due to the relatively high ORR activity; however, the lower ORR activity than Pt-based catalysts. Therefore, it is necessary for the carbon-based catalysts to elucidate the ORR active sites. To understand roles of each element, I have focused on the nitrogen components without transition metals and attempted to reveal the role of nitrogen.

In Chapter 3, I have investigated the O_2 adsorption property of nitrogen-containing metal-free CACs using *in situ* XPS, Raman spectroscopy, O_2 adsorption isotherm, and electrochemical measurements. The ORR activity, the selectivity of 2-electron ORR, and the amount of defect sites were increased in CACs compared to the nitrogen-free carbon materials. The chemisorbed O_2 was revealed by the adsorption isotherm and

mainly composed of C=O components (57%). In addition, the change of electronic structures of nitrogen before and after O_2 adsorption indicates a 3-fold coordinated graphitic N changes to a 2-fold coordinated pyridinic N. From these results, it is indicated that the graphitic N in the vicinity of defect sites enhances the O_2 adsorption with the C-N bond breaking. Furthermore, the adsorbed C=O components would form possible 2-electron ORR sites. Thus it is considered that nitrogen itself is contributed to not the ORR activity but the formation of ORR active sites.

In Chapter 4, I have investigated the characteristics of N-HOPG via low energy nitrogen ion sputtering at 200 eV using XPS, angle-dependent XAS, Raman spectroscopy in combination with electrochemical measurements. The doped graphitic and pyridinic N were substituted in the graphite basal plane under low nitrogen doping condition (N-HOPG with X = 0.4 at.%). The valley N (graphitic N in the zigzag edge and/or vacancy sites) was also observed preferably under the same condition. The orientation of the doped nitrogen is less remarkable and the amount of amorphous carbon structure increased on increasing the doped nitrogen content (N-HOPG with X = 8.4 at.%). Therefore, the flat N-HOPG with the controlled nitrogen species was synthesized under the appropriate conditions, such as $< 8 \times 10^{13}$ ions cm^{-2} (N-HOPG with X = 0.4 at.%) nitrogen ion sputtering at 200 eV. The highest ORR activity was observed in N-HOPGs (N-HOPG with X = 0.4 at.%) among the three N-HOPG (N-HOPG with X = 0.4, 2.3, and 8.4 at.%). Thus it was clarified that the doped nitrogen in the well-defined flat graphene lattice is contributed to improve the ORR activity.

In Chapter 5, I have investigated the CO_2 adsorption property and the electronic structure of N-HOPG (N-HOPG with X = 0.4 at.%) using XPS, angle-dependent XAS and IRRAS to elucidate the Lewis basicity of the nitrogen-doped graphite surface as an indicator of the ORR activity. The adsorbed CO_2 at 300 K was stabilized by a charge transfer from the substrate and showed approximately 2 eV lower O 1*s* binding energy, located at 533 eV, than that of the physisorbed CO_2. It was clear evidence of the Lewis basicity of N-HOPG caused by the nitrogen doped in the graphite. The high polarization dependence of O 1*s* XAS indicates the adsorbed CO_2 lies flat on the graphite surface. The N 1*s* XAS and XPS results indicate the possible CO_2 adsorption sites would be responsible for the carbon sites in the vicinity of the pyridinic and valley N, respectively.

Finally, I have summarized the role of nitrogen in carbon-based cathode catalysts.

(1) The graphitic N enhanced the O_2 adsorption and would cause the formation of the active sites derived from the C=O components. (Chapter 3)

(2) The doped nitrogen with the well-defined flat graphene lattice was contributed to improve the ORR activity. (Chapter 4)

(3) The Lewis basicity sites would be induced by the presence of the pyridinic N and valley N of the graphite surface. (Chapter 5)

These results show the O_2 and CO_2 adsorption sites are formed by not the nitrogen atoms but the carbon atoms next to or in the vicinity of the nitrogen atoms and suggests that the electronic structure modification of carbon atoms through hetero atom doping contributes to enhance the oxygen reduction activity.

6.2 Future prospects

In the future, it is required to reveal the structure of the adsorbed CO_2 on the nitrogen-doped graphite and estimate the Lewis basicity of CO_2 adsorption sites supported by the first principles calculation since the degree of the Lewis basicity is important for determining the interaction strength of CO_2 and the reaction rate of ORR. It is also useful to experimentally visualize the local atomic structure of the adsorbed CO_2 using STM or AFM for revealing the Lewis base sites. For example, some recent reports mentioned that the adsorbed CO_2 on Ni(110) [126] or Ru(0001) [136] is partially tilted to the substrate surface, which is similar configuration on N-HOPG in this study.

The valley N sites were believed to be one of the important nitrogen components for the formation of ORR active sites in the last decade [83]. I have observed the valley N using spectroscopic method in combination with first principles calculation, however, any group does not observe an atomic structure of the valley N experimentally. Therefore it is also required to visualize the local atomic and electronic structures of the valley N using STM and STS, respectively, since the detailed electronic structure of the valley N is crucial to control the property of the nitrogen-doped graphite.

The activity of these carbon-based materials indicates the potential to fine-tune the activity to use the degree of Lewis basicity of the graphite substrate as a standard. The Lewis basicity would be fine-tuned by controlling the prevalence of nitrogen species focused to the appropriate interaction strength for ORR. The properties of fine-tuned

Lewis basicity in carbon-based materials can be applied to the variety field of catalysis, including the use of the materials as CO_2 reduction reaction or hydrogen evolution reaction sites. Furthermore, the electronic structure modification of carbon atoms controlled by other chemical or mechanical method would also contribute to enhance the catalytic activity, suggesting the new development of the catalyst other than conventional method such as nitrogen doping.

Bibliography

[1] H. A. Gasteiger, S. S. Kocha, B. Sompalli, and F. T. Wagner, Appl. Catal. B Environ. **56**, 9 (2005).

[2] Y. Tanabe and E. Yasuda, Carbon **38**, 329 (2000).

[3] Z. Chen, J.-P. Dodelet, and J. Zhang, *Non-Noble Metal Fuel Cell Catalysts* (Wiley-VCH Verlag GmbH & Co. KGaA, Weinheim, Germany, 2014).

[4] H. J. H. Fenton, J. Chem. Soc. Trans. **65**, 899 (1894).

[5] V. R. Stamenkovic, B. S. Mun, M. Arenz, K. J. J. Mayrhofer, C. A. Lucas, G. Wang, P. N. Ross, and N. M. Markovic, Nat. Mater. **6**, 241 (2007).

[6] J. Greeley, I. E. L. Stephens, A. S. Bondarenko, T. P. Johansson, H. A. Hansen, T. F. Jaramillo, J. Rossmeisl, I. Chorkendorff, and J. K. Nørskov, Nat. Chem. **1**, 552 (2009).

[7] X. Huang, Z. Zhao, L. Cao, Y. Chen, E. Zhu, Z. Lin, M. Li, A. Yan, A. Zettl, Y. M. Wang, X. Duan, T. Mueller, and Y. Huang, Science **348**, 1230 (2015).

[8] C. Chen, Y. Kang, Z. Huo, Z. Zhu, W. Huang, H. L. Xin, J. D. Snyder, D. Li, J. a Herron, M. Mavrikakis, M. Chi, K. L. More, Y. Li, N. M. Markovic, G. A. Somorjai, P. Yang, and V. R. Stamenkovic, Science **343**, 1339 (2014).

[9] L. Zhang, L. T. Roling, X. Wang, M. Vara, M. Chi, J. Liu, S.-I. Choi, J. Park, J. A. Herron, Z. Xie, M. Mavrikakis, and Y. Xia, Science **349**, 412 (2015).

[10] K. Kamiya, R. Kamai, K. Hashimoto, and S. Nakanishi, Nat. Commun. **5**, 1 (2014).

[11] T. Yoshida and K. Kojima, Interface Mag. **24**, 45 (2015).

[12] R. Jasinski, Nature **201**, 1212 (1964).

[13] H. Jahnke, M. Schönborn, and G. Zimmermann, Top. Curr. Chem. **61**, 133 (1976).

[14] S. Gupta, D. Tryk, I. Bae, W. Aldred, and E. Yeager, J. Appl. Electrochem. **19**, 19 (1989).

[15] C. Médard, M. Lefèvre, J. P. Dodelet, F. Jaouen, and G. Lindbergh, Electrochim. Acta **51**, 3202 (2006).

[16] R. Bashyam and P. Zelenay, Nature **443**, 63 (2006).

[17] F. Jaouen and J. P. Dodelet, Electrochim. Acta **52**, 5975 (2007).

[18] F. Charreteur, S. Ruggeri, F. Jaouen, and J. P. Dodelet, Electrochim. Acta **53**, 6881 (2008).

[19] V. Nallathambi, J.-W. Lee, S. P. Kumaraguru, G. Wu, and B. N. Popov, J. Power Sources **183**, 34 (2008).

[20] M. Lefèvre, E. Proietti, F. Jaouen, and J.-P. Dodelet, Science **324**, 71 (2009).

[21] H. T. Chung, C. M. Johnston, K. Artyushkova, M. Ferrandon, D. J. Myers, and P. Zelenay, Electrochem. Commun. **12**, 1792 (2010).

[22] J. Y. Choi, R. S. Hsu, and Z. Chen, J. Phys. Chem. C **114**, 8048 (2010).

[23] G. Wu, K. L. More, C. M. Johnston, and P. Zelenay, Science **332**, 443 (2011).

[24] E. Proietti, F. Jaouen, M. Lefèvre, N. Larouche, J. Tian, J. Herranz, and J.-P. Dodelet, Nat. Commun. **2**, 416 (2011).

[25] S. Yuan, J. L. Shui, L. Grabstanowicz, C. Chen, S. Commet, B. Reprogle, T. Xu, L. Yu, and D. J. Liu, Angew. Chemie Int. Ed. **52**, 8349 (2013).

[26] J. Tian, A. Morozan, M. T. Sougrati, M. Lefèvre, R. Chenitz, J.-P. Dodelet, D. Jones, and F. Jaouen, Angew. Chemie Int. Ed. **52**, 6867 (2013).

[27] W. Ding, Z. Wei, S. Chen, X. Qi, T. Yang, J. Hu, D. Wang, L. J. Wan, S. F. Alvi, and L. Li, Angew. Chemie Int. Ed. **52**, 11755 (2013).

[28] D. Zhao, J. L. Shui, L. R. Grabstanowicz, C. Chen, S. M. Commet, T. Xu, J. Lu, and D. J. Liu, Adv. Mater. **26**, 1093 (2014).

[29] Y. Nabae, M. Sonoda, C. Yamauchi, Y. Hosaka, A. Isoda, and T. Aoki, Catal. Sci. Technol. **4**, 1400 (2014).

[30] Y. Nabae, Y. Kuang, M. Chokai, T. Ichihara, A. Isoda, T. Hayakawa, and T. Aoki, J. Mater. Chem. A **2**, 11561 (2014).

[31] Q. Wang, Z. Zhou, Y. Lai, Y. You, J. Liu, X. Wu, E. Terefe, C. Chen, L. Song, M. Rauf, N. Tian, and S. Sun, J. Am. Chem. Soc. **136**, 10882 (2014).

[32] L. Yang, N. Larouche, R. Chenitz, G. Zhang, M. Lefèvre, and J.-P. Dodelet, Electrochim. Acta **159**, 184 (2015).

[33] Y.-C. Wang, Y.-J. Lai, L. Song, Z.-Y. Zhou, J.-G. Liu, Q. Wang, X.-D. Yang, C. Chen, W. Shi, Y.-P. Zheng, M. Rauf, and S.-G. Sun, Angew. Chemie Int. Ed. **54**, 9907 (2015).

[34] O.-H. Kim, Y.-H. Cho, D. Y. Chung, M. J. Kim, J. M. Yoo, J. E. Park, H. Choe, and Y.-E. Sung, Sci. Rep. **5**, 8376 (2015).

[35] A. Zitolo, V. Goellner, V. Armel, M.-T. Sougrati, T. Mineva, L. Stievano, E. Fonda, and F. Jaouen, Nat. Mater. **14**, 937 (2015).

[36] M. Saito, Master Thesis (2011).

[37] T. Iwazaki, R. Obinata, W. Sugimoto, and Y. Takasu, Electrochem. Commun. **11**, 376 (2009).

[38] M. Chokai, M. Taniguchi, S. Moriya, K. Matsubayashi, T. Shinoda, Y. Nabae, S. Kuroki, T. Hayakawa, M. Kakimoto, J. Ozaki, and S. Miyata, J. Power Sources **195**, 5947 (2010).

[39] X. Wang, J. S. Lee, Q. Zhu, J. Liu, Y. Wang, and S. Dai, Chem. Mater. **22**, 2178 (2010).

[40] G. Liu, X. Li, P. Ganesan, and B. N. Popov, Electrochim. Acta **55**, 2853 (2010).

[41] R. A. Sidik, A. B. Anderson, N. P. Subramanian, S. P. Kumaraguru, and B. N. Popov, J. Phys. Chem. B **110**, 1787 (2006).

[42] T. Ikeda, M. Boero, S. F. Huang, K. Terakura, M. Oshima, and J. I. Ozaki, J. Phys. Chem. C **112**, 14706 (2008).

[43] X. Bao, X. Nie, D. von Deak, E. J. Biddinger, W. Luo, A. Asthagiri, U. S. Ozkan, and C. M. Hadad, Top. Catal. **56**, 1623 (2013).

[44] H. Kim, K. Lee, S. I. Woo, and Y. Jung, Phys. Chem. Chem. Phys. **13**, 17505 (2011).

[45] Y. Hiraike, M. Saito, H. Niwa, M. Kobayashi, Y. Harada, M. Oshima, J. Kim, Y. Nabae, and M. Kakimoto, Nanoscale Res. Lett. **10**, 179 (2015).

[46] A. Muthukrishnan, Y. Nabae, T. Okajima, and T. Ohsaka, ACS Catal. **5**, 5194 (2015).

[47] P. D. Nolan, B. R. Lutz, P. L. Tanaka, J. E. Davis, and C. B. Mullins, J. Chem. Phys. **111**, 3696 (1999).

[48] S. Chen, J. Bi, Y. Zhao, L. Yang, C. Zhang, Y. Ma, Q. Wu, X. Wang, and Z. Hu, Adv. Mater. **24**, 5593 (2012).

[49] T. Kondo, S. Casolo, T. Suzuki, T. Shikano, M. Sakurai, Y. Harada, M. Saito, M. Oshima, M. I. Trioni, G. F. Tantardini, and J. Nakamura, Phys. Rev. B **86**, 035436 (2012).

[50] X. Wang, X. Li, L. Zhang, Y. Yoon, P. K. Weber, H. Wang, J. Guo, and H. Dai, Science **324**, 768 (2009).

[51] T. Schiros, D. Nordlund, L. Pálová, D. Prezzi, L. Zhao, K. S. Kim, U. Wurstbauer, C. Gutiérrez, D. Delongchamp, C. Jaye, D. Fischer, H. Ogasawara, L. G. M. Pettersson, D. R. Reichman, P. Kim, M. S. Hybertsen, and A. N. Pasupathy, Nano Lett. **12**, 4025 (2012).

[52] G. Imamura and K. Saiki, J. Phys. Chem. C **115**, 10000 (2011).

[53] A. Auroux and A. Gervasini, J. Phys. Chem. **94**, 6371 (1990).

[54] J. C. Lavalley, Catal. Today **27**, 377 (1996).

[55] U. A. Paulus, T. J. Schmidt, H. A. Gasteiger, and R. J. Behm, J. Electroanal. Chem. **495**, 134 (2001).

[56] M. Kobayashi, Doctor Thesis (2007).

[57] J. Stöhr, *NEXAFS Spectroscopy* (Springer, 1992).

[58] A. Jorio, R. Saito, G. Dresselhaus, and M. S. Dresselhaus, *Raman Spectroscopy in Graphene Related Systems* (Wiley-VCH Verlag GmbH & Co. KGaA, Weinheim, Germany, 2011).

[59] F. Tuinstra and J. L. Koenig, J. Chem. Phys. **53**, 1126 (1970).

[60] H. Niwa, K. Horiba, Y. Harada, M. Oshima, T. Ikeda, K. Terakura, J. Ozaki, and S. Miyata, J. Power Sources **187**, 93 (2009).

[61] C. W. B. Bezerra, L. Zhang, K. Lee, H. Liu, J. Zhang, Z. Shi, A. L. B. Marques, E. P. Marques, S. Wu, and J. Zhang, Electrochim. Acta **53**, 7703 (2008).

[62] S. Maldonado, S. Morin, and K. J. Stevenson, Carbon **44**, 1429 (2006).

[63] P. Wang, Z. Wang, L. Jia, and Z. Xiao, Phys. Chem. Chem. Phys. **11**, 2730 (2009).

[64] N. Kobayashi, T. Enoki, C. Ishii, K. Kaneko, and M. Endo, J. Chem. Phys. **109**, 1983 (1998).

[65] E. Pollak, G. Salitra, A. Soffer, and D. Aurbach, Carbon **44**, 3302 (2006).

[66] D. Briggs and G. Beamson, Anal. Chem. **65**, 1517 (1993).

[67] Z. Yue, W. Jiang, L. Wang, S. Gardner, and C. Pittman, Carbon **37**, 1785 (1999).

[68] J. Pels, F. Kapteijn, J. Moulijn, Q. Zhu, and K. Thomas, Carbon **33**, 1641 (1995).

[69] J. Casanovas, J. M. Ricart, J. Rubio, F. Illas, and J. M. Jiménez-Mateos, J. Am. Chem. Soc. **118**, 8071 (1996).

[70] R. Jansen and H. Van Bekkum, Carbon **33**, 1021 (1995).

[71] J. Ripalda, N. Diaz, E. Roman, L. Galan, I. Montero, A. Goldoni, A. Baraldi, S. Lizzit, G. Comelli, and G. Paolucci, Phys. Rev. Lett. **85**, 2132 (2000).

[72] S. E. Rodil and S. Muhl, Diam. Relat. Mater. **13**, 1521 (2004).

[73] J. J. S. Acuña, C. A. Figueroa, M. E. H. Maia da Costa, P. Paredez, C. T. M. Ribeiro, and F. Alvarez, J. Non. Cryst. Solids **352**, 1314 (2006).

[74] J. J. S. Acuña, C. A. Figueroa, D. Biggemann, M. U. Kleinke, and F. Alvarez, J. Appl. Phys. **103**, 124907 (2008).

[75] Y. Nabae, I. Yamanaka, and K. Otsuka, Appl. Catal. A Gen. **280**, 149 (2005).

[76] J. M. Campos-Martin, G. Blanco-Brieva, and J. L. G. Fierro, Angew. Chemie Int. Ed. **45**, 6962 (2006).

[77] D. Geng, S. Yang, Y. Zhang, J. Yang, J. Liu, R. Li, T.-K. Sham, X. Sun, S. Ye, and S. Knights, Appl. Surf. Sci. **257**, 9193 (2011).

[78] M. T. Lusk, D. T. Wu, and L. D. Carr, Phys. Rev. B **81**, 155444 (2010).

[79] D. A. Horner, P. C. Redfern, M. Sternberg, P. Zapol, and L. A. Curtiss, Chem. Phys. Lett. **450**, 71 (2007).

[80] N. Ghaderi and M. Peressi, J. Phys. Chem. C **114**, 21625 (2010).

[81] T. Kondo, Y. Honma, J. Oh, T. Machida, and J. Nakamura, Phys. Rev. B **82**, 153414 (2010).

[82] B. Sanyal, O. Eriksson, U. Jansson, and H. Grennberg, Phys. Rev. B **79**, 113409 (2009).

[83] S.-F. Huang, K. Terakura, T. Ozaki, T. Ikeda, M. Boero, M. Oshima, J. Ozaki, and S. Miyata, Phys. Rev. B **80**, 235410 (2009).

[84] T. Ikeda and K. Terakura, *private communicatoin*.

[85] L. Qu, Y. Liu, J.-B. Baek, and L. Dai, ACS Nano **4**, 1321 (2010).

[86] P. Matter, L. Zhang, and U. Ozkan, J. Catal. **239**, 83 (2006).

[87] H. T. Chung, J. H. Won, and P. Zelenay, Nat. Commun. **4**, 1922 (2013).

[88] K. Gong, F. Du, Z. Xia, M. Durstock, and L. Dai, Science **323**, 760 (2009).

[89] C. H. Choi, H.-K. Lim, M. W. Chung, J. C. Park, H. Shin, H. Kim, and S. I. Woo, J. Am. Chem. Soc. **136**, 9070 (2014).

[90] H. Niwa, M. Kobayashi, K. Horiba, Y. Harada, M. Oshima, K. Terakura, T. Ikeda, Y. Koshigoe, J. I. Ozaki, S. Miyata, S. Ueda, Y. Yamashita, H. Yoshikawa, and K. Kobayashi, J. Power Sources **196**, 1006 (2011).

[91] W. Ouyang, D. Zeng, X. Yu, F. Xie, W. Zhang, J. Chen, J. Yan, F. Xie, L. Wang, H. Meng, and D. Yuan, Int. J. Hydrogen Energy **39**, 15996 (2014).

[92] M. Favaro, L. Perini, S. Agnoli, C. Durante, G. Granozzi, and A. Gennaro, Electrochim. Acta **88**, 477 (2013).

[93] J. F. Ziegler, M. D. Ziegler, and J. P. Biersack, Nucl. Instruments Methods Phys. Res. Sect. B **268**, 1818 (2010).

[94] M. Risch and M. Bradley, Phys. Status Solidi C **5**, 939 (2008).

[95] S. E. O'Donnell and P. Reinke, J. Vac. Sci. Technol. B **27**, 2209 (2009).

[96] Q. Yang, T. Li, B. King, and R. MacDonald, Phys. Rev. B **53**, 3032 (1996).

[97] T. Sharifi, G. Hu, X. Jia, and T. Wågberg, ACS Nano **6**, 8904 (2012).

[98] X. Wang, Z. Hou, T. Ikeda, S.-F. Huang, K. Terakura, M. Boero, M. Oshima, M. Kakimoto, and S. Miyata, Phys. Rev. B **84**, 245434 (2011).

[99] Y. Niimi, T. Matsui, H. Kambara, K. Tagami, M. Tsukada, and H. Fukuyama, Phys. Rev. B **73**, 085421 (2006).

[100] A. N. Patel, M. G. Collignon, M. A. O'Connell, W. O. Y. Hung, K. McKelvey, J. V. Macpherson, and P. R. Unwin, J. Am. Chem. Soc. **134**, 20117 (2012).

[101] F. Orlando, P. Lacovig, M. Dalmiglio, A. Baraldi, R. Larciprete, and S. Lizzit, Surf. Sci. **643**, 214 (2016).

[102] M. Batzill, Surf. Sci. Rep. **67**, 83 (2012).

[103] W. Zhao, O. Höfert, K. Gotterbarm, J. F. Zhu, C. Papp, and H.-P. Steinrück, J. Phys. Chem. C **116**, 5062 (2012).

[104] E. H. Martins Ferreira, M. V. O. Moutinho, F. Stavale, M. M. Lucchese, R. B. Capaz, C. A. Achete, and A. Jorio, Phys. Rev. B **82**, 125429 (2010).

[105] I. Shimoyama, G. Wu, T. Sekiguchi, and Y. Baba, Phys. Rev. B **62**, R6053 (2000).

[106] X. Wang, Z. Hou, T. Ikeda, M. Oshima, M. Kakimoto, and K. Terakura, J. Phys. Chem. A **117**, 579 (2013).

[107] F. Atamny, J. Blöcker, B. Henschke, R. Schlögl, T. Schedelniedrig, M. Keil, and A. M. Bradshaw, J. Phys. Chem. **96**, 4522 (1992).

[108] Z. Hou, X. Wang, T. Ikeda, K. Terakura, M. Oshima, and M. A. Kakimoto, Phys. Rev. B **87**, 165401 (2013).

[109] M. dos Santos and F. Alvarez, Phys. Rev. B **58**, 13918 (1998).

[110] A. Cuesta, P. Dhamelincourt, J. Laureyns, A. Martínez-Alonso, and J. M. D. Tascón, Carbon **32**, 1523 (1994).

[111] A. Jorio, M. M. Lucchese, F. Stavale, E. H. M. Ferreira, M. V. O. Moutinho, R. B. Capaz, and C. A. Achete, J. Physics. Condens. Matter **22**, 334204 (2010).

[112] A. Jorio, M. M. Lucchese, F. Stavale, and C. A. Achete, Phys. Status Solidi B **246**, 2689 (2009).

[113] X. Li, G. Liu, and B. N. Popov, J. Power Sources **195**, 6373 (2010).

[114] T. Ikeda, Z. Hou, G. L. Chai, and K. Terakura, J. Phys. Chem. C **118**, 17616 (2014).

[115] H. Niwa, M. Saito, M. Kobayashi, Y. Harada, M. Oshima, S. Moriya, K. Matsubayashi, Y. Nabae, S. Kuroki, T. Ikeda, K. Terakura, J. I. Ozaki, and S. Miyata, J. Power Sources **223**, 30 (2013).

[116] K. Kamiya, H. Koshikawa, H. Kiuchi, Y. Harada, M. Oshima, K. Hashimoto, and S. Nakanishi, ChemElectroChem **1**, 877 (2014).

[117] H. Kiuchi, H. Niwa, M. Kobayashi, Y. Harada, and M. Oshima, Electrochim. Acta **82**, 291 (2012).

[118] U. Tylus, Q. Jia, K. Strickland, N. Ramaswamy, A. Serov, P. Atanassov, and S. Mukerjee, J. Phys. Chem. C **118**, 8999 (2014).

[119] P. S. Miedema, M. M. van Schooneveld, R. Bogerd, T. C. R. Rocha, M. Hävecker, A. Knop-Gericke, and F. M. F. de Groot, J. Phys. Chem. C **115**, 25422 (2011).

[120] S. Moroboshi, S. Saji, Y. Shirota, T. Fujitani, T. Kondo, and J. Nakamura, in *96th CSJ Annu. Meet.* 2E6-46 (2014).

[121] M. Scardamaglia, M. Amati, B. Llorente, P. Mudimela, J.-F. Colomer, J. Ghijsen, C. Ewels, R. Snyders, L. Gregoratti, and C. Bittencourt, Carbon **77**, 319 (2014).

[122] H. Kiuchi, T. Kondo, M. Sakurai, D. Guo, J. Nakamura, H. Niwa, J. Miyawaki, M. Kawai, M. Oshima, and Y. Harada, Phys. Chem. Chem. Phys. **18**, 458 (2016).

[123] P. A. Redhead, Vacuum **12**, 203 (1962).

[124] J. L. Edridge, K. Freimann, D. J. Burke, and W. A. Brown, Philos. Trans. R. Soc. A Math. Phys. Eng. Sci. **371**, 20110578 (2013).

[125] G. Illing, D. Heskett, E. W. Plummer, H.-J. Freund, J. Somers, T. Lindner, A. M. Bradshaw, U. Buskotte, M. Neumann, U. Starke, K. Heinz, P. L. De Andres, D. Saldin, and J. B. Pendry, Surf. Sci. **206**, 1 (1988).

[126] X. Ding, L. De Rogatis, E. Vesselli, A. Baraldi, G. Comelli, R. Rosei, L. Savio, L. Vattuone, M. Rocca, P. Fornasiero, F. Ancilotto, A. Baldereschi, and M. Peressi, Phys. Rev. B **76**, 195425 (2007).

[127] H. Kuhlenbeck, C. Xu, B. Dillmann, M. Haßel, B. Adam, D. Ehrlich, S. Wohlrab, H.-J. Freund, U. A. Ditzinger, H. Neddermeyer, M. Neuber, and M. Neumann, Berichte Der Bunsengesellschaft Für Phys. Chemie **96**, 15 (1992).

[128] O. Seiferth, K. Wolter, B. Dillmann, G. Klivenyi, H.-J. Freund, D. Scarano, and A. Zecchina, Surf. Sci. **421**, 176 (1999).

[129] J. Kiss, K. Révész, and F. Solymosi, Surf. Sci. **207**, 36 (1988).

[130] L. Bugyi, A. Oszkó, and F. Solymosi, Surf. Sci. **461**, 177 (2000).

[131] K. Takeuchi, S. Yamamoto, Y. Hamamoto, Y. Shiozawa, K. Tashima, H. Fukidome, T. Koitaya, K. Mukai, S. Yoshimoto, M. Suemitsu, Y. Morikawa, J. Yoshinobu, and I. Matsuda, submitted.

[132] H.-J. Freund and M. W. Roberts, Surf. Sci. Rep. **25**, 225 (1996).

[133] D. Maganas, P. Kristiansen, L.-C. Duda, A. Knop-Gericke, S. DeBeer, R. Schlögl, and F. Neese, J. Phys. Chem. C **118**, 20163 (2014).

[134] F. Tao, M. H. Qiao, Z. H. Wang, and G. Q. Xu, J. Phys. Chem. B **107**, 6384 (2003).

[135] D. Guo, R. Shibuya, C. Akiba, S. Saji, T. Kondo, and J. Nakamura, Science **351**, 361 (2016).

[136] X. Feng, J. I. Cerdá, and M. Salmeron, J. Phys. Chem. Lett. 1780 (2015).

List of Publications and Presentation

List of papers

1. **Hisao Kiuchi**, Hideharu Niwa, Masaki Kobayashi, Yoshihisa Harada, Masaharu Oshima, Masayuki Chokai, Yuta Nabae, Shigeki Kuroki, Masa-aki Kakimoto, Takashi Ikeda, Kiyoyuki Terakura and Seizo Miyata, "Study on the oxygen adsorption property of nitrogen-containing metal-free carbon-based cathode catalysts for oxygen reduction reaction", Electrochimica Acta, **82**, pp291-294 (2012).

2. **Hisao Kiuchi**, Takahiro Kondo, Masataka Sakurai, Donghui Guo, Junji Nakamura, Hideharu Niwa, Jun Miyawaki, Maki Kawai, Masaharu Oshima, and Yoshihisa Harada, "Characterization of nitrogen species incorporated into graphite using low energy nitrogen ion sputtering", Physical Chemistry Chemical Physics, 18, pp458-465 (2016).

3. **Hisao Kiuchi**, Riku Shibuya, Takahiro Kondo, Junji Nakamura, Hideharu Niwa, Jun Miyawaki, Maki Kawai, Masaharu Oshima, and Yoshihisa Harada, "Lewis basicity of nitrogen-doped graphite observed by CO_2 chemisorption", Nanoscale Research Letters *accepted*.

Papers not included in this thesis

4. Hideharu Niwa, **Hisao Kiuchi**, Jun Miyawaki, Yoshihisa Harada, Masaharu Oshima, Yuta Nabae, Tsutomu Aoki, "*Operando* soft X-Ray emission spectroscopy of iron phthalocyanine-based oxygen reduction catalysts", Electrochemistry Communications, **35**, pp57–60 (2013).

5. Kamiya Kazuhide, Hiroyuki Koshikawa, **Hisao Kiuchi**, Yoshihisa Harada, Masaharu Oshima, Kazuhito Hashimoto, and Shuji Nakanishi, "Iron-nitrogen coordination in modified graphene catalyzes a four-electron-transfer oxygen reduction reaction", ChemElectroChem, **1**, pp877-884 (2014).

6. Daisuke Asakura, Eiji Hosono, Hideharu Niwa, **Hisao Kiuchi**, Jun Miyawaki, Yusuke Nanba, Masashi Okubo, Hirofumi Matsuda, Haoshen Zhou, Masaharu Oshima, and Yoshihisa Harada, "*Operando* soft x-ray emission spectroscopy of $LiMn_2O_4$ thin film involving Li–ion extraction/insertion reaction", Electrochemistry Communications, **50**, pp93–96 (2015).

7. Keisuke Kurita, Daiichiro Sekiba, Isao Harayama, Kenta Chito, Yoshihisa Harada, **Hisao Kiuchi**, Masaharu Oshima, Shigeyuki Takagi, Motoaki Matsuo, Ryutaro Sato, Katsutoshi Aoki, and Shin-ichi Orimo, "Multi-phonon excitations in Fe 2*p* RIXS on Mg_2FeH_6", Journal of the Physical Society of Japan, **84**, 043201 (2015).

8. Yusuke Nanba, Tatsumi Iwao, Benoit Mortemard de Boisse, Wenwen Zhao, Eiji Hosono, Daisuke Asakura, Hideharu Niwa, **Hisao Kiuchi**, Jun Miyawaki, Yoshihisa Harada, Masashi Okubo, and Atsuo Yamada, " Redox Potential Paradox in Na_xMO_2 for Sodium-Ion Battery Cathodes", Chemistry of Materials, in press.

Domestic papers

1. 原田慈久，徳島高，堀川裕加，丹羽秀治，**木内久雄**，小林正起，尾嶋正治，辛埴，液体水分子の内殻励起ダイナミクスと局所構造，しょうとつ 10 (1), pp14-20 (2013).

International conferences

(Oral presentation)

1. ○**Hisao Kiuchi**, Makoto Saito, Masaki Kobayashi, Yoshihisa Harada, Masaharu Oshima, Masayuki Chokai, Yuta Nabae, Shigeki Kuroki, Takashi Ikeda, Kiyoyuki

Terakura, and Seizo Miyta, "Characteristics of Oxygen Adsorption on Carbon-based Catalysts Revealed by *in situ* X-ray Photoemission Spectroscopy", 62nd Annual Meeting of the International Society of Electrochemistry, ise111457, Niigata, Japan (September 2011).

(Poster presentation)

2. ○**Hisao Kiuchi**, Hideharu Niwa, Masaki Kobayashi, Yoshihisa Harada, Masaharu Oshima, Masayuki Chokai, Yuta Nabae, Shigeki Kuroki, Takashi Ikeda, Kiyoyuki Terakura, and Seizo Miyta, "Characteristics of Oxygen Adsorption on Carbon-based Catalysts Revealed by *in situ* X-ray Photoelectron Spectroscopy", The 2nd International Fuel Cell Summer Seminar for Young Scientists, Yamanashi, Japan (August 2011).

3. ○**Hisao Kiuchi**, Takahiro Kondo, Masataka Sakurai, Hideharu Niwa, Masaki Kobayashi, Yoshihisa Harada, Takashi Ikeda, Kiyoyuki Terakura, Junji Nakamura and Masaharu Oshima, "Characteristics of Oxygen adsorption on Nitrogen doped HOPG revealed by X-ray absorption spectroscopy", Pacific Rim Meeting on Electrochemical and Solid-State Science 2012 (PRiME 2012), Abstract #1439, Hawaii, USA (October 2012).

4. ○**Hisao Kiuchi**, Takahiro Kondo, Masataka Sakurai, Junji Nakamura, Hideharu Niwa, Jun Miyawaki, Yoshihisa Harada and Masaharu Oshima, "X-ray absorption study on the electronic structure of nitrogen doped graphite", 5th International Conference on Recent Progress in Graphene Research (RPGR 2013), 12p-P4-33, Tokyo, Japan (September 2013).

5. ○**Hisao Kiuchi**, Takahiro Kondo, Masataka Sakurai, Hideharu Niwa, Jun Miyawaki, Yoshihisa Harada, Takashi Ikeda, Zhufeng Hou, Kiyoyuki Terakura, Junji Nakamura and Masaharu Oshima, "Oxygen Adsorption Characteristics of Nitrogen-doped Graphite Revealed by N 1*s* X-ray Absorption Spectroscopy", 224th ECS Meeting, Abstract #1493, San Francisco, California, USA (October 2013).

6. ○**Hisao Kiuchi**, Riku Shibuya, Takahiro Kondo, Donghui Guo, Junji Nakamura, Hideharu Niwa, Jun Miyawaki, Maki Kawai, Masaharu Oshima, and Yoshihisa Harada, "X-ray absorption study of nitrogen doped graphite upon CO_2 adsorption", The 7th International Symposium on Surface Science (ISSS-7), 4PN-70, Shimane,

Japan (November 2014).

Domestic conferences

(Oral presentation)

1. ○木内久雄, 小林正起, 原田慈久, 尾嶋正治, 畳開真之, 難波江裕太, 黒木重樹, 池田隆司, 寺倉清之, 宮田清藏, 金属を含まないカーボンアロイ型燃料電池正極触媒の酸素吸着特性 : 光電子分光を用いた電子状態分析, 第 52 回電池討論会, 2F04, 東京 2011 年 10 月.

2. ○木内久雄, 櫻井雅崇, 丹羽秀治, 宮脇淳, 原田慈久, 尾嶋正治, 近藤剛弘, 中村潤児, 池田隆司, 寺倉清之, 窒素ドープグラファイトモデル触媒の酸素吸着特性 : 放射光を用いた電子状態分析, 電気化学会第 80 回大会, 2C03, 宮城, 2013 年 3 月.

3. ○木内久雄, 近藤剛弘, 櫻井雅崇, 中村潤児, 丹羽秀治, 宮脇淳, 原田慈久, 尾嶋正治, X 線吸収分光による窒素ドープグラファイトの窒素の電子状態観測, 第 7 回分子科学討論会, 4B03, 京都, 2013 年 9 月.

4. ○木内久雄, 渋谷陸, 近藤剛弘, Donghui Guo, 中村潤児, 丹羽秀治, 宮脇淳, 原田慈久, 川合眞紀, 尾嶋正治, X 線吸収分光法による窒素ドープグラファイトへの CO_2 吸着状態の観測, 第 28 回日本放射光学会年会・放射光科学合同シンポジウム(JSR15), 1C003, 滋賀, 2015 年 1 月.

5. ○木内久雄, 渋谷陸, 近藤剛弘, 中村潤児, 丹羽秀治, 宮脇淳, 原田慈久, 川合眞紀, 尾嶋正治, X 線分光による窒素ドープグラファイトに化学吸着した CO_2 の観測, 第 25 回日本 MRS 年次大会, B1-O9-012, 神奈川, 2015 年 12 月.

6. ○木内久雄, 渋谷陸, 近藤剛弘, 中村潤児, 丹羽秀治, 宮脇淳, 原田慈久, 川合眞紀, 尾嶋正治, X 線光電子・吸収分光法による窒素ドープグラファイトに配向吸着した CO_2 の観測, 第 29 回日本放射光学会年会・放射光科学合同シンポジウム(JSR16), 5B006, 千葉, 2016 年 1 月.

(Poster presentation)

7. ○木内久雄, 近藤剛弘, 小林正起, 原田慈久, 尾嶋正治, 中村潤児, 畳開真之, 難波江祐太, 黒木重樹, 池田隆司, 寺倉清之, 宮田清藏, カーボンアロイ触媒及び窒素ドープグラファイトの酸素吸着に伴う電子状態変化の解析, 第 25

回日本放射光学会年会・放射光科学合同シンポジウム(JSR12), 8P100, 佐賀, 2012 年 1 月.

8. ○木内久雄, 近藤剛弘, 櫻井雅崇, 中村潤児, 丹羽秀治, 宮脇淳, 原田慈久, 尾嶋正治, グラファイトのエッジ面及びベーサル面にドープされた窒素種の電子状態観察, 第 27 回日本放射光学会年会・放射光科学合同シンポジウム (JSR14), 13P078S, 広島, 2014 年 1 月.

9. ○木内久雄, 近藤剛弘, 櫻井雅崇, 中村潤児, 丹羽秀治, 宮脇淳, 原田慈久, 川合眞紀, 尾嶋正治, グラファイトのエッジ面及びベーサル面にドープされた窒素種の電子状態観察, 東京大学放射光アウトステーション報告会 SPring-8 BL07LSU の現状と第Ⅱ期への展望, 千葉, 2014 年 2 月.

10. ○木内久雄, 櫻井雅崇, 近藤剛弘, 中村潤児, 丹羽秀治, 宮脇淳, 原田慈久, 川合眞紀, 尾嶋正治, グラファイトのエッジ及び面内に取り込まれた窒素構造の電子状態分析, 電気化学会第 81 回大会, PFC16, 大阪, 2014 年 3 月.

11. ○木内久雄, 渋谷陸, 近藤剛弘, Donghui Guo, 中村潤児, 丹羽秀治, 宮脇淳, 原田慈久, 川合眞紀, 尾嶋正治, X 線吸収分光法による窒素ドープグラファイトへのCO_2吸着の観測, 放射光学会第7回若手研究会 最先端オペランド分光で明らかになる物性科学, P9, 千葉, 2014 年 9 月.

12. ○木内久雄, 渋谷陸, 近藤剛弘, Donghui Guo, 中村潤児, 丹羽秀治, 宮脇淳, 原田慈久, 川合眞紀, 尾嶋正治, 窒素ドープグラファイトの CO_2 吸着特性と ORR 活性サイトの考察, 電気化学会第 82 回大会, PFC21, 神奈川, 2015 年 3 月.

13. ○木内久雄, 渋谷陸, 近藤剛弘, Donghui Guo, 中村潤児, 丹羽秀治, 宮脇淳, 原田慈久, 川合眞紀, 尾嶋正治, X 線光電子・吸収分光による窒素ドープグラファイトに化学吸着した CO_2 の観測, 物性研短期研究会「反応と輸送」, P-33, 千葉, 2015 年 6 月.

Awards

1. The 2nd International Fuel Cell Summer Seminar for Young Scientists Poster Award, "Characteristics of Oxygen Adsorption on Carbon-based Catalysts Revealed by *in situ* X-ray Photoelectron Spectroscopy", August 2011.

2. 電気化学会第 81 回大会優秀ポスター賞, “グラファイトのエッジ及び面内に取り込まれた窒素構造の電子状態分析”, (PFC16) 2014 年 3 月.

3. 第 25 回日本 MRS 年次大会奨励賞, “X 線分光による窒素ドープグラファイトに化学吸着した CO_2 の観測”, (B1-O9-012) 2015 年 12 月.

Acknowledgments

I would like to express my gratitude to the following people for their support and help about my doctoral thesis. First of all, I would like to express my great gratitude to my supervisor Prof. Maki Kawai for providing me this great opportunity to study as Ph. D. candidate in her laboratory, insightful comments and considerable encouragements.

I especially would like to express my profound gratitude to Prof. Yoshihisa Harada for teaching me fundamental experimental techniques, his passionate ambition, and in-depth discussion. I also would like to express my special gratitude to Prof. Masaharu Oshima for teaching me principles of science, discussion, and presentation.

I am deeply grateful to the member of “NEDO/XES-group”. I would like to thank Dr. J. Miyawaki, Dr. M. Kobayashi, Dr. C. Sakai, Dr. S. Hidai, Dr. H. Niwa, Dr. Y. Cui, Mr. M. Saito, Mr. Y. Hiraike, Mr. J. Nakajima, Mr. K. Yamazoe, Mr. N. Itamoto, and Mr. T. Inoue for giving me opportunities to study variable scientific topics and conduct meaningful discussion.

I wish to express my appreciation to the member of Kawai laboratory, Prof. N. Takagi, Prof. H. Ueba, Prof. Y. Kim, Dr. N. Tsukahara, Dr. R. Arafune, Dr. E. Minamitani, Dr. C.-L. Lin, Dr. H.J. Yang, Dr. N. Ohta, Dr. R. Hiraoka, Ms. I. Miyabi, Mr. K. Kawahara, Mr. T. Nakazawa, Mr. K. Yukizaki, Mr. K. Nakamura, Mr. S. Inakazu, Mr. M. Kanno, Mr. R. Nagao, Mr. K. Morita, Mr. N. Kawakami, Mr. S. Kawahara, Mr. K. Shindo, Mr. H. Okumura, Mr. Y. Ohda, Mr. K. Kimura, Mr. M. Shinozuka, Mr. R. Shimomura and Mr. M. Yoshimura for their extensive discussion. I would like to thank Ms. Y. Izumi for huge help of business and paperwork.

I gratefully acknowledge the member of Oshima laboratory and Fujioka laboratory, in particular, Prof. H. Kumigashira, Prof. K. Horiba, Dr. I. Ohkubo, Dr. S. Toyoda, Prof. H. Fujioka, Dr. J. Ohta and Dr. A. Kobayashi for valuable discussion. I also would like to thank Ms. H. Imafuku, Ms. H. Tanomuro, Ms. M. Harada and Ms. Y. Yamamoto for huge help of business and paperwork.

I am very grateful to the member of BL07LSU in SPring-8, Prof. I. Matsuda, Prof. H. Wadati, Dr. S. Yamamoto, Dr. K. Yaji, Dr. Y. Hirata, Dr. N. Nagamura, Dr. R. Hobara, Dr. M. Fujisawa, Dr. A. Harasawa, Dr. M. Ogawa, Dr. R. Yukawa, Dr. K. Takubo, Mr. T.

Kitagawa, Mr. S. Yamamoto, Mr. Y. Yamamoto, Mr. K. Fujikawa, Mr. Y. Yokoyama, Ms. R. Liu, Mr. K. Akikubo, Mr. T. Someya, Mr. T. Tsuyama, Mr. S. Ito, Ms. K. Takeuchi and Mr. K. Yamamoto for useful discussion and suggestions. I also would like to thank Ms. M. Araki, Ms. Y. Kosegawa, Ms. E. Mitsuda, Ms. Y. Aihara, Ms. Y. Kaneko and Ms. Y. Tsutsumi for their enormous help.

I would like to thank the member of "NEDO CAC group", in particular, Prof. S. Miyata, Prof. K. Terakura, Porf. M. Kakimoto, Prof. S. Kuroki, Porf. T. Ohsaka, Prof. K. Saiki, Dr. T. Ikeda, Dr. Y. Nabae, Dr. S. Obata and Dr. G. Imamura for sample preparation, theoretical calculation, and invaluable discussion about fuel cells. I am deeply grateful to Prof. J. Nakamura, Prof. T. Kondo, Mr. M. Sakurai, Dr. D. Guo, Mr. R. Shibuya, and Ms. C. Akiba for the model catalysts preparation and analyses in SPring-8.

I would like to thank Dr. T. Muro, Dr. Y. Tamenori, Dr. Y. Izumi at BL27SU in SPring-8, Dr. E. Ikenaga at BL47SU in SPring-8, Prof. J. Guo and Mr. X. Feng at BL 7.0.1.1 in ALS for their technical supports during the experiments.

I also would like to thank other collaborators, in particular, Dr. T. Asakura, Dr. E. Hosono, Prof. K. Fukuda, Prof. D. Sekiba, Dr. K. Kurita, Prof. S. Nakanishi, Dr. K. Kamiya, Dr. T. Masuda, Prof. A. Yamada, Prof. M. Okubo, Dr. Y. Yamada, Mr. G. Oyama and Dr. T. Tokushima for the joint researches in SPring-8.

This work was financially supported by the New Energy and Industrials Technology Development Organization (NEDO). I also acknowledge financial support for making my Ph. D. study from Japan Society for the Promotion of Science (JSPS) Research Fellowship for Young Scientists and JSPS through Program for Leading Graduate Schools (MERIT).

Finally, I would like to thank to my parents and family for their warm support and deep understanding.

December, 2015

Hisao Kiuchi